DEPENDENCE OF MECHANICAL PROPERTIES OF PARTIALLY ORIENTED POLYMERIC SYSTEMS ON CHEMICAL STRUCTURE AND MOLECULAR ARCHITECTURE

A Dissertation

Presented to

The Academic Faculty

by

Xin Dong

In Partial Fulfillment

of the Requirements for the Degree

Doctor of Philosophy in the

School of Materials Science and Engineering

Georgia Institute of Technology

August 2015

DEPENDENCE OF MECHANICAL PROPERTIES OF PARTIALLY ORIENTED POLYMERIC SYSTEMS ON CHEMICAL STRUCTURE AND MOLECULAR ARCHITECTURE

Approved by:

Dr. Karl I. Jacob, Advisor

School of Materials Science and Engineering

Georgia Institute of Technology

Dr. David L. McDowell, Co-advisor

School of Mechanical Engineering

Georgia Institute of Technology

Dr. Donggang Yao

School of Materials Science and Engineering

Georgia Institute of Technology

Dr. Arun Gokhale

School of Materials Science and Engineering

Georgia Institute of Technology

Dr. Anselm C. Griffin

School of Materials Science and Engineering

Georgia Institute of Technology

Date Approved: May 14,2015

ACKNOWLEDGEMENTS

First of all I would like to express my gratitude my advisor, Dr. Karl Jacob and my co-advisor, Dr. David McDowell for their support, encouragement and patience during my PhD study, without which I cannot even imagine the achievement and academic level I have reached so far.

I would like to thank my thesis committee, Dr. Anselm Griffin, Dr. Donggang Yao and Dr. Arun Gokhale, for their valuable suggestions for my proposal and careful reading of my dissertation. Particularly, Dr. Griffin provided substantial guidance in the experimental part of the dissertation. Dr. Yao shared insightful discussions in a variety of simulation and experimental data interpretation. Dr. Gokhale provided important instructions in the data-analysis tools, especially the two-point statistics method.

I would specially thank my former group mate, Dr. Zaixing Zhang, for his training and inspirations in chemical synthesis, sample preparation and polymer characterization. In collaboration with him, the experimental work proceeded much faster than expected owing to his abundant experience and serious working attitude in the experimental area.

I would also like to thank other faculty members and my colleagues in the materials science and engineering department for their kind help during my research. To name just a few of many, Dr. An-Ting Chien helped with X-ray diffraction experimental set-up and data analysis. Dr. Chaowei Feng helped with UV-Vis spectroscopy and GPC data interpretation. Dr. Surya Kalidindi, Dr. Tony Fast and Dr. Mohammed Abba kindly shared code for two-point statistics analysis of nanocrystalline metals. Dr. JC Gumbart and Hennim Hwang optimized force fields and constructed initial structures for MD

simulations of experimental structures. Kelsey Novak assisted in liquid crystalline elastomer shape memory experiments.

I would like to thank my industrial mentors, Dr. James Shepherd and Dr. Kelly Andersen for their directions in the initial stage of the simulation project.

I would like to thank financial support from the Center for computational Materials Design (CCMD), a joint National Science Foundation (NSF) Industry/University Cooperative Research Center at Penn State (IIP-1034965) and Georgia Tech (IIP-1034968).

Finally I would like to express my sincere thanks to my wife, Fangbing Lv and lovely newborn daughter, Taylor Yunhan Dong, for sharing with me the happiest moments so far in my life. Last but not least, I thank my parents, Cuntian Dong and Xiaoying Dong, who are both university professors, educated and enlightened me throughout my life.

TABLE OF CONTENTS

LIST OF TABLES

LIST OF FIGURES

LIST OF SYMBOLS AND ABBREVIATIONS

d	Distance
E	Energy
F	Force
L	Length
r	Radius
S	Hermans' orientation parameter
T_{Cr}	Crystallization temperature
T_g	Glass transition temperature
T_{NI}	Nematic-to-isotropic phase transformation temperature
$T_{Sc\text{-}Iso}$	Smectic-to-isotropic phase transformation temperature
$T_{Sc\text{-}N}$	Smectic-to-nematic phase transformation temperature
V	Volume
ε	Strain
σ	Stress
θ	Angle
φ	Azimuthal angle
λ	Wavelength
Ω	Periodic box size
2D	Two-dimensional
3D	Three-dimensional
AA	All-atom
AB	Azobenzene

CDF	Chord distribution function
DIC	diisopropylcarbodiimide
DMAP	dimethylaminopyridine
DSC	Differential scanning calorimetry
DTPS	Dimethylaminopyridinium-toluenesulfonate
fs	Femtosecond
GPC	Gel permeation chromatography
LC	Liquid crystal
LCE	Liquid crystalline elastomer
LCP	Liquid crystalline polymer
MC	Monte Carlo
MCE	Main-chain elastomer
MCLCE	Main-chain liquid crystalline elastomer
MD	Molecular Dynamics
Mn	Number average molecular weight
mol	molecule
Mw	Weight average molecular weight
ns	Nanosecond
$NL_z\sigma_x\sigma_yT$	Constant number, z dimension, lateral stresses and temperature
NPT	Constant number, pressure, and temperature
NVT	Constant number, volume, and temperature
NVT	Constant number, volume, and temperature
ps	Picosecond

PDI	Polydispersity index
PE	Polyethylene
PEVA	Poly(ethylene-co-vinylactate)
POM	Polarized optical microscopy
PP	Polypropylene
PPDL	Poly(ω-pentadecalactone)
Rg	Radius of gyration
RT	Room temperature
SAXS	Small-angle X-ray scattering
SCE	Side-chain elastomer
SCLCE	Side-chain liquid crystalline elastomer
UA	United atom
UV	Ultraviolet
Vis	Visible
WAXS	Wide-angle X-ray scattering
XRD	X-ray diffraction pattern
XL	Crosslinking

SUMMARY

Partially oriented polymeric structures such as semi-crystalline polymers and liquid crystalline polymers/elastomers cover a wide range of synthetic and natural the polymeric materials. Owing to the significant differences between the molecular structures and properties of ordered (crystalline or liquid crystalline) and amorphous regions, such as orientation ordering, tensile moduli and relaxation times, these materials show complex patterns of behavior, although the molecular level mechanisms for deformation are still not well-understood.

Due to time and length scale limitations of the existing characterization tools, experimental studies cannot capture the morphological evolution of the whole crystallization and deformation process. Molecular dynamics (MD) simulation based on a united atom method were performed, to study the crystallization behavior and molecular response of semi-crystalline polyethylene structures under external stresses in a time scale of nanoseconds (ns) to capture the molecular details. Using the data from MD simulations, the effect of lamellae orientation on the stress-strain behavior was evaluated to understand the morphological evolution during deformation. The annealing and recovery simulations of the as-deformed samples were also performed, to validate the stability of the observed morphologies during non-equilibrium deformation. For the data analysis, local density distribution, Hermans' orientation mapping and two-point statistics in structural quantification of the semi-crystalline structures at different stage of crystallization, deformation and recovery were applied.

Free-standing and supported thin films were studied to understand their morphological characteristics. Influence of free-surfaces in nanoscale samples compared to spatially continuous periodic boundary conditions were explored in detail. The stress-induced morphological changes of free-standing and supported thin films with strong interacting surfaces were also investigated.

Process-structure relationships are also investigated for liquid crystalline elastomers, with experimental approaches for validation. Structures and properties of a series of azobenzene containing liquid crystalline elastomeric films were characterized in detail by a combination of differential scanning calorimetry (DSC), polarized optical microscopy (POM), RSA solid dynamic mechanical analyzer and two-dimensional X-ray scattering. With large uniaxial stretch at elevated temperature, followed by annealing procedure, a highly-oriented monodomain smectic-C liquid crystalline phase was obtained and confirmed by the X-ray diffraction pattern. The prepared monodomain films showed strong opto-mechanical responses upon exposure to ultraviolet (UV) light at 365 nm, as a result of an optically induced isomerization of azobenzene moieties in the backbone. Compared to the previously reported side-chain and copolymer LCEs, the new end-on main-chain LCEs presented more pronounced mechanical responses due to the large backbone molecular motion during the *trans-cis* transition of the azobenzene moieties upon UV irradiation. The UV-induced stress response property was applied in the design of a fully reversible actuator by a single monochromic light source at room temperature in a timely manner.

CHAPTER 1

INTRODUCTION

1.1 Literature review of semi-crystalline polymer structure-property relationships

Semi-crystallinity is a unique and important structural characteristic of thermoplastic polymers. Due to multiple relaxation times and chain entanglements, thermoplastic polymers form semi-crystalline structures through crystallization. In general, isothermal crystallization at low pressure tends to develop a lamellar structure with periodic crystalline and amorphous regions [1]. Various diffraction [1-3] and spectroscopic [4, 5] characterizations have confirmed existence of the lamellar structure.

Owing to the significant structural and behavioral differences between the crystalline and amorphous regions, such as the orientation ordering, tensile modulus and relaxation time, molecular level mechanisms of semi-crystalline polymer deformation have been debated over the decades. Early attempts tried to fit semi-crystalline polymer deformation using a universal rubber elasticity model [6], in which the chain entanglements are concentrated in the amorphous region and responsible for the inelastic strain. Such models treated the crystallites as rigid bodies without structural details and rotational degrees of freedom during deformation. For example, Bartczak et al. [7, 8] carried out a series of X-ray scattering and transmission electron microscopy experiments on compression and shearing deformation experiments on semi-crystalline polyethylene samples. Direct evidence of interlamellar sliding and intralamellar shearing were found from his investigation. Peterlin and Meinel [9-11] investigated the plastic deformation of polyethylene samples by small-angle X-ray scattering (SAXS) and wide-angle X-ray scattering (WAXS). By comparing the intensity changes of the meridional and equatorial

scattering peaks, a microfibril model were proposed and a lamellar to fibrillar transition was suggested based on scattering data [12].

To incorporate the stress-strain relation of linear polymers into a general viscoelastic model, Strobl and colleagues [13-16] examined the true stress-strain behavior of linear polymer samples. From extensive loading-unloading tests, some intrinsic critical points were identified [17] which occurred at certain true strain levels that were independent of temperature, strain rate and degree of crystallinity. Experiments were carried out at different temperatures and strain rates, while the crystallinity was controlled through adjusting the co-monomer content, as was specified in Table 1-1.

Table 1-1 Properties of PE samples under tensile study. [17]

Sample	Type	Crystallinity (%)	Co-unit content
PE27	Linear polyethylene	76	
FM1570	Poly(ethylene-co-octene)	38	7.5 wt % counits
PEVA12	Poly(ethylene-co-vinylactate)	33	12 wt % counits
PEVA18	Poly(ethylene-co-vinylactate)	25	18 wt % counits
PEVA27	Poly(ethylene-co-vinylactate)	15	27 wt % counits

In the model [17], two linear regions in the initial stages terminated with “double yielding points”, while the third critical point was associated with the onset of fibrillation. The fourth point was believed to have originated from chain disentanglements, and initiated cracking and failure. As is shown in Figure 1-1a, the orientation of the polymer chains

during deformation tests was indicated by the anisotropy of the two dimensional (2D) X-ray diffraction diagram at various strain levels. In Figure 1-1b, for different linear polymeric systems, the critical points B (yielding) and C (hardening) were identified, at same true strain levels of 0.1 and 0.6, respectively. The strain-softening region was attributed to the onset of cooperative motion of crystallites, while the strain-hardening region was initiated by the formation of fibrillar structure after the breakdown of crystal lamellae.

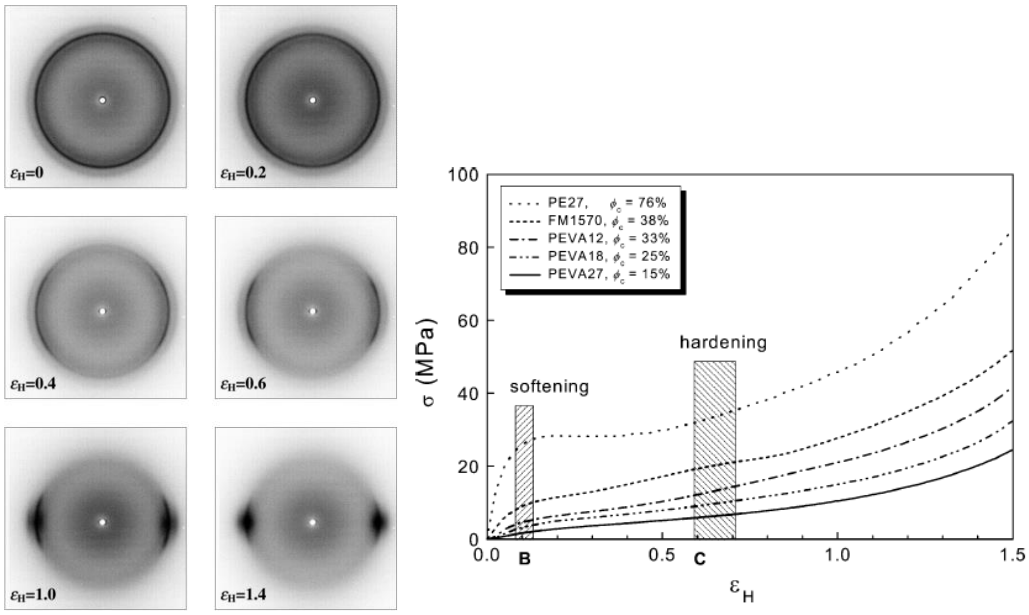

(a) **(b)**

Figure 1-1 (a) PEVA27: WAXS patterns measured for the indicated strains. The fiber axis is oriented in the vertical direction [17], (b) Relation between the true stress and the true strain for the five samples under study, obtained by video-controlled stretching experiments at a constant strain rate ε = 0.005 s^{-1}. Measurements were carried out over similar ranges, away from the points of fracture. [14]

Morphological evolution of the deformation process is accessible using in-situ synchrotron X-ray techniques, the pioneering work by Samon, Schultz and Hsiao et al. [18, 19] on structure development in polymer melt spinning involving both SAXS and WAXS showed that the melt spinning process was a combination of the crystallization (early stage) and uniaxial deformation (drawing stage). In the case of polyethylene, the amorphous lamellar thickness obviously increased, while the crystal lamellar thickness remained constant at slow or moderate take-up speed, and was reduced at higher speed. Different behaviors of the lamellae were attributed to the large difference in their tensile modulus.

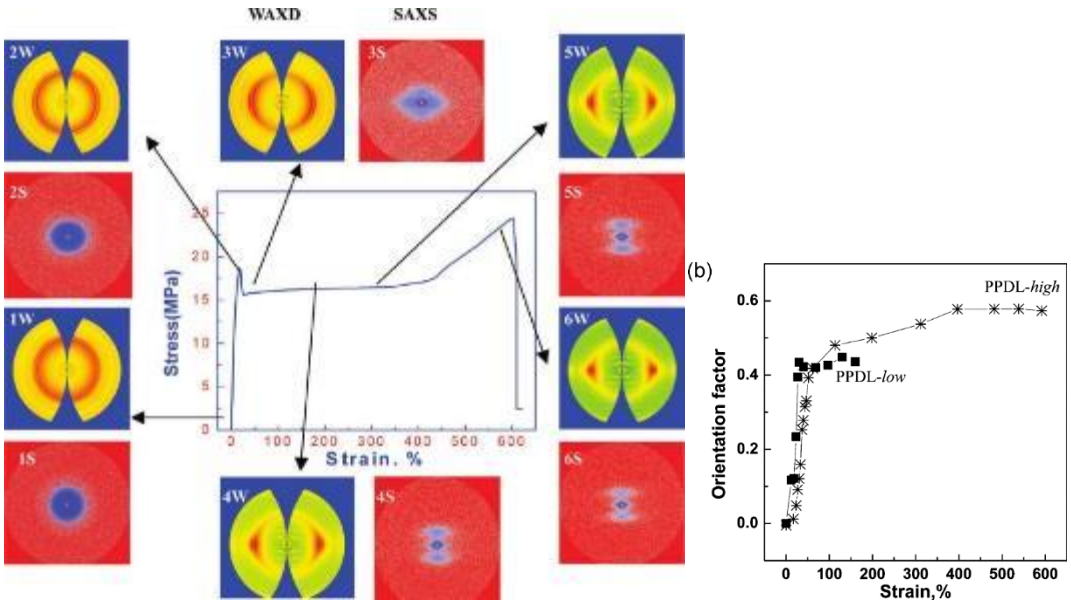

Figure 1-2 (a) Engineering stress-strain curve and selected 2D SAXS and WAXD patterns acquired during uniaxial tensile deformation of PPDL at room temperature. (b) Hermans' orientation factor of the crystal chain axis determined as a function of strain for PPDL-low and PPDL-high, based on orthorhombic (from the (001) diffraction peak) unit cell systems. [20]

A later work also calculated the Hermans' orientation factor [20] of the crystal chain

axis as a function of strain. Figure 1-2 showed both the in-situ WAXD and SAXS patterns of the uniaxial tensile test on a linear polyethylene-like polymer, Poly(ω-pentadecalactone) (PPDL) together with the engineering stress-strain curve. As is shown in Fig. 2b, the chain orientation increased drastically along the stretching direction in the early stage of deformation, followed by a relatively stable stage. It was pointed out that even at high strain certain off-axis orientation was maintained for the system, which was attributed to the entangled network structure.

Tang, Jiang and Men et al. [21] studied the uniaxial deformation of over-stretched polyethylene samples, and observed a decrease in tilt angle and increase in fibril length with increased strain. A later study [12] indicated lamellar to fibrillar transitions in the tensile deformation of high-density polyethylene. The breakdown of the initial laminated crystallites and fibril formation during tensile deformation were identified by the peak shift in the SAXS patterns.

Stribeck et al. [22] developed a multidimensional mathematical tool, the chord distribution function (CDF), based on data analysis of the SAXS pattern, which strongly enhances the sharpness of surfaces and distinguishes the correlation between the surface orientations. It presents autocorrelations of surfaces from the scattering objects in a way that positive values characterize distances between surfaces of opposite direction, negative values indicate distances between surfaces of the same direction (see Figure 1-3). Hence, the positive peaks around the origin characterize size distributions of the primary domains. In the case of semi-crystalline polymers, the sizes of crystalline and amorphous domains are shown. The negative peaks show the long period of a lamellar structure.

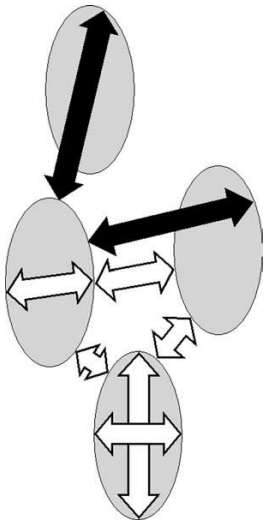

Figure 1-3 Information indicated by CDF: In any particular structure, positive values of the CDF represent correlations of interfaces with opposite direction (light arrows); negative values represent correlation of interfaces with the same direction (dark arrows). [22]

The crystallization behavior from a highly oriented melt [23] and the deformation process [24] were characterized by the CDF, accompanied by wide angle x-ray diffraction patterns and thermal analyses. Highly oriented crystals were found to have crystallized from the highly-oriented melt. The lamellar-to-fibrillar transition and co-existence of lamellar and fibrillar domains were also confirmed. Figure 1-4 illustrates the lamellar-to-fibrillar transitions at hot and cold stretched isotactic polypropylene (PP) samples. The initial stage at relatively low strains features the reorientation of the crystallites with their chains aligned to the stretching direction, followed by the fracture of lamellae. Depending on test temperatures, the structures are different at larger strains. At a high temperature (130 °C) (see Figure 1-6), due to the higher chain mobility, the oriented chains after

lamellae breakdown are able to re-crystallize into smaller crystallites, which maintain certain periodicity in the tensile direction (Figure 1-4e). In contrast, at room temperature (see Figure 1-5), the chains aligned in tensile orientation are not able to fully re-arrange during stretching. A transverse periodic structure with highly oriented and less-ordered amorphous regions is formed, as is illustrated in Figure 1-4g.

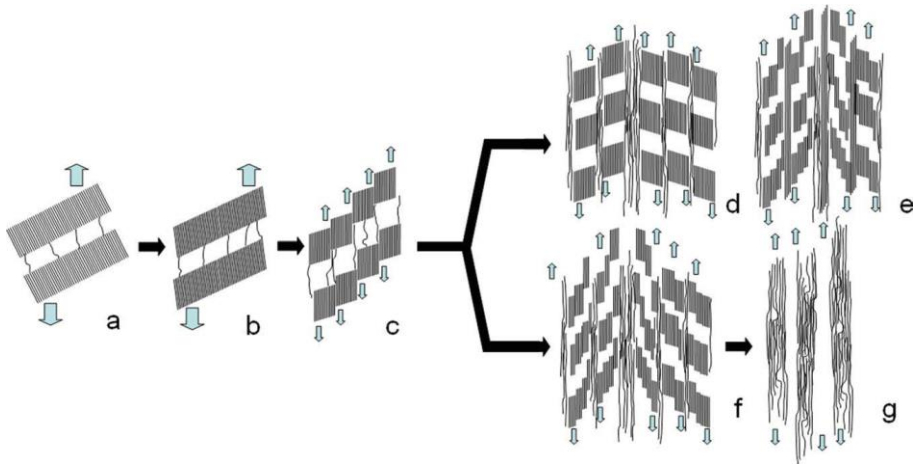

Figure 1-4 Sketch of the transformations of the oriented chains during deformation, with additional amorphous chains in between: (a) Lamellae with some tie-molecules, (b) elastic shear-deformation of lamellae under small load and reorientation with respect to the loading direction, (c) fracture of lamellae into smaller blocks due to local stress concentration apparently caused by tie molecules, (d) stretched aligned, but not recrystallized chains between the bocks during stretching at higher temperatures, (e) some of the fibrillar arranged molecules crystallize, final stage in the case of hot stretched PP, (f) further dissolution of the blocks creating more extended chains at room temperature, and (g) finally, there are several strands of extended chains, not crystallized, with some amorphous regions in between, final stage in the case of cold stretched PP. [24]

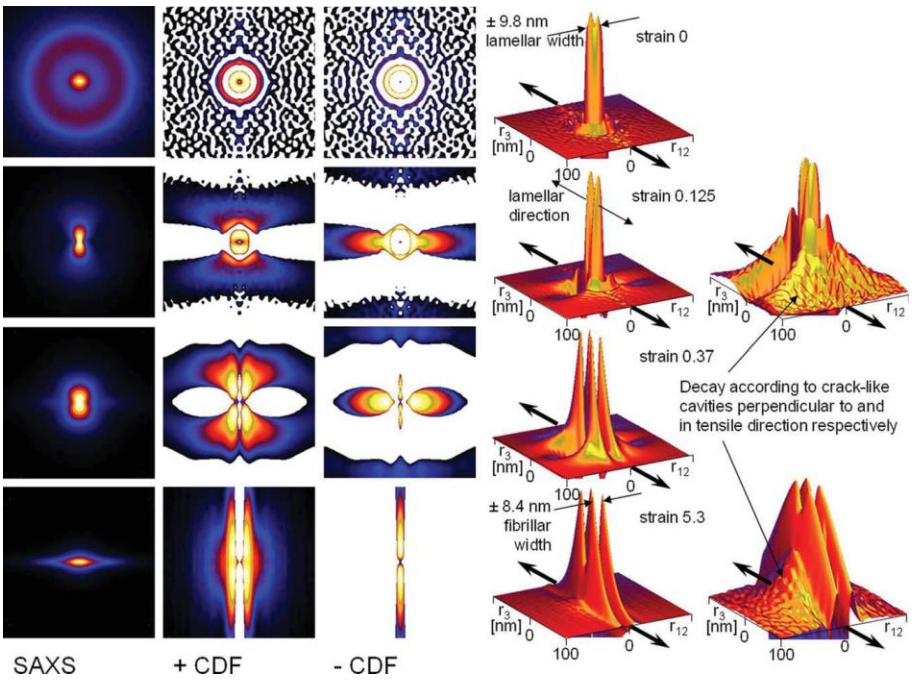

Figure 1-5 Deformation of iPP at room temperature, from left to right: SAXS patterns, positive and negative CDFs (always logscale, pseudo color) as well as a surface plot of the CDF's (linear scale and for two strains also log scale) at different strains ε= 0.0, 0.125, 0.37, and 5.3 (from top). Each square of the pattern covers a range -0.12 nm^{-1} < s_1, s_3 < 0.12 nm^{-1}, each square of the 2d-CDF covers a range of -100 nm < r_{12}, r_3 < 100 nm, fiber direction always vertical. The stretching (fiber) direction is indicated in the surface plots by arrows. [24]

As is shown in the 2D and surface CDF's of the SAXS patterns at different strains at room temperature (Figure 1-5), highly anisotropic structure was developed during uniaxial loading of initially isotropic structure. The yield point was identified at a strain of 0.125 and the fibrillation process was believed to initiate from a strain of 0.37. The lamellar

and transversal fibrillar widths were identified from initial and high strain conditions, respectively. Cavitation was also captured in the surface CDF. At a higher temperature of 130°C, the strained structure showed both transversal and longitudinal periodicity, even with higher orders of reflexes, which was speculated to be an effect of re-crystallization, as is demonstrated in Figures 1-4d, e.

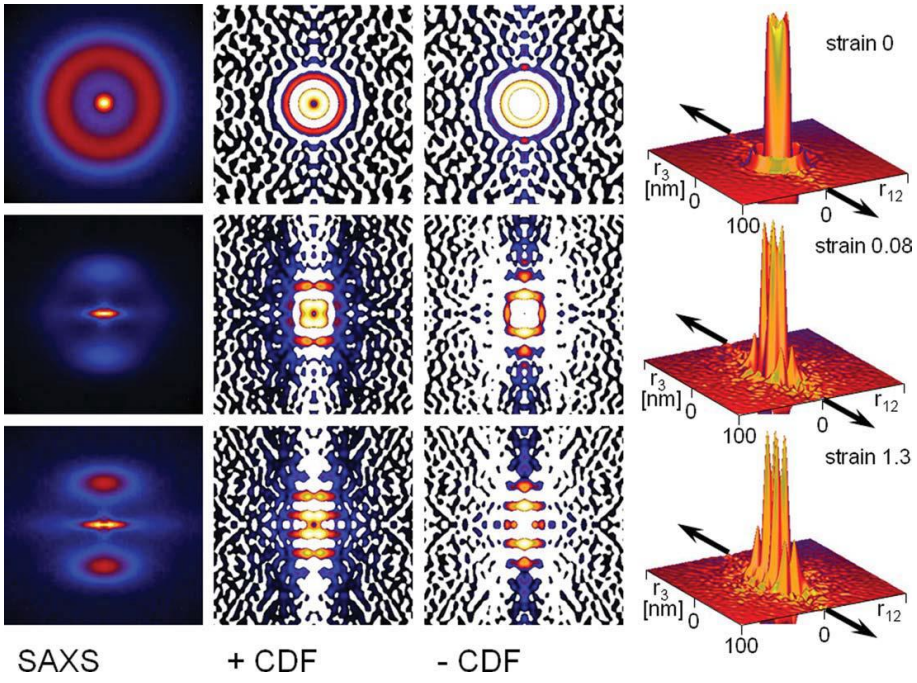

Figure 1-6 Deformation of iPP at 130°C, from left to right: SAXS patterns, positive and negative CDF's (always log-scale, pseudo color) as well as a surface plot of the CDF's (linear scale) at different strains ε = 0.0, 0.08, and 1.3 (from top). Each square of the pattern covers a range -0.12 nm^{-1} < s_1, s_3 < 0.12 nm^{-1}, each square of the 2d-CDF covers a range of -100 nm < r_{12}, r_3 < 100 nm, fiber direction always vertical. The stretching (fiber) direction is indicated in the surface plot by arrows. [24]

An injection molded sample with highly oriented crystalline regions was also investigated. Deformation tests in both the injection and transversal directions were performed. After structural evolutions, the fibrillar structure was obtained from both tests at room temperature.

Due to the structural complexity and long relaxation time, simulations of crystallization behavior from the polymer melt were seldom reported compared to the attention devoted to metallic and inorganic systems. Early attempts were based on the Monte Carlo (MC) approaches [25] on the high coordination lattice [26]. Molecular dynamics (MD) simulations [27] investigated single chain crystallization behavior in vacuum. Rutledge et al. were able to crystallize n-eicosane ($C_{20}H_{42}$) [28] and n-octane ($C_{80}H_{162}$) [29] chains from the melt state. Crystal growth kinetics were also studied.

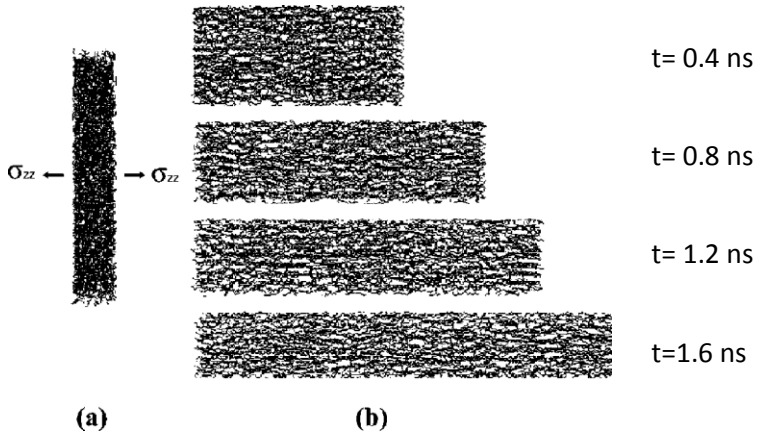

Figure 1-7 Snapshots of (a) amorphous melt and (b) pre-oriented melt at 425 K. From right top to right bottom, t=0.4, 0.8, 1.2, and 1.6 ns, respectively. [30]

The crystallization behavior for longer polyethylene-like chain lengths was also reported [30]. Chains with 400 repeat units from the unidirectional oriented melt (see

Figure 1-7) were observed to partially crystallize within 30 nanoseconds (ns) into a lamellar semi-crystalline structure. The initial structure was an amorphous polymer melt at 425 K, before stretching with a unidirectional stress σ_{zz}=100 MPa.

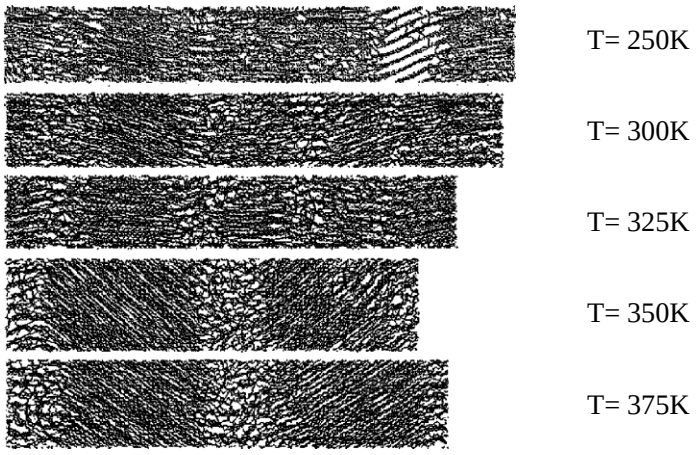

Figure 1-8 Snapshots at 30 ns from the simulations of 20 C400 chains quenched from 425 to 250, 300, 325, 350, and 375 K, in order from top to bottom. [30]

The system was quenched at atmospheric pressure to different crystallization temperatures. As is shown in Figure 1-8, snapshots of initially stressed systems after 30 s crystallization at 250, 300, 325, 350 and 375K were taken, from top to bottom. Crystallization occurred at all temperatures, but thick crystals with well-defined lamellar structure are only obtained at 350K and 375K. This is an indication of the optimized isothermal crystallization temperature to consider for future studies.

Similar approaches were also applied by Yamamoto [31] in a recent communication to simulate a fiber spinning process. The initial orientation imposed to the melt was believed to reduce the induction period of nucleation substantially, compared to that at the isotropic condition.

The mechanical properties of amorphous polymer samples have also been simulated using united atom MD simulations [32-34]. As is shown in Figure 1-9, true stress-strain curves were calculated from the uniaxial deformation tests, with a fixed strain rate in the direction of stretching and zero lateral pressure. Although the strain rate of 10^{10} s^{-1} is orders of magnitude higher than the experimental values (a general limitation of the MD simulations), the overall characteristics of the response of polymers to deformation were captured, such as the initial elastic deformation, the yield point and the strain hardening. The morphological changes of the homogeneous deformation at atomistic detail are also shown right to the stress-strain curve.

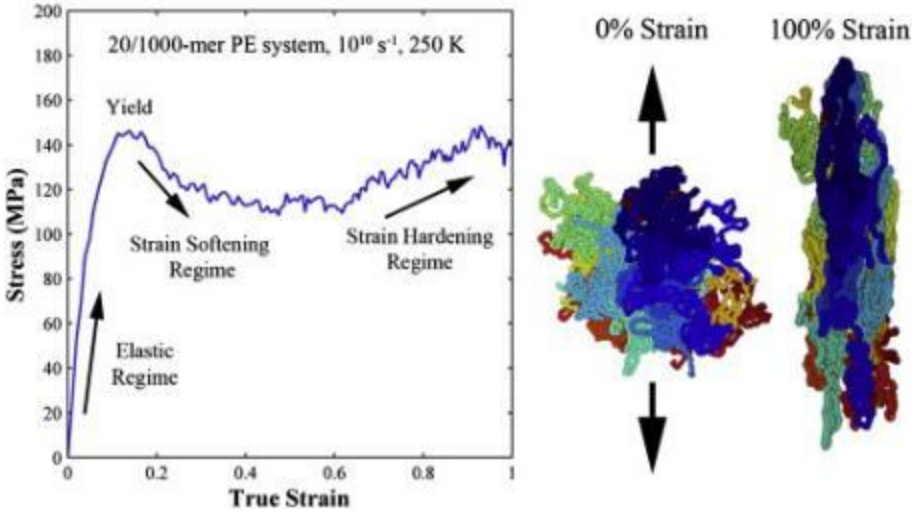

Figure 1-9 Stress-strain response of a polyethylene (PE) glassy polymer deformed in uniaxial tension at strain rate of 10^{10}/s and temperature of 250 K. The accompanying images (right) show the polyethylene structure after equilibration and at 100% true strain (colors represent united atoms on separate chains). [34]

In most experimental studies and applications, polyethylene samples prepared for deformation tests are semi-crystalline. Owing to the structural complexity of the multi-

phase nature of the system, almost all the previous studies [35-37] have adopted an MC approach which fixes the crystalline layers and only relaxes the amorphous part. Interfacial structures and deformation mechanisms have been examined. A recent publication on the mechanical property of a semi-crystalline polymer [37] allowed all the united atoms of the initial structure to relax. The initial structure was built using an MC algorithm [35], which consists of two crystalline lamellae with fixed distance, and certain number of "bridge" and "tail" connections of amorphous regions in between the crystals. Figure 1-10a shows the initial structure built to study the interfacial property of the semi-crystalline structure. A similar structure (see Figure 1-10b) was also applied to carry out MD simulations of the constant volume tensile test.

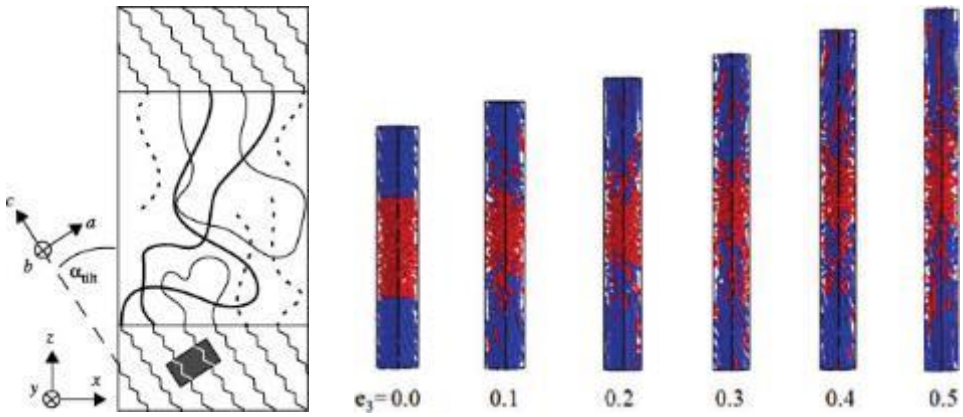

(a) (b)

Figure 1-10 (a) Schematic diagram of the simulation box based on an MC Algorithm, showing the two crystalline lamellae and the interlamellar phase in between, which consists of loops (thin solid lines), bridge chains (thick solid lines), and tails (dashed lines) [35]; (b) volume-conserving deformations. [37]

Hudzinskyy and Michels et al.[38] performed MD simulations on atactic-polystyrene thin films with thicknesses ranging between 1 nm to 10 nm supported by both strongly interacting and weakly interacting substrates. Three different layers in the near-substrate, middle and surface regions were defined based on density differences for films thicker than 2 nm (see Figure 1-11). Slight orientation of the polymer main-chain and benzene rings were found only at the near-substrate areas. The glass transition temperatures of the individual layers and the entire film were also explored with respect to different film thicknesses. For polystyrene thin films of thicknesses less than 10 nm, a decreasing trend of average T_g was found with a decreasing film thickness. Local density distribution and Herman's orientation distribution of individual layers were calculated to assist physical property predictions during the research, which showed certain practical values. However, it was restricted to the amorphous polystyrene thin film. Semi-crystalline polymeric thin films were not discussed in the context.

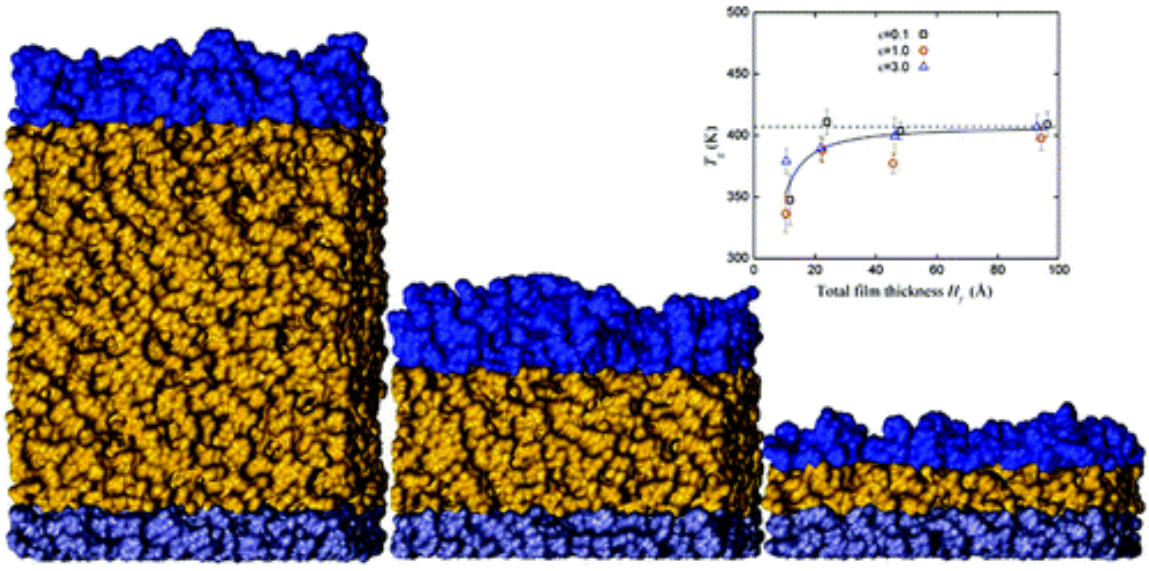

Figure 1-11 Thickness dependence of glass transition temperatures in atactic-polystyrene thin films of 9.5 nm, 5 nm and 2.5 nm. [38]

1.2 Literature review of liquid crystalline polymers and elastomers

Liquid crystalline elastomers (LCEs) have attracted considerable interest over the decades owing to their combined intriguing properties of anisotropic liquid crystalline mesogens and flexible polymeric networks [39] [40] . The mesogenic moieties are either rod-like or disc-like and can display certain liquid crystalline ordered states in certain temperature range. The flexible networks are generally amorphous. The mesogenic units can be attached either as side chains to the monomer units yielding "side chain elastomers" (see Figure 1-12 a, b) or directly linked together within the polymer backbone yielding "main chain elastomers" (see Figure 1-12 c, d). An additional variation of the molecular architecture is given by connecting the mesogenic groups via different geometries, e.g., for rods via their long axis ("end-on") as shown in Figure 1-12 a, c or via their short axis ("side-on") (see Figure 1-12 b, d). All these different geometries directly and specifically affect the liquid crystalline state of order and the polymorphism.

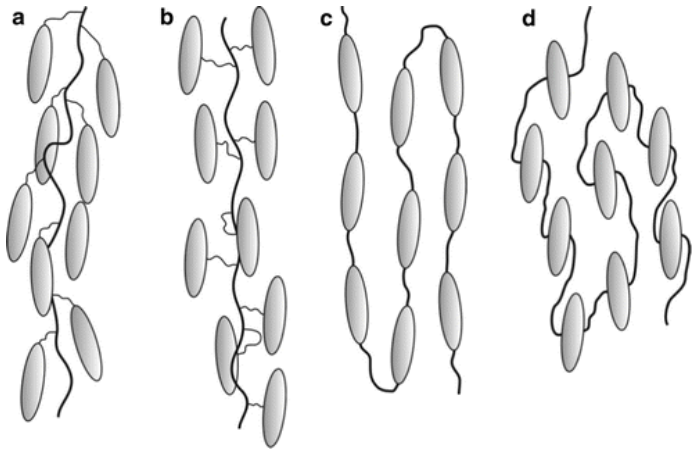

Figure 1-12 Different attachment geometries for the synthesis of LCEs: side chain elastomers with end-on (a) or side-on (b) attached mesogenic side chains and main chain elastomers with mesogenic units incorporated end-on (c) or side-on (d) into the polymer main chain. [40]

Due to the regular arrangement of the mesogens along the polymer backbone, main chain polymers tend to form smectic or even crystalline phases. Despite more complex chemistries involved in synthesis, main chain LC elastomers have attracted many theoretical attentions due to the direct coupling of the liquid crystalline order and the polymer backbone conformation. The early-year predications of de Gennes were also based on main chain elastomers[41]. End-on polymers (or elastomers) (see Figure 1-12 a, c) tend to form smectic phases, the lateral linkage of the mesogenic units (see Figure 1-12 b, d) often prevents long range positional ordering and favors the formation of nematic phases.

A typical example is the two-step crosslinking process combined with a drawing process for polysiloxane based LCEs, which was introduced by Kŭpfer and Finkelmann [42] The alignment in the LCE network is formed in a cold drawing process followed by a second crosslinking process to lock in the monodomain liquid crystalline order.

Donnio and Finkelmann [43] introduced a simple and versatile synthetic route for the preparation of main-chain LCE. Instead of starting from pre-synthesized main chain polymers, this synthetic approach is based on a polyaddition reaction in solution via hydrosilylation of a divinyl substituted mesogen with tetramethyl dihydro disiloxane as additional flexible spacer to lower the phase-transition temperatures. As a crosslinker a cyclic pentasiloxane was used. A conceptual chain conformation of the main-chain LCE is sketched in Figure 1-13.

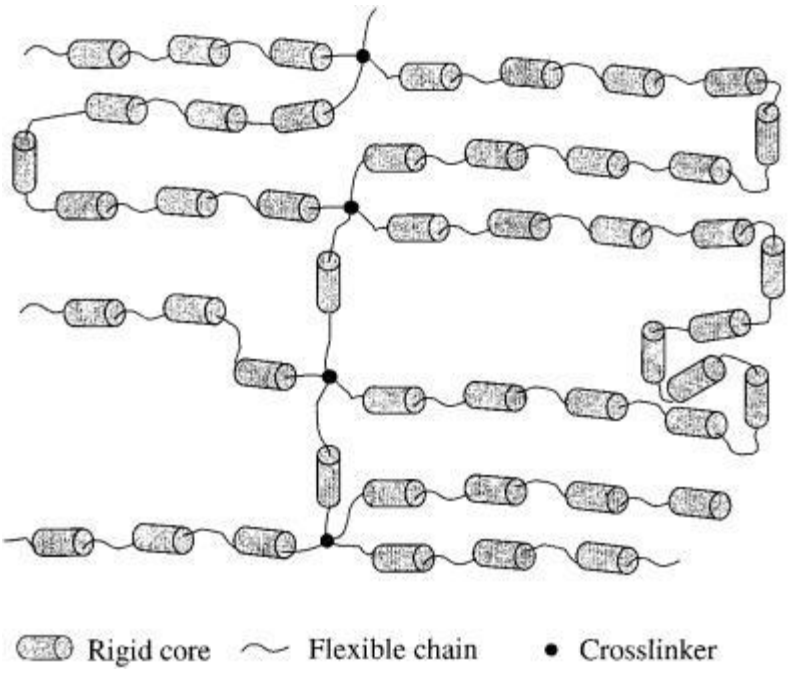

Figure 1-13 Schematic representation of the main-chain LCE. [43]

The phase behavior of the LCEs were also characterized by two dimensional X-ray diffraction (2DXRD) patterns. At 153 °C, in the isotropic state, the X-ray pattern (see Figure 1-14a) and the corresponding azimuthal intensity profiles (see Figure 1-14a') show two diffuse halos: one in the wide angle region, indicative of a complete orientational disorder of the mesogenic units, and another one in the small angle area, which corresponds to some degree of local positional ordering of the mesogenic units. At 110 °C, in the nematic phase (see Figure 1-14b,b'), the two half-crescents are smaller and confined in the equatorial plan and the two diffuse lines give way to a set of four Braggs peaks. This indicates that the mesogenic subunits are macroscopically aligned parallel to the axis of the applied stress. On further cooling, the nematic monodomain undergoes another phase transformation. At 55 °C, (see Figure 1-14c,c'), the wide angle half-crescents remain still

diffuse but are narrower, and the small-angle Braggs peaks become sharper, indicative of a layered phase, namely a smectic-C phase. The tilt angle (angle between the layer normal and the director) is ca. 45°, suggesting a Chevron structure.

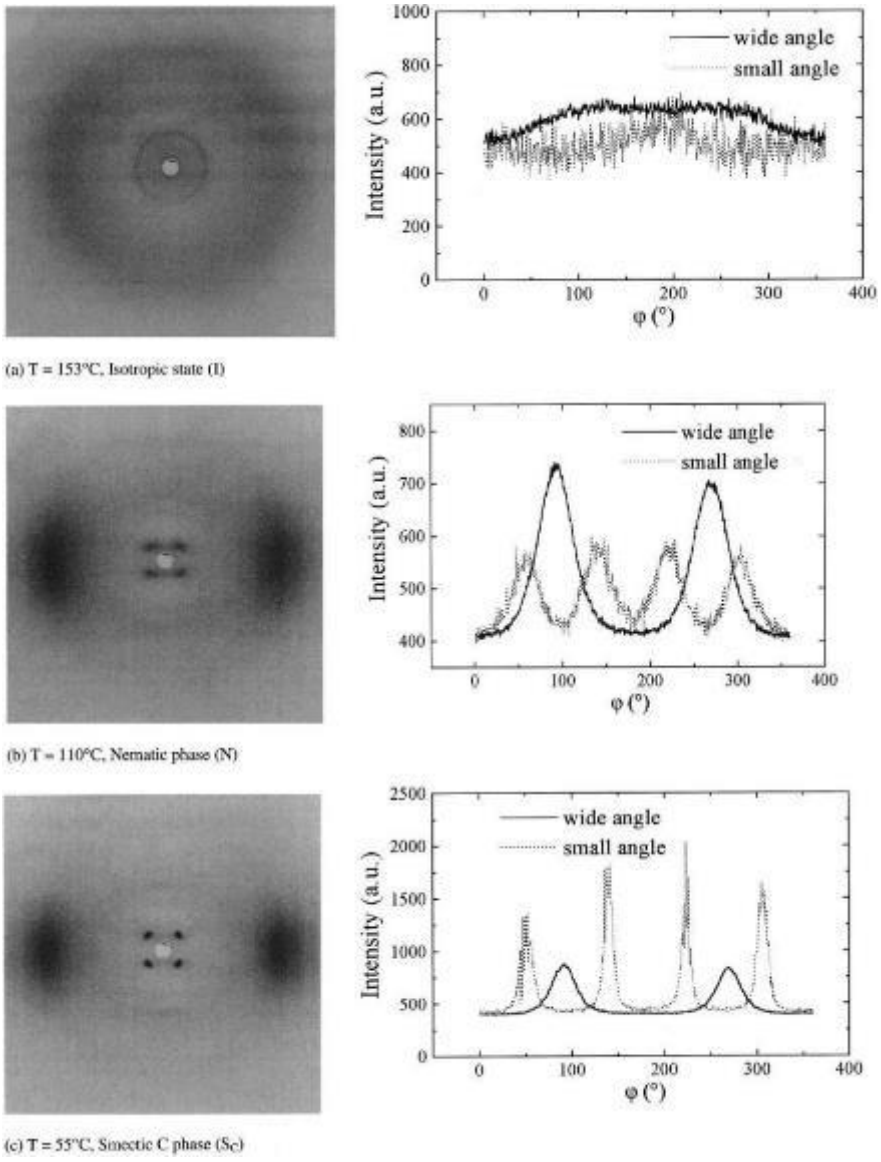

Figure 1-14 X-ray diffraction patterns (a, b, c) and the corresponding azimuthal intensity profiles (a′, b′, c′) at different temperatures of the LCE: (a) T= 153 °C, in the isotropic state; (b) T= 110 °C, in the nematic phase; and (c) T = 55 °C, in the S C phase. φ is the azimuthal angle [43].

Azobenzene-containing liquid crystalline elastomers are of particular research interest since it was successfully synthesized via one-pot chemistry[39] at the beginning of this century. Upon exposure to ultraviolet (UV) or visible light, the azobenzene moieties undergo reversible isomerization from *trans*- to *cis*-conformation, which results in photoinduced reorientation and deformation of the LCEs, and triggers significant changes in the LCEs' physical properties [44-67].

In addition to the change in shape and bending angle of azobenzene-containing LCE samples, stress change between fixed ends could also be monitored to quantify the contractive force generated by UV-irradiation.

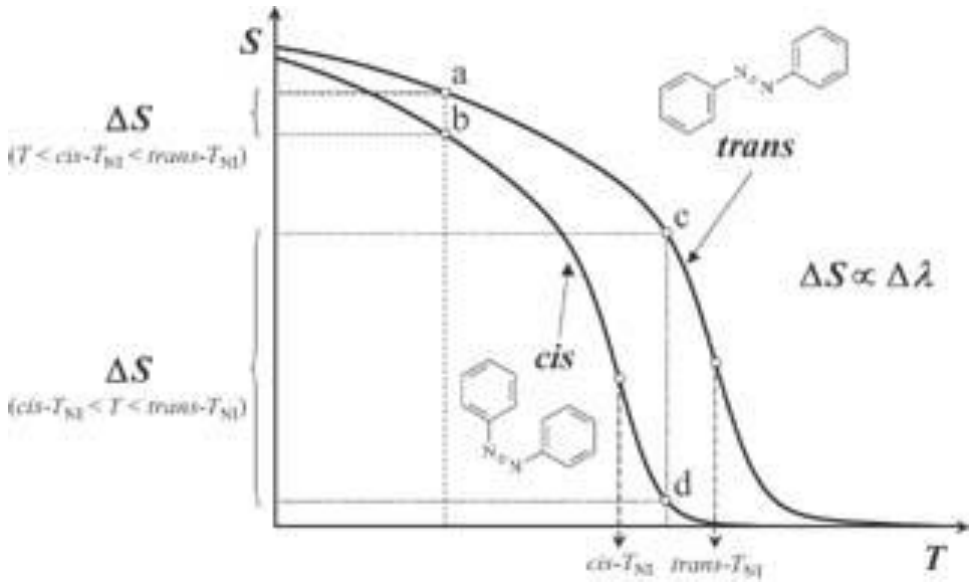

Figure 1-15 Order parameter (S) as function of temperature for a LCE containing azobenzene molecules. The *trans*-isomer stabilizes the liquid-crystalline phase and has higher clearing temperature (*trans*-T_{NI}), while the *cis*-isomer destabilizes the liquid-crystalline phase, reducing the local order, and shifting the clearing temperature to lower values (*cis*-T_{NI}). [68]

Sanchez-Ferrer and Finkelmann et al. studied the opto-mechanical effect of azobenzene-containing side chain LCEs [68]. The mechanical behavior of monodomain samples was studied under UV irradiation and in the darkness at different temperatures.

In an azobenzene-containing LCE, when the azobenzene compound is isomerized (from *trans* to *cis*), the local order parameter (S) and the nematic-to-isotropic phase transformation temperature (T_{NI}) decrease, causing a microscopic local disorder in the mesogens and a consequent change in the macroscopic length of the sample (see Figure 1-15). A big change in the macroscopic dimensions can be predicted in the vicinity of the T_{NI} due to the photo-isomerization process.

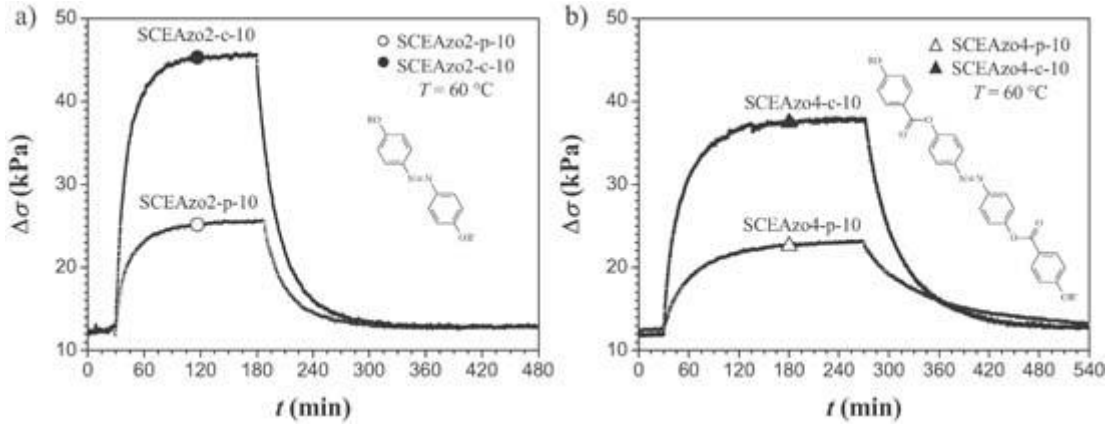

Figure 1-16 Opto-mechanical experiment at 60 °C on the samples (a) SCEAzo2-p-10 ($R = CH_3$, $R' = (CH_2)_4CH = CH_2$) and SCEAzo2-c-10 ($R = R' = (CH_2)_4CH = CH_2$) at $\lambda = 380$ nm), and (b) SCEAzo4-p-10 ($R = CH_3$, $R' = (CH_2)_4CH = CH_2$) and SCEAzo4-c-10 ($R = R' = (CH_2)_4CH = CH_2$) at $\lambda = 360$ nm. [68]

In the research, azobenzene-containing moieties with two or four aromatic rings were added either as crosslinker or pendant chain. The chemical structures are shown in the inset of Figure 1-16. At 60 °C, a maximum stress of 46 kPa was achieved by LCE sample with the two phenyl ring azobenzene derivative as crosslinker. The authors also found that by increasing the temperature, both photo- and thermal-isomerization processes were accelerated.

A recent publication shown that by increasing the crosslinking density (by shortening the polymer length between crosslinking points) the elastomer becomes more responsive than its corresponding low crosslinked counter partner [69], or than side-chain systems with a similar crosslinking density. [68]

As is shown in Figure 1-17 (a), the contractive force yielded inside the main-chain LCE sample with the azobenzene containing 10 mol% crosslinker (MCEAzo-10) reached 70 kPa. The kinetics parameters such as photo-/thermal activation energy and their respective relaxation time at different temperatures were also calculated. An acceleration of both photo- and thermal activated *trans-cis* isomerization were shown. For MCEAzo-10 the lifetime for photo-isomerization decreased from approximately one hour at 30 °C to eight minutes at 60 °C. The thermal isomerization lifetime was more than five hours at 30 °C but less than half an hour at 60 °C.

Figure 1-17 (b) shows the uniaxial thermal expansion of both samples, where the maximum length ratio λ at 20 °C is related to the crosslinking density and the inflexion point of each curve to the nematic-to-isotropic temperature T_{NI}. Thus, samples with low crosslinking density expand/contract more than those with high crosslinking density. The clearing temperature for the 10 mol% crosslinking density sample

(MCEAzo-10) is lower than the isotropization temperature of the 2.5 mol% crosslinked sample (MCEAzo-2.5) due to the fact that the isotropic crosslinker acts as an impurity, introducing some disorder and lowering the transition temperature.

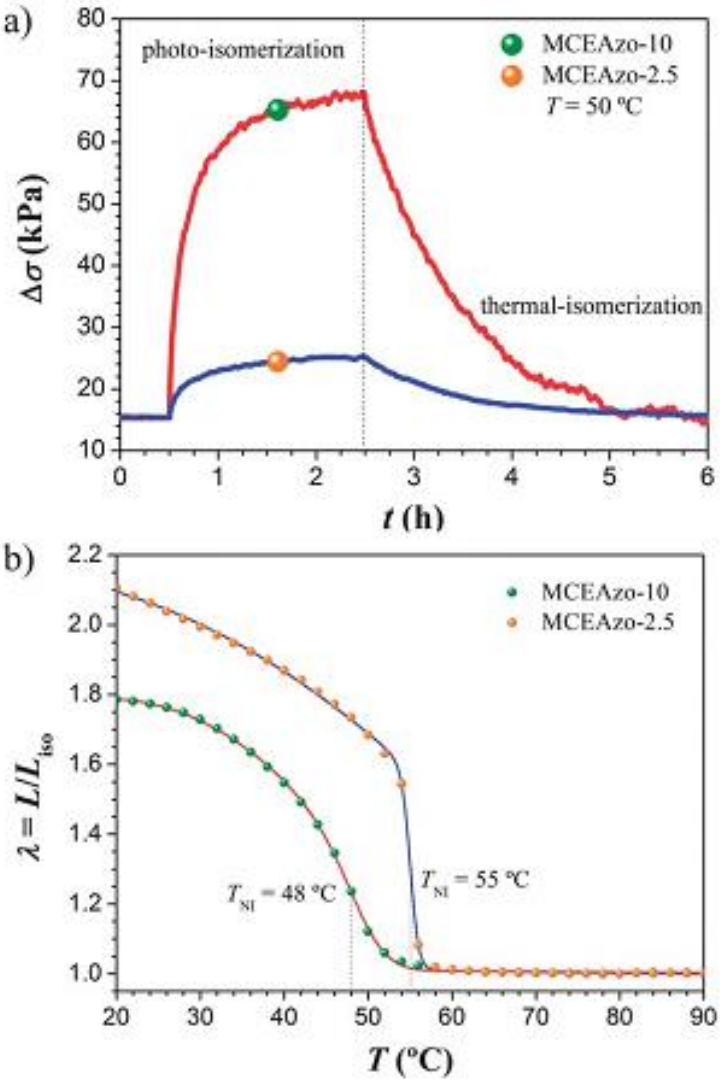

Figure 1-17 (a) Opto-mechanical experiment at 50 C on the samples MCEAzo-10 and MCEAzo-2.5 at l =380 nm. (b) Uniaxial thermal expansion (λ =L/L_{iso}) as a function of temperature for the two nematic MCLCEs. Note: both experiments were performed under a constant pre-load of F =0.5 g. [69]

Horada et al. [49] prepared photoresponsive actuators using the expansion–contraction ability of αCD–Azo gels. Figure 1-18a shows a component drawing of an αCD–Azo gel actuator. Irradiating the plate gel with ultraviolet light (λ=365 nm) from the left side bends the gel to the right, whereas irradiating the bent gel with visible light (λ=430 nm) from the same side for an hour restores the initial condition (see Figure 1-18b). Similarly, irradiating the plate gel from the right side causes the gel to bend to the left side, while irradiating with visible (Vis) light restores the initial state (see Figure 1-18c).

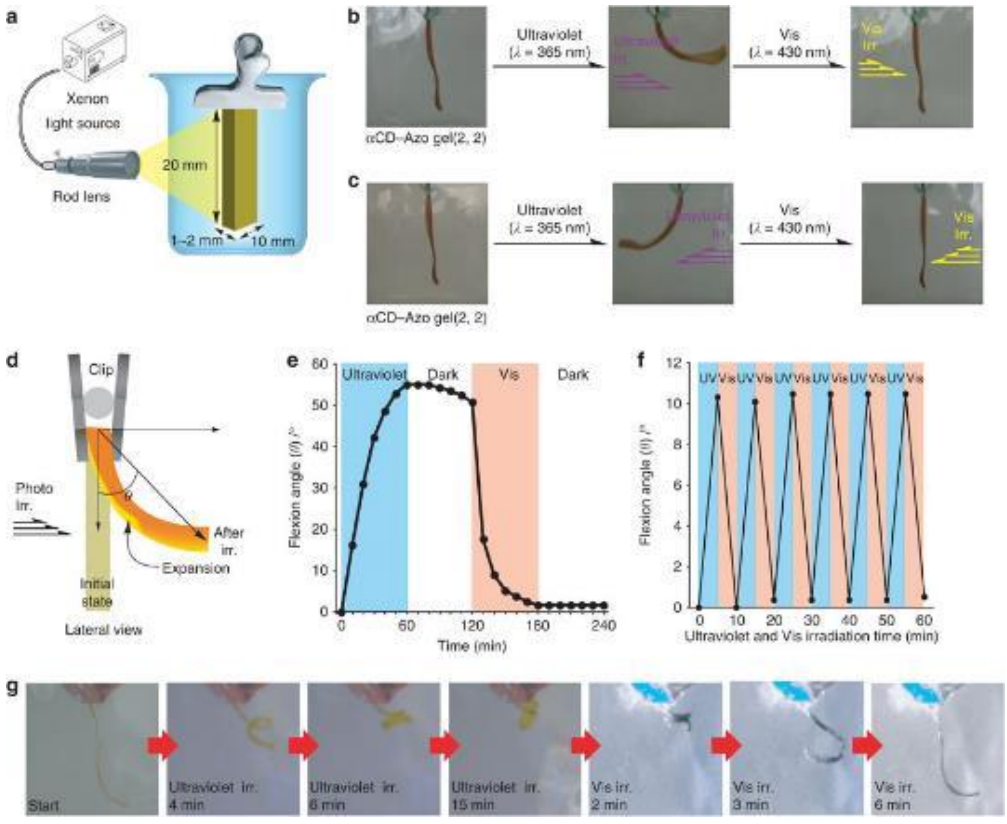

Figure 1-18 (a) Experiment set-up (b) (c) Irradiation protocol (d) Lateral view of sample hung with a clip. Flexion angle (θ) is defined here. (e) Plots of irradiation time versus the flexion angle (θ) in one actuation cycle. (f) Plots show repeated actuation. (g) Coiling and recovery of a ribbon-shaped sample. [49]

Figure 1-18e show one full cycle of the photo-actuation behavior in terms of flexion angle (θ). Blue and red areas denote ultraviolet irradiation and Vis irradiation, respectively. Blank area indicates dark storage without light irradiation. A plateau region can be reached after certain time of irradiation, which is comparable to Finkelmann's experimental findings [67-69]. Impressively, Figure 1-18f show good repeatability of the photo-actuation process. In Figure 1-18g, the ribbon-shaped gel turns to a coil by the irradiation of ultraviolet light (λ=365 nm) from the left side. The coil-shaped gel returns to the ribbon-shaped gel by visible light irradiation.

1.3 Motivation of research

Based on the above literature review on semi-crystalline and liquid crystalline polymeric systems, extensive research efforts has been put in the past decades in seeking order during structural evolution of polymeric systems and trying to establish the relationships between various ordering states and their corresponding thermodynamic and mechanical properties. Nevertheless, challenges still exist from both simulations and experiments in description of partially ordered polymeric systems due to the complexity of the systems and lack of effective analysis tools.

For the semi-crystalline polymers, the crystallization and deformation behaviors have been well documented in the literature. However, the molecular-scale detail of the morphological evolution is still not well understood due to limitation of length and time scale resolution of existing experimental tools. Molecular dynamics simulations are thus performed in this research to explore the mechanism of the phase evolution in molecular detail and predict mechanical property of semi-crystalline polymers crystallized from

different conditions. During the simulations and post-processing, various data analyses tools are developed and well testified to describe the partially ordered polymeric systems.

Although plenty of effort has been devoted to side-chain LCE systems [44, 49, 54, 55, 57, 62, 68-70], only several attempts on the main-chain LCEs have been reported, in which the azobenzene containing mesogens were added as a minor component of a copolymer or a crosslinker (10 mol% or less) [71-75]. However, due to the UV-inactivity of the major component, a high stress level induced by the *trans-cis* isomerization mechanism could not be reached.

Difficulties of synthesizing the high azobenzene content main-chain LCE systems were attributed to the rigidity of the azobenzene group as the mesogenic rod, introducing relatively high transition temperatures of the LCE films compared to the side-chain counterparts [68] and copolymers with a softer component [71-73]. More structural regularity that has been brought to the LCE system of a main-chain conformation would also tend to form smectic-C layers [73] compared to the less-ordered nematic LC phase exhibited by most side-chain LCEs. At room temperature, smectic-C LCEs have long relaxation time[71], which is considered a disadvantage in certain application areas such as actuation. It is necessary to use the highest purity of the starting materials and accurately tuned experimental conditions [73]. The azobenzene-containing mesogen homopolymeric MCLCE with 100 mol% of active group was seldom reported.

There is a strong demand on the development of main-chain LCE both from the applications perspective in seeking novel, highly efficient photo-responsive materials and from the theoretical interest in the direct correlation of the molecular scale orientation to the macroscopic order of a polymeric system. Since the particular category of the LCE is

rarely reported experimentally, this part of research started from the experimental efforts in preparation of both azobenzene-containing organic compounds and liquid-crystalline elastomers with the compounds as mesogenic groups.

1.4 Structure of the dissertation

This dissertation is organized as follows. After a general review of the research in the area of structural analysis and property prediction in semi-crystalline and liquid crystalline polymeric materials in Chapter 1, simulation and data-analysis methods to be applied in the research are presented in Chapter 2, which include the generation of initial structure using a modified diamond lattice code, molecular dynamics simulation details such as potentials, force fields and simulation protocols as well as the definition and calculation of the Hermans' orientation parameter and two-point statistics.

As a benchmark study, the dynamics of single polymeric chains are presented in Chapter 3, evidences show that under suitable thermodynamic conditions a single polymeric chain in vacuum with enough length could form a well-developed crystallite. This finding inspires the study of bulk crystallization properties of multiple polymer chains in the condensed state, which are described in detail in Chapter 4. The structural evolution during deformation of quasi-equilibrium semi-crystalline structures obtained in Chapter 4 are studied in Chapter 5, in addition to the mechanical property predictions.

In Chapter 6, the applications of two-point statistics in structural quantification of the semi-crystalline structures at different stage of deformation are illustrated. Chapter 7

discusses the recovery behavior of the as-deformed structures, using the tools developed in Chapters 4-6.

In Chapter 8, crystallization morphologies of semi-crystalline free-standing and supported thin films are described. Surface and sub-surface morphologies such as density and Hermans' orientation distribution of thin films with free-surfaces are traced. The polymer chain morphology near a strong interacting surface is also investigated. Finally, the behavior of a thin polymer layer between parallel sheets is studied, including the behavior under a shearing force between parallel sheets.

Experimental results of structural analysis of novel liquid crystalline polymers are discussed in detail in Chapter 9. Synthetic route, characterizations, polydomain to monodomain transition and device fabrication of novel azobenzene-containing main-chain liquid crystalline elastomers are presented. Order parameters of the samples at different stretching ratios are calculated from two-dimensional X-ray diffraction patterns, which would bridge the experimental finding with simulations results in tracking the order in the liquid crystalline systems.

CHAPTER 2

SIMULATION AND DATA-ANALYSIS METHODS

2.1 Generation of initial structure

The initial polymer structures were generated using the diamond lattice algorithm as described by Shepherd [76]. The original algorithm was targeted at generating a reasonable initial structure for a random bulk polymeric system with three-dimensional periodicity. However, proper modifications to the code could also meet the need to generate non-periodic systems such as a single chain in vacuum or a nanocluster of polymer chains. Of particular interest are also systems with one or two dimensional periodicity, e.g. thin films or fibers, which can be generated as well.

The method is successfully tested to efficiently produce a high density initial configuration with a low energy, near equilibrium state. The controlling factors include the distribution of rotational isomeric states, end-to-end distances, radius of gyration, number of atoms per molecule, number of molecules in the system, and the system density. To resemble the carbon-carbon bond angle, a diamond lattice is applied to provide possible sites for the united atoms molecules. For each molecule, the site for the first atom is picked randomly on the diamond lattice, followed by the growth of chain atom-by-atom on the neighboring sites, based on the density, energy and RIS state. After the atomic positions are mapped on the diamond lattice, an NPT simulation is performed for 1 nanosecond at 500 K and atmospheric pressure, to generate a well-equilibrated polymer melt.

2.2 Molecular dynamics simulation methods

Molecular dynamics simulations were carried out with the large-scale atomic/molecular massively parallel simulator (LAMMPS) [77]. Parallel processors of the college of computing at the Georgia Institute of Technology were accessed for large scale computation, with a 53-node, 106-core Dell PowerEdge 1850 Linux cluster with dual Pentium4 Xeon EMT64 processers using Infiniband interconnects and Gigabit Ethernet. The visualization of molecular morphologies was realized by VMD (Visual Molecular Dynamics) software, which is developed with NIH support by the Theoretical and Computational Biophysics group at the Beckman Institute, University of Illinois at Urbana-Champaign. Data post-processing applied Microsoft Excel and Matlab codes.

The united atoms force field first developed by Paul et al. [78] and revised by Waheed et al. [28] were applied throughout the research, which has been proven to be accurate in predicting physical properties on polyethylene melt [78], olegomer [28] and polymer crystallizations [30] as well as uniaxial constant volume deformation [37].

Harmonic potentials were used for both bond stretching and bond bending interactions.

$$E_l = k_l (l - l_0)^2, \tag{2-1}$$

$$E_\theta = k_\theta (\theta - \theta_0)^2, \tag{2-2}$$

where k_l =1.46×10^5 kJ/mol·nm^2, l refers to the bond length, and l_0, the average bond length, is 0.153 nm. k_θ =251.04 kJ/mol·rad^2, and θ, the bond bending angle, has its equilibrium value θ_0 at 1.23 rad.

The bond torsion potential is described as

$$E_{\varphi} = \frac{1}{2}[k_1(1-\cos\varphi) + k_2(1-\cos 2\varphi) + k_3(1-\cos 3\varphi)], \quad (2\text{-}3)$$

where k_1 =6.69 kJ/mol, k_2 =-3.63 kJ/mol and k_3 =13.56 kJ/mol, φ is the torsion angle.

The Lenard-Jones potential was adopted for the non-bonded interactions

$$E_{LJ} = 4\varepsilon\left[\left(\frac{\sigma}{r}\right)^{12} - \left(\frac{\sigma}{r}\right)^{6}\right], \quad (2\text{-}4)$$

where ε =0.469 kJ/mol and σ =0.401 nm, the truncation length of non-bonded interactions was chosen to be 1 nm.

2.3. Structure Quantification Approaches

2.3.1 Density and Hermans' orientation distributions

Density is a most common yet effective way in characterizing multi-phase materials, either in macroscopic scale or in the nano-scale. For semi-crystalline polymers, the amorphous regions have lower densities than the crystalline regions. Based on this, the density distribution with respect to the axis of interest (e.g. direction of pre-orientation) is taken to indicate structural organizations.

In addition to density distribution based on local atom concentrations, the orientation of local chain vectors and their ordering are also important in the conversation of pre-oriented melt crystallization and uniaxial deformation test.

As a popular tool in describing both general and local polymer chain orientations, the Hermans' orientation S [79, 80] is defined as

$$S = \frac{3}{2} < \cos^2\theta > -\frac{1}{2} \quad (2\text{-}5)$$

where θ refers to the angle between a chain vector and the direction of interest (in this

particular case, the uniaxial stretching direction z is chosen as the reference). For each of the non-chain-end i^{th} united atom, a corresponding chain vector is defined as the vector between the i-1^{th} and the i+1^{th} united atoms.

Another Hermans' orientation S_{ij} is defined to capture the local ordering and different crystal orientations. Rather than a specified direction, each chain vector is calculated once as a reference, and the average Hermans' orientation of a domain is recorded.

2.3.2 Two-point statistics

For a heterogeneous material system with multiple phases, the notion of a structure function $m(\boldsymbol{x}, h)$ has been introduced to capture the stochastic nature of the description of the material internal structure [81, 82]. Mathematically, $m(\boldsymbol{x}, h)$ is defined [83] as

$$m(\boldsymbol{x}, h)dh = \frac{dV}{V}\Big|_{\boldsymbol{x}, h} \tag{2-6}$$

where h refers to the local state (e.g., chain orientation),and V is a small volume element with its center position at $\boldsymbol{x}$. Physically, $\frac{dV}{V}$ is the volume fraction of V occupied by local states around h within a variation of dh. Implicit in Eq. (6) is the normalization for the structure function in any given region Ω, i.e.,

$$\frac{1}{vol(\Omega)} \int \int \int_{\Omega} \ldots \int m(\boldsymbol{x}, h) dh d\boldsymbol{x} = 1 \tag{2-7}$$

The two-point spatial correlation function describing a higher-order probability distribution is then expressed by[81, 82]

$$f(h, h'|\boldsymbol{r}) = \frac{1}{vol(\Omega|\boldsymbol{r})} \int \int \int_{x \in \Omega|\boldsymbol{r}} m(\boldsymbol{x}, h) m(\boldsymbol{x} + \boldsymbol{r}, h') d\boldsymbol{x} \tag{2-8}$$

Physically, the 2-point spatial correlations reflect the probability density associated with

finding local states h and h' at the ends of a vector r thrown randomly into the material structure. Consequently, when $h=h'$, these reflect autocorrelations, and when $h\neq h'$, they reflect cross-correlations.

For the particular systems of interest considered here in the thesis, a periodic box (Ω) is meshed into 20×20 pixel cells. The crystalline and amorphous phases are defined by the overall Hermans' orientation of a given cell, with a threshold at 0.6. In other words, one mesh cell is either in microstructural state h (crystalline) or h' (amorphous). In a discrete description, each periodic box is represented by a 20×20 matrix of 1 (crystalline) and 0 (amorphous). The autocorrelation of the crystalline phase and the cross-correlations between the crystalline and amorphous phases are calculated for various samples at different stages of crystallization and processing conditions. The data are presented in 2D spectra corresponding to the simulation box shape and size. The morphological evolutions of different systems are well characterized by the 2D two-point correlation spectra.

CHAPTER 3

SINGLE CHAIN DYNAMICS

As a benchmark study, single chain dynamics is performed in vacuum to explore the chain behavior without restrictions from external force or other chains. Single linear polymeric chains consisting of 200, 800, 4000 and 8000 repeat units are studied, covering a wide range of molecular weights. The morphological features after relaxation of single chains of different lengths would further guide the simulations of more complex polymeric systems such as a film or a bulky piece.

3.1 Simulation details

The initial structures are generated with different targeted chain lengths without any periodic boundary conditions, i.e. an isolated single chain is to be relaxed in vacuum without any influence from other force field. The systems are held at 375 K by Nose-Hoover thermostat [84-86] for 10 ns in the condition to reach a quasi-equilibrium state.

3.2 Relaxation and crystallization morphology of single chains of different length

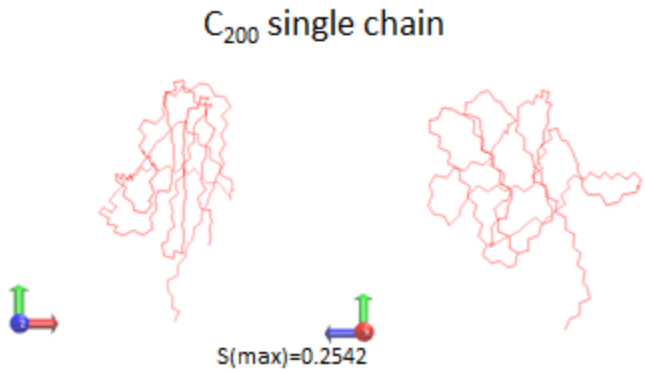

Figure 3-1 A single chain consisting of 200 repeat units after relaxation at 375 K.

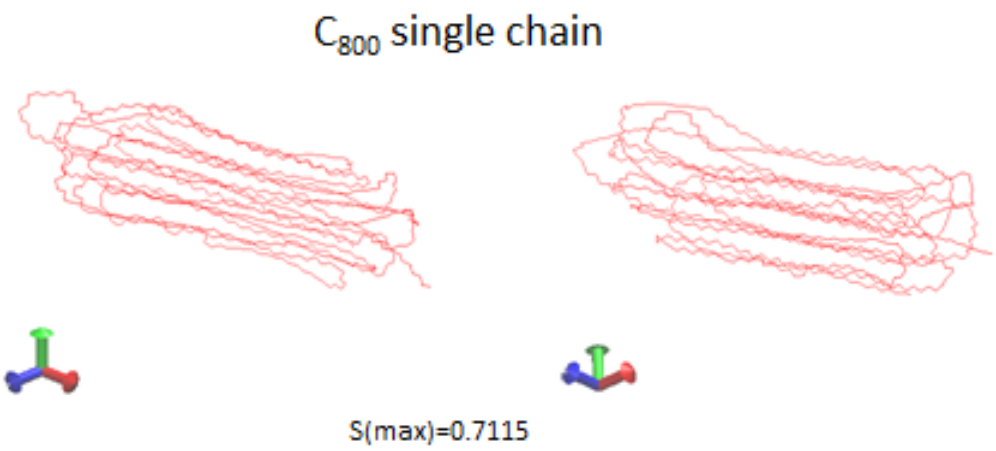

Figure 3-2 A single chain consisting of 800 repeat units after relaxation at 375 K.

As is shown in Figure 3-1, a single short chain consisting 200 repeat units is build and well relaxed at 375 K for 10 ns. From two perspectives, no obvious crystallization behavior can be seen. However, the molecular dynamics of polyethylene chains with 800 repeat units indicates a single crystalline domain after 10 ns of relaxation at 375 K (see Figure 3-2). The highest order parameter of the crystalline part reaches over 0.7.

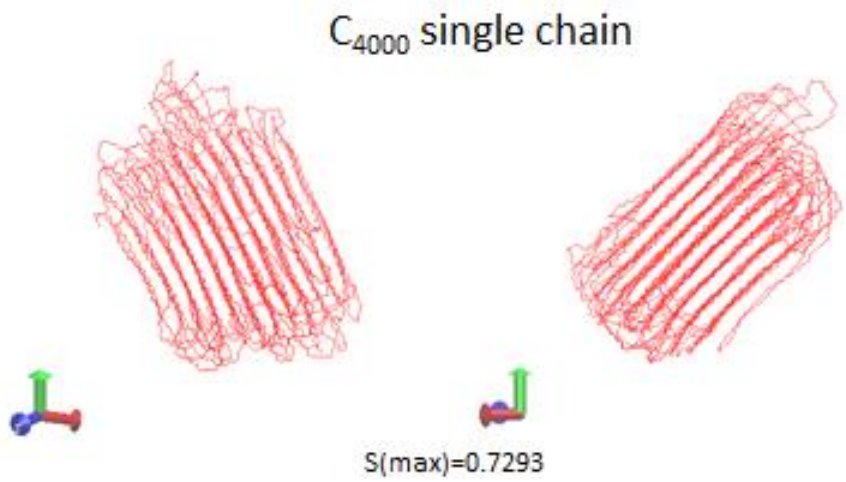

Figure 3-3 A single chain consisting of 4000 repeat units after relaxation at 375 K.

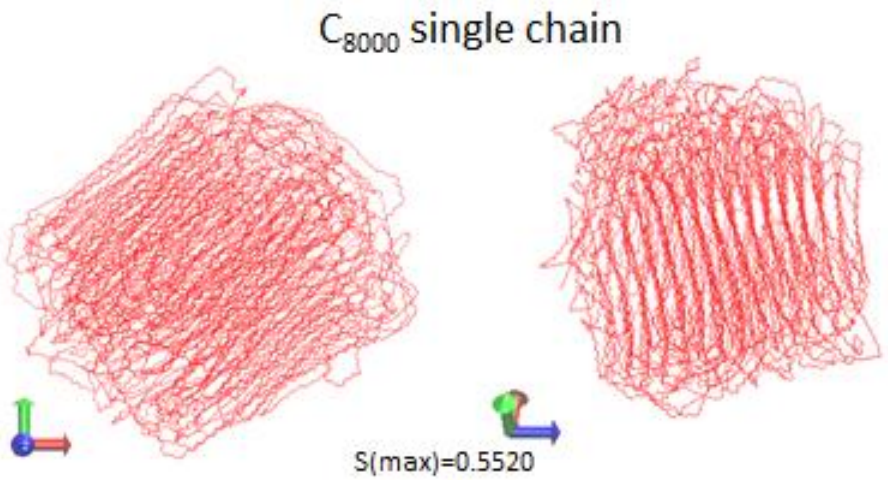

Figure 3-4 A single chain consisting of 8000 repeat units after relaxation at 375 K.

Similar scenarios are also shown in the longer chains of 4000 repeat units (Figure 3-3). A slightly higher order parameter (0.7293) of the entire chain was recorded. This indicates that under suitable thermodynamic conditions and at suitable chain length, a single crystal-like domain could be formed by a single polymeric chain. While the center core are highly oriented and well organized in an all-*trans* conformation, kinks and pendant chains-ends concentrates at the surface of a structure.

However, as the chain length goes further up to 8000 repeat units of a single chain (see Figure 3-4), the overall order parameter dropped to 0.552, and the running time before reaching such a quasi-equilibrium state is significantly longer. Although only one general direction of the chain orientation is observed, due to internal stresses built up inside the crystalline bead, chains are slightly off-axis from one edge to another. In addition, longer chains are more vulnerable for entanglements which will add to defects inside the crystalline domain.

3.3 Basic conclusions and insights into further research

As a benchmark study, the simulations on single chain molecular dynamics show that at long enough chain length and under favorable thermodynamics conditions, a single polymer chain could fold into a monodomain crystalline structure with a highly ordered overall structure with order parameter higher than 0.7. Defects occur in the forms such as entanglements, kinks, loops as well as pendant chain-ends. A relatively long chain (e.g. with 8000 repeat units per chain) takes significantly longer time period to relax. A drop in the overall order parameter to the as-crystallized system is also demonstrated, which could be attributed to more defects from self-entanglements with increased chain length and off-axis orientation of chains in the crystalline domain due to internal stress.

The preliminary research also show potentials in studying crystallization behavior of more complex systems with multiple chains and periodic boundary conditions.

CHAPTER 4

BULK POLYMERIC SYSTEM CRYSTALLIZATION STUDY

In the previous chapter, simulations of single chain dynamics of the chain-folding behavior show a single linear polymeric chain tend to form a monodomain crystallite at proper thermodynamics conditions. Encouraged by the preliminary result, simulations of bulk polymer systems consisting of multiple polymer chains are performed in this chapter. Based on the fact that a polymer chain with a high molecular weight take longer time to disentangle and crystalize, accompanied with a higher tendency to include defects in the crystalline domain, 400 repeat unites are selected here, which meet the minimum chain length to form a crystal.

4. 1 Simulation details of different crystallization conditions

4. 1.1 Crystallization from uniaxial oriented melt

After the isotropic and homogeneous melt is generated, an NVT uniaxial stretching of the melt in the z direction is loaded up to an elongation ratio of 6. The temperature is held at 500 K and the volume is kept at 264 nm^3. The Poisson's ratio is maintained at 0.5, i.e., the x and y dimensions of the simulation box shrink simultaneously with the stretching of the z dimension, to maintain constant total melt volume. A relatively high strain rate of 10^{10} s^{-1} is applied to impose the chain orientation in the melt. The oriented melt is suddenly quenched to 375 K to "freeze" the oriented melt configuration to a non-equilibrium state below melting temperature at atmospheric pressure, which is an optimized condition for crystallization [30]. The system is held at 375 K for 30 ns in the hydrostatic condition to reach a quasi-equilibrium semi-crystalline structure with memories of the orientation at the

initial melting state.

4.1.2 Crystallization from biaxial oriented melt

Similarly, another semi-crystalline structure is created from a biaxial oriented melt, to simulate the stress field of processing conditions such as film formation or compression molding. The initial isotropic melt is stretched two times in the y direction and three times in the z direction, to generate a biaxial oriented melt within 100 picoseconds (ps), the x dimension is compressed into 1/6 of the original length to preserve the constant volume of the melt. The compression ratio is in accordance with that of the uniaxial extension sample. After a transient quench, the biaxial oriented melt is then crystallized at 375 K and atmospheric pressure for 30 ns, with the Nose-Hoover thermostat [84-86] to keep the isothermal-isobaric condition.

4.1.3 Crystallization of amorphous sample with constant stress condition

The structure of a semi-crystalline material is not only determined by the crystallinity and crystal orientation, but also subject to external thermodynamics conditions. The initial structure is a cubic melt cell with a temperature of 425K. Equilibration is performed at the temperature and atmospheric pressure for 2 ns to fully relax the structure and reach an accurate density. The timestep for the relaxation is 2 fs. The melt is suddenly quenched to 375 K while loaded with a constant uniaxial stress in the z direction of 800 MPa. The timestep for constant stress condition is set to 1 fs. The pressure on the x and y directions is coupled and readjusted each 1000 time steps to keep the zero lateral stress condition. The temperature control is performed every 100 fs to keep the constant

temperature at 375 K during the whole crystallization process of 20 ns.

4.1.4 Crystallization of amorphous sample with constant volume condition

In contrast to the constant stress crystallization, a constant volume condition is also imposed for the identical initial structure of a well equilibrated melt. The crystallization temperature is kept at 375 K and the timestep was 1 fs. The simulation box is constantly deformed in the z direction at a strain rate of 1×10^{7} s^{-1}. The x and y dimensions are reduced to maintain a constant volume, assuming the material's Poisson's Ratio is 0.5. The crystallization time is 10 ns, resulting in a total strain in z dimension of 1.

4.2 Analyses of semi-crystalline structures

4.2.1 Crystallization kinetics study of oriented polymeric melts

As is illustrated in Figure 4-1, an initial isotropic polymeric melt is generated and well equilibrated at a temperature of 425 K for 2 ns, before a transient strain of 600 % of its original length in z direction is imposed. The semi-crystalline morphology of the polymeric system in a quasi-equilibrium state is also shown, paired with the density distribution in the z dimension.

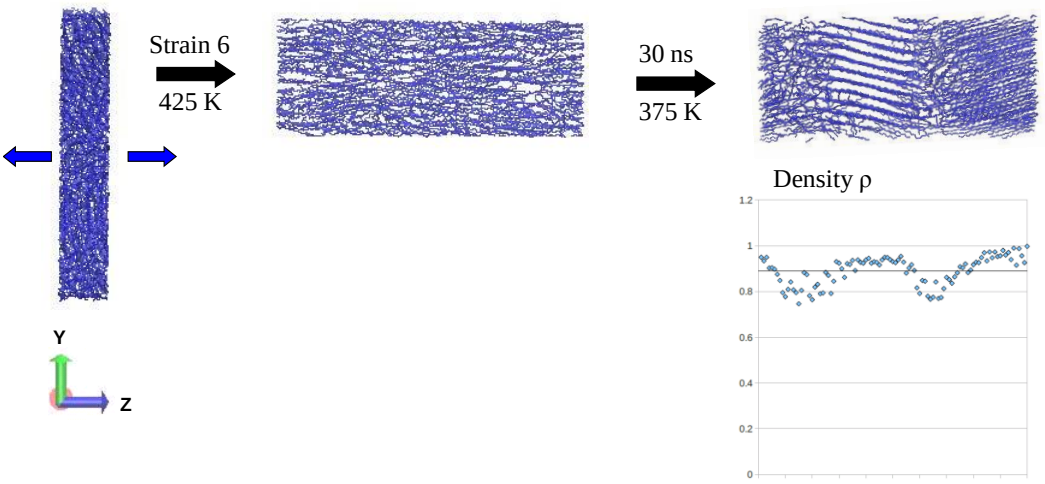

Figure 4-1 Morphological evolution of the orientation and crystallization process.

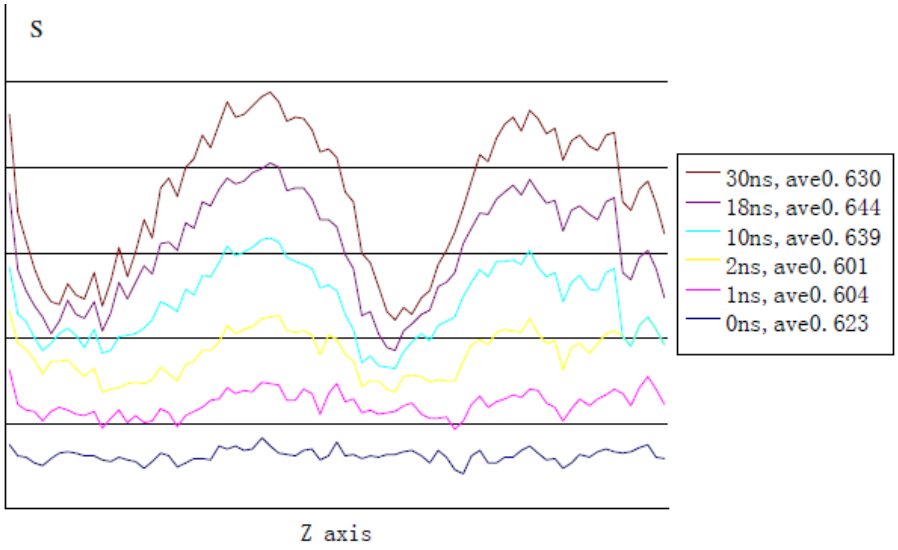

Figure 4-2 Order parameter evolution during the crystallization of an oriented melt.

In Figure 4-2, the crystallization process of the oriented melt is characterized by the change in the order parameter. The initial melt, due to imposed high uniaxial strain, has a relatively high order parameter S=0.6. At the early stage of crystallization (first several nanoseconds), regions with a higher order parameter begin to develop, while the

neighboring regions starts to randomize. From 10 ns to 30 ns, the structure of consecutive ordered-disordered regions is well developed, as is illustrated in Figure 4-2. The highly ordered region corresponds to the crystalline part and the less-ordered region corresponds to the amorphous part.

4.2.2 Characteristics of the semi-crystalline structure from uniaxial oriented melt

A detailed look into the as-crystallized semi-crystalline system (Figure 4-3) reveals more structural characteristics. Based on the order parameter S, the structure could be divided into two crystalline slabs separated by two amorphous slabs. Here the definition of "crystalline" refers to a small region with a Hermans' orientation factor of 0.7 or more. Since the quasi-equilibrium state is reached at a relatively high temperature, thermodynamics will drive the disordered polymer chains to diffuse into a crystalline matrix. Kinks and entanglements may also contribute to the defects inside a crystalline domain. The chain vectors that are not at the *trans*-state and those are not aligned with the stretching direction are counted. The ratios of such defects in the two crystalline slabs are 13.5 % and 9.6 %, respectively. Excluding such defects, recalculations of the Hermans' orientation parameters of the "pure" crystalline chain vectors show that S =0.892 and S=0,873 for the two crystalline domains. The crystalline domains are highly oriented towards the initial uniaxial stretching direction of melt.

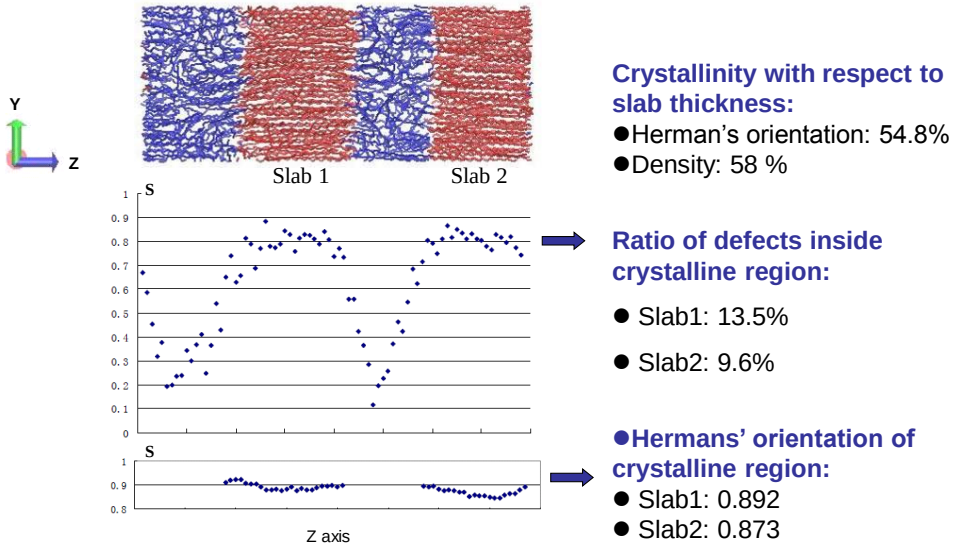

Figure 4-3 Characteristics of the semi-crystalline polymer system crystallized from uniaxial oriented melt.

As is shown in Figure 4-4a, a lamellar semi-crystalline structure is built with periodic repeat units of crystal-amorphous parts.[87] The lamellar structure can be well characterized by the density (see Figure 4-4b) and Hermans' orientation (see Figure 4-4c) distributions along the z axis.

The crystallinity of the sample is 58% with respect to density, and 54.8 % with respect to Hermans' orientation, which provides good convergence and falls within the range of experimental data [88].

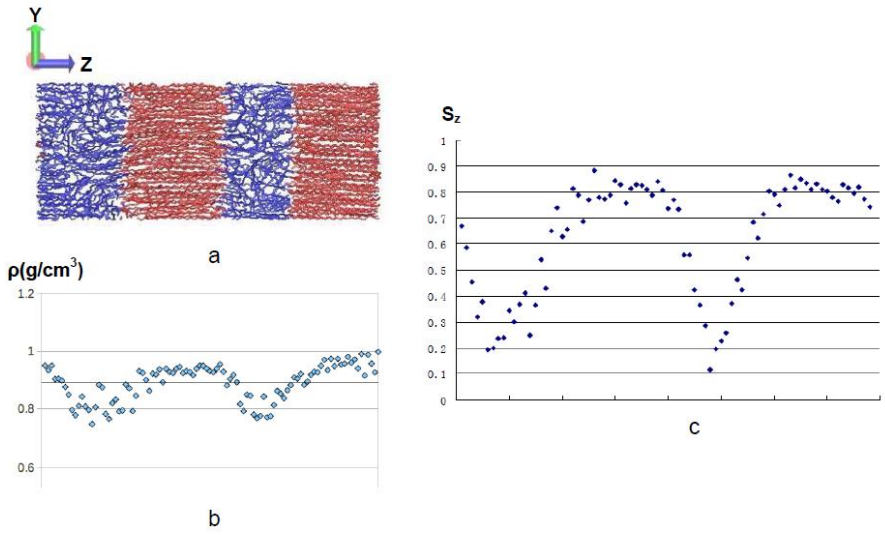

Figure 4-4 Characteristics of the semi-crystalline structure after 30 ns crystallization from unidirectional oriented melt. (a) Snapshot of the semi-crystalline structure on the yz plane, the red colored parts are the ordered crystalline region, with Hermans' orientation with respect to the z axis (S_z) above 0.7. The crystallinity calculated by this method is 54.8%. (b) Density distribution along z axis. (c) Hermans' orientation S_z distribution along z axis.

As is shown in Figure 4-5 (a), the crystalline region show great structural regularity and a predominant orientation towards the original melt orientation. A crystal lattice could be defined. In addition, the pair correlation function (Figure 4-5b) also show great differentiation between the crystalline and amorphous parts. The crystalline region has a much higher peak at around 5 Angstrom than the amorphous region.

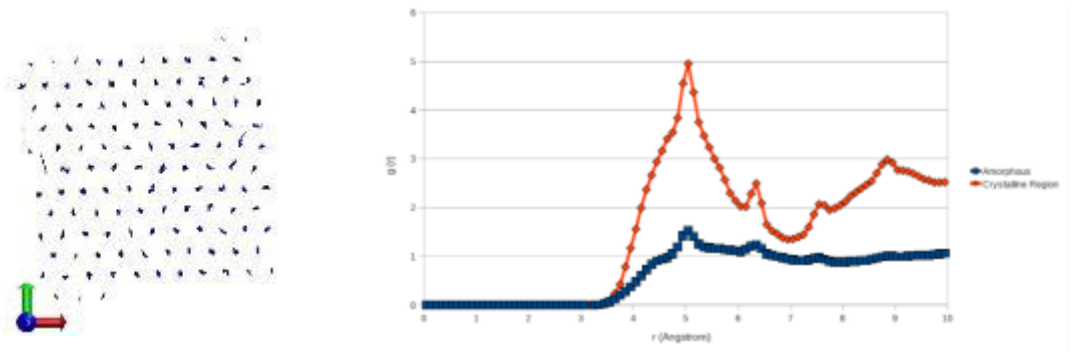

(a) (b)

Figure 4-5 Details of the crystalline structure from highly oriented melt. (a) Snapshot of the crystalline structure on the xy plane (b) Radial distribution function of the crystalline and amorphous regions.

4.2.3 Characteristics of the semi-crystalline structure from biaxial oriented melt

Figure 4-6a shows the semi-crystalline structure crystallized from the biaxial oriented melt. As is drawn from the density differences (see Figure 4-6b), a similar lamellar structure with identical densities of the respective crystalline and amorphous domains was obtained. Another Hermans' orientation S_{ij} was defined to capture the local ordering and different crystal orientations. Rather than a specified direction, each chain vector was calculated once as a reference, and the average Hermans' orientation of a domain was recorded.

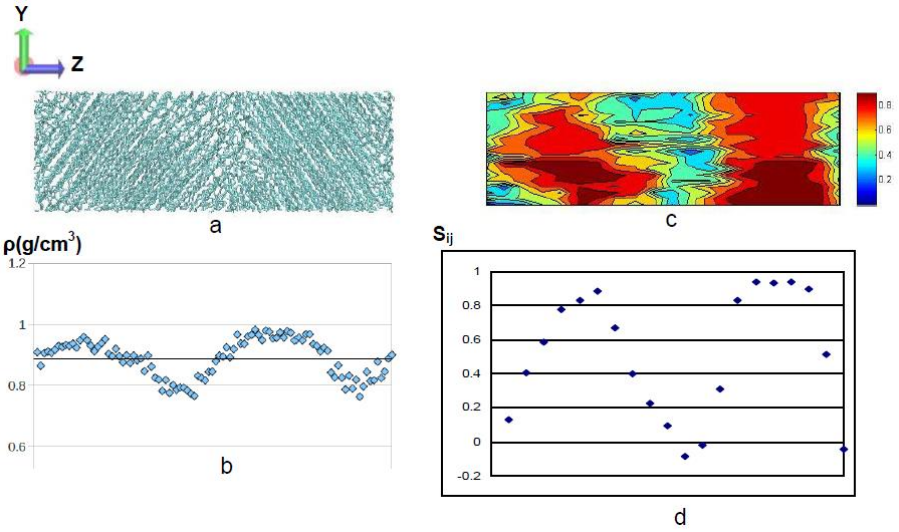

Figure 4-6 Characteristics of the semi-crystalline structure after 30 ns crystallization from bidirectional oriented melt. (a) Snapshot of the semi-crystalline structure on the yz plane. (b) Density distribution along z axis. (c) Self-correlated Hermans' orientation (S_{ij}) distribution on the yz plane. The space was meshed into 20×20 regions, with an average of 20 chains per region. (d) Hermans' orientation S_{ij} distribution along z axis.

4.2.4 Structural characteristics of the semi-crystalline material from constant stress crystallization

After 30 ns of crystallization, the resultant semi-crystalline structure was shown in Figure 4-7a.[89] The semi-crystalline feature of the structure was clearly identified in the density distribution curve, in which the densely packed region (highly ordered) with a density approaching 1, while the less ordered region with density minima at around 0.8. The typical lamellar structure of the crystalline part was also shown from the periodic density fluctuations (see Figure 4-7c).

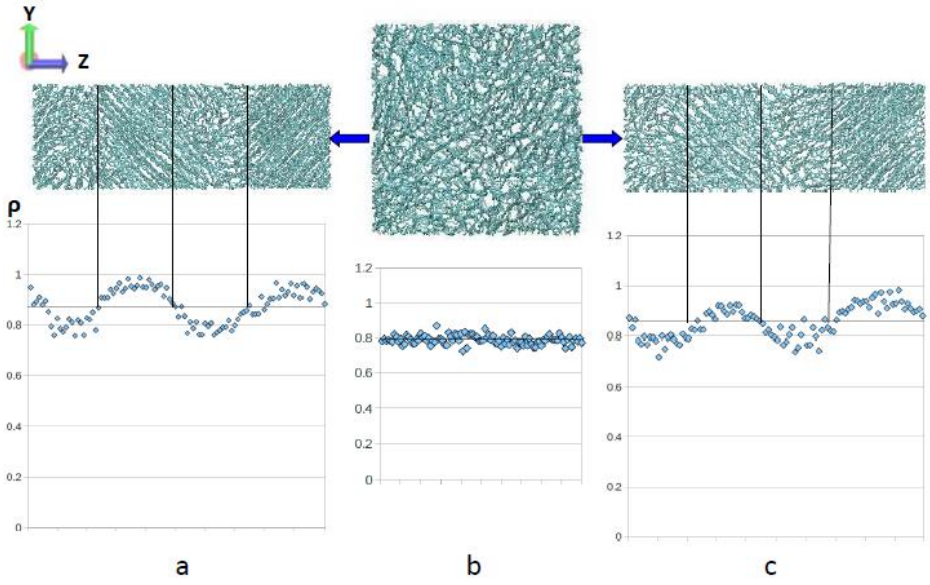

Figure 4-7 Morphologies and density distributions of the semi-crystalline structures prepared through (a) constant stress deformation and (c) constant volume deformation from (b) the initial structure.

4.2.5 Structural characteristics of the semi-crystalline material from constant volume crystallization

The bulk crystallization structure from the constant volume under constant strain rate crystallization to a strain of 1 was shown in Figure 4-7c. From the density distribution, well defined crystal and amorphous lamellae were identified, confirming the direct observation from the morphology. The crystal density of approximately 1 and the amorphous part density minima of around 0.8 were consistent with experimental results [88] and similar to the MD simulated structures from previous constant stress conditions.

4.3 Conclusions

Semi-crystalline structures can be prepared through different processing conditions. By tuning the initial structure and the isothermal crystallization environment, samples from pre-oriented melt, under constant stress or constant volume conditions can obtain lamellar structures with similar crystallinity, crystal orientation, lamellae thicknesses and density distribution.

CHAPTER 5

MECHANICAL PROPERTY OF SEMI-CRYSTALLINE STRUCTURES

Uniaxial deformation behavior and corresponding stress responses are calculated of bulk polymeric systems under different processing conditions. The major objective of this research is to establish a relationship between the morphological evolution of a semi-crystalline structure and its mechanical behavior.

5.1 Uniaxial deformation simulation

Uniaxial tensile simulations are carried out along the z direction on the semi-crystalline structures. The z dimension is continuously deformed to a strain of 1 over 10 million timesteps, each 1 fs, corresponding to a strain rate of 1.24 nm/ns. All references to "strain" in this paper refer to engineering strain. The x and y dimensions are reduced to maintain a constant volume, assuming the Poisson's Ratio of 0.5. The temperature is held at 375 K.

Another deformation simulation is carried out on the biaxial-oriented semi-crystalline structure, in which the lateral stresses (in the x and y directions) are maintained at zero while the strain in the z direction is applied to the end of the periodic box at a constant engineering strain rate of 1.24nm/ns. The periodic box size is free to expand or contract in the x and y dimensions. Deformation increments are applied at each timestep in the z direction, while the pressure (stress) controls in the x and y directions are performed every 1000 timesteps to maintain lateral normal stress free conditions. This is equivalent to an $NL_z\sigma_x\sigma_yT$ ensemble, compared to the NVT ensemble employed in the previous

deformation simulations. Here L_z refers to the periodic box length in z direction, which increases in a fixed rate with time, while σ_x and σ_y represents the external pressure on the x and y directions, which are readjusted to zero every thousand time steps. The constant pressure condition is widely believed to be more closely representative of deformation experiments, and has been applied previously in deformation simulations of amorphous polyethylene samples [34].

5.2 Morphological characteristics and tensile behavior of uniaxially deformed semi-crystalline systems

5.2.1 Morphological changes during tensile deformation of the unidirectional oriented semi-crystalline structure

The crystalline domain of the initial structure, due to the pre-orientation from the melt, exhibits an average Hermans' orientation of 0.8 with respect to the z direction, which means the chains are only slightly off-axis. As deformation initiates, the rotation of the polymer chains inside the crystalline part dominate the elastic region of the stress-strain behavior, shown in Figure 5-1a.

Once the crystal rotational deformation is exhausted, as the Hermans' orientation of the crystalline domain approaches 1 in the z direction, the stress-strain curve enters the inelastic region (see Figure 5-1b~e). In the amorphous domain, S_z increases steadily with stretching. The drop in the density near the center of amorphous domains is an indication of orientation of chains and their incorporation into the crystals, which occurs mostly in the interfacial area. However, after the strain reaches 0.5 (see Figure 5-1e), the density of the amorphous domains also increases, which is possibly attributed to the homogenization of the entire structure, while lamellar characteristics still remain.

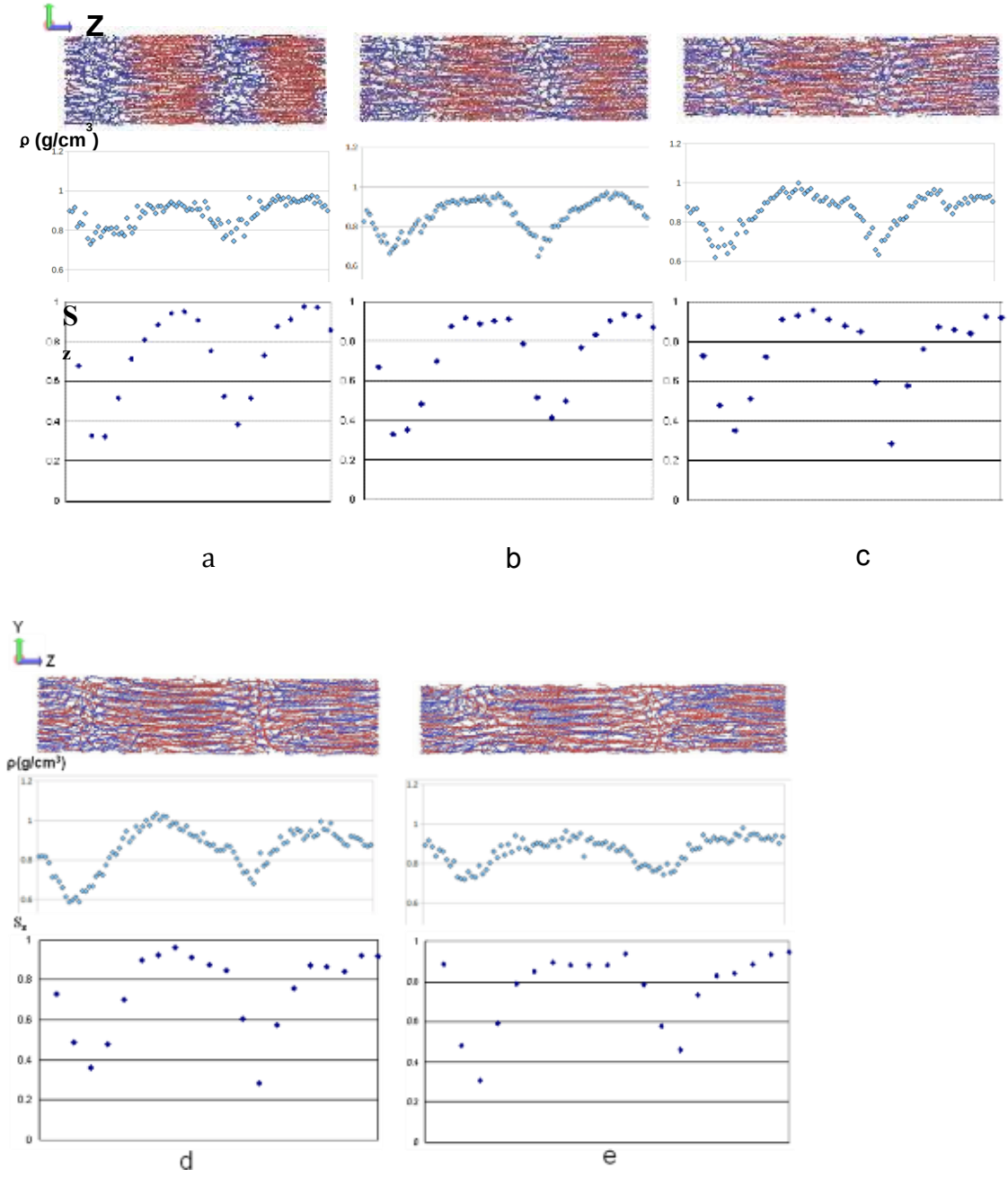

Figure 5-1 Morphological changes during uniaxial stretching along z axis of unidirectional oriented semi-crystalline structure consisting two crystalline domains in a periodic simulation box, (a)-(e) corresponds to the strain of 0.1-0.5.

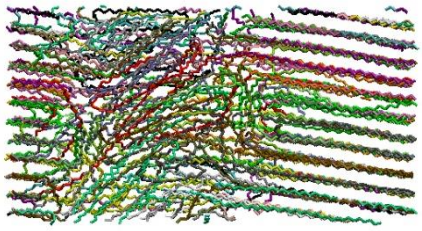

a 0.1

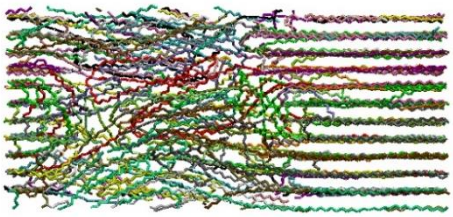

b 0.2

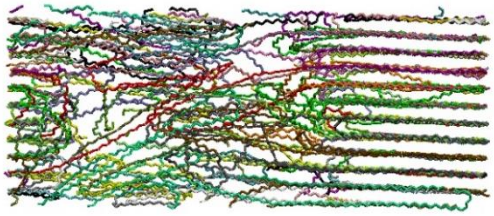

c 0.3

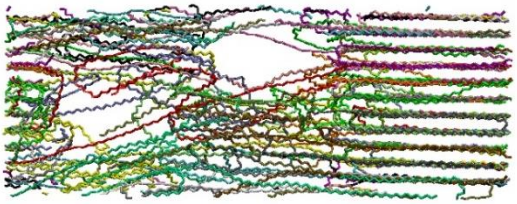

d 0.4

Figure 5-2 Morphological changes during uniaxial stretching along z axis of a unidirectional oriented semi-crystalline structure consisting one crystalline domain in a periodic simulation box, (a)-(d) corresponds to the strain of 0.1-0.4.

A semi-crystalline structure with shorter box length in the pre-orientation direction is also built to explore the finite-size effect on morphological evolution during the unidirectional deformation simulation.

For the structure shown in Figure 5-2, the crystallization protocol is identical to the structure in Figure 5-1. Clearly an oriented semi-crystalline structure is presented. The only difference is that only one crystalline domain and one amorphous domain are presented in one simulation box, due to the shorter periodic box length. However, the morphology is less stable even at a small strain level, featuring void growth in the early stage of deformation. This could be attributed to an artifact of the limited simulation box size. However, for the structure presented in Figure 5-1, the effect is not obvious. This box size is thus selected for future mechanical property predictions.

5.2.2 Morphological changes during uniaxial deformation of the bidirectional oriented semi-crystalline structure

During the deformation simulation, the rotational motion of chains in the crystalline domains persists to a higher strain, until fully orients along the z axis. Despite the continuous rotation of the crystals with deformation, the overall lamellar semi-crystalline structure is maintained during deformation up to a strain of 0.5[87] (see Figure 5-2a~e).

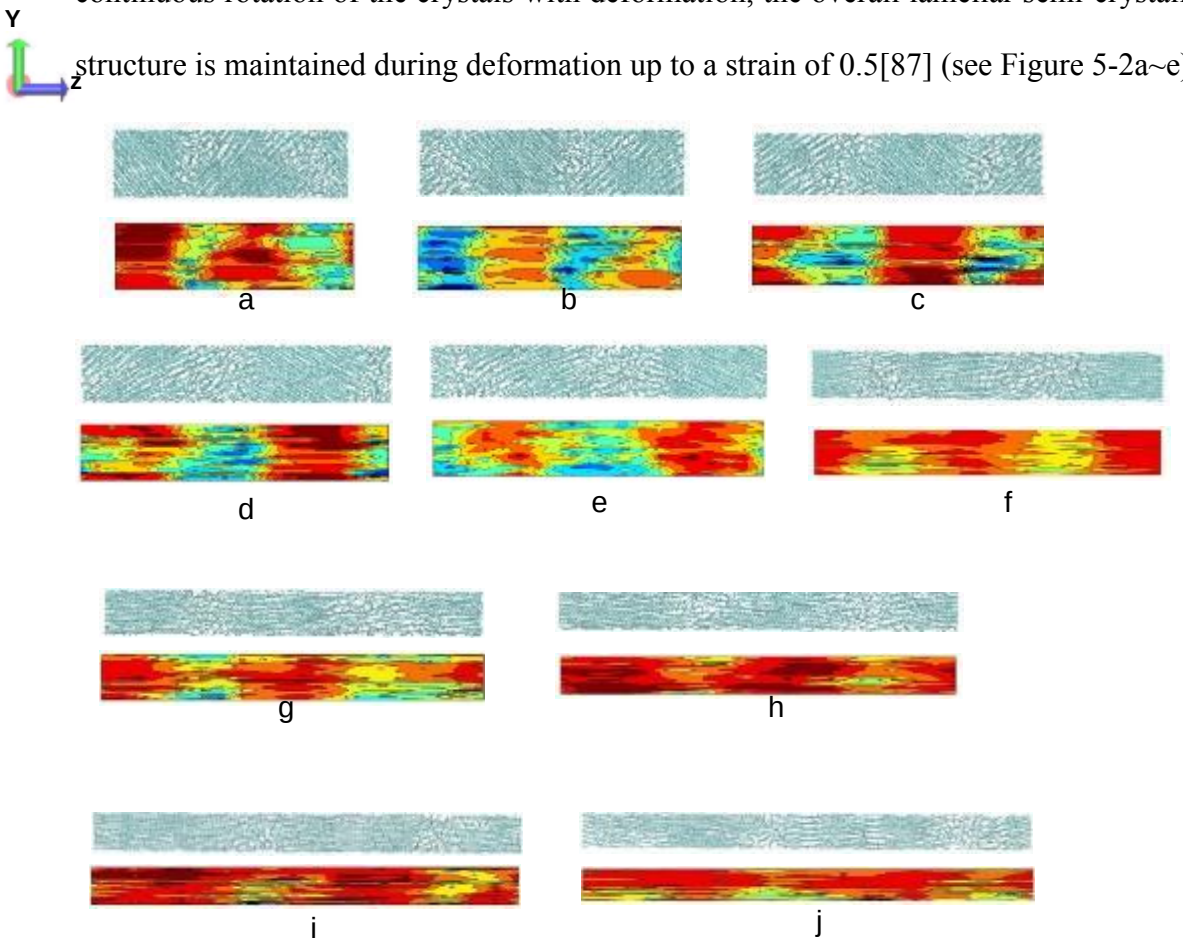

Figure 5-3 Morphological changes during uniaxial stretching along z dimension of the bidirectional oriented semi-crystalline structure, (a-j) corresponds to the true strain of 0.1-1.0.

Nevertheless, after a strain of 0.6 (see Figure 5-3f), some regions in the previously amorphous domain become locally ordered and connect two adjacent crystals. The growing trend of crystalline inter-connections evolve into a new structure which features highly oriented and fully stretched chains along the z axis, surrounded by amorphous regions, as shown in Figure 5-3g~j.

5.2.3 Tensile behavior of the semi-crystalline structures

Based on the above analysis of the crystal size, orientation and crystallinity, no significant differences were found among the three structures with different processing conditions. However, further examinations of the stress-strain behavior of the structures showed large divergences, as is shown in Figure 5-4.

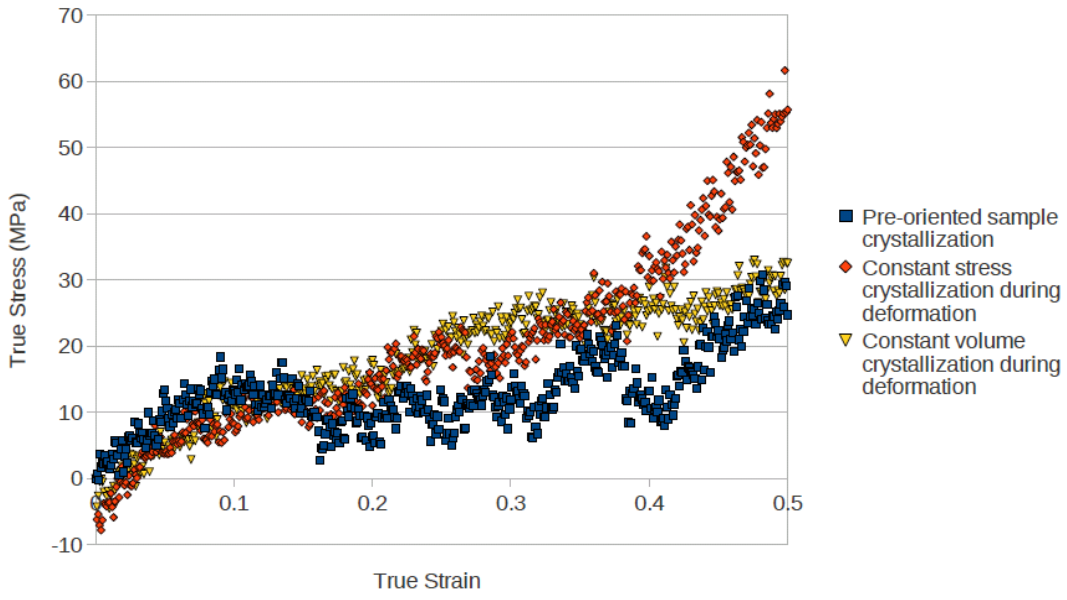

Figure 5-4 Tensile stress-strain relations of the semi-crystalline structures prepared from the biaxial pre-oriented melt (cubes), under constant stress condition (diamonds) and under constant volume, constant strain rate condition (triangles).

Figure 5-4 compares the true stress-strain behavior of the semi-crystalline structures at 375 K, up to a strain of 0.6. [89] The squares show the structure crystallized from uniaxial oriented melt, while the diamonds represent the structure from the biaxial oriented melt. In the initial elastic region, the unidirectional semi-crystals exhibit a higher modulus, due to the better general alignment of the crystal chains. Double yield points are observed for both curves at a strain around 0.1, which coincides with the experimental findings from the true stress-strain curves, which are identified at strain levels of 0.07 and 0.11 [17]. In the subsequent inelastic region, strain hardening behavior is observed for both samples, but the bidirectional oriented semi-crystalline structure demonstrated a more obvious hardening trend, which is possibly due to the competition of network stretching and crystal reorientation and growth during deformation. The fluctuations of the stress-strain curve are still large, especially at higher strains, even after averaging over 15 independent runs. This might be due to the limited size of the periodic simulation box and high strain rate, which is a general limitation of the MD simulations.

During the uniaxial extension of the bidirectional oriented semi-crystalline structure with zero lateral stress (see Figure 5-5), the initial behavior is similar to that of constant volume deformation. An initial linear stress response is observed up to a strain of 0.07. However, the stress-strain curve diverges significantly after the strain exceeds 0.1, even after averaging over 20 independent runs of the deformation simulation. One possible reason for this is cavitation inside the sample. The limited size of the simulation cell and application of periodic condition could also generate unphysical artifacts in the stress simulation at large deformation. Most of the deformation occurs in the amorphous region.

As the strain increases, the density in the amorphous region drops more rapidly. The trend of deformation inhomogeneity initiates vacancy evolution and growth of free volume in the amorphous domain, which has also been reported in experiments [90]. In Figure 5-5, vacancies are visible at a strain of 0.2.

The common features include the initial elastic part, followed by the yielding point between strain 0.05 and 0.1. But in the subsequent plastic region, different behaviors were displayed, indicating their thermo-mechanical history during crystallization. Strain hardening behavior, which was attributed to the network stretching in the amorphous part of polymeric structures, was observed only for the samples crystallized during constant stress conditions, either from the pre-oriented melt or during constant stress deformation. The structure from constant volume deformation saw a continuous drop in modulus after yielding. A major difference between the NPT and NVT conditions is that the former allows volumetric changes during constant temperature crystallization while the latter keeps the total volume of the system despite of the shape change of the simulation box. As is well known, the density of crystalline polymers is higher than their amorphous counter parts at the same temperature, due to spatial regularity in chain arrangement. Consequently, as part of a polymer system crystallizes, the density of the entire structure will increase. The NPT conditions, by keeping constant stress on the boundaries, led system shrinkage, which was forbidden in the NVT condition. The constant volume restriction on the partially densified semi-crystalline structure gave rise to a less effective network in the inter-crystal amorphous region. In contrast, the network was better developed under constant stress conditions, preserving a normal density after relaxation.

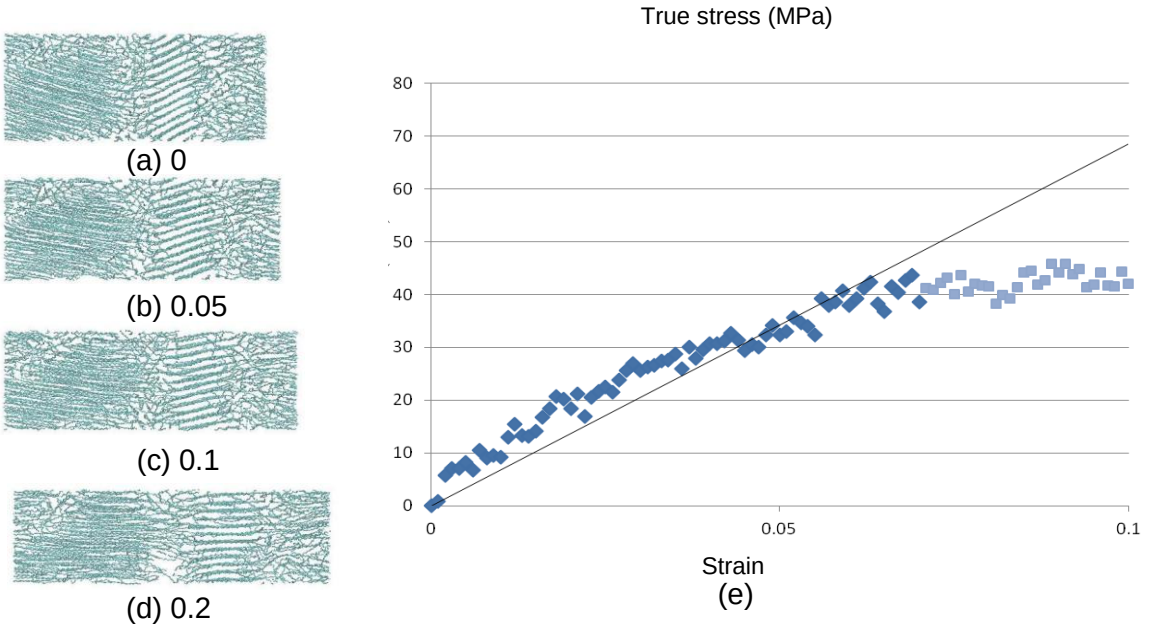

Figure 5-5 Morphological changes and stress-strain behavior of the initial part of the uniaxial stretching simulation along z axis on polyethylene samples with zero lateral stress condition, with strain (a) 0, (b) 0.05, (c) 0.1, (d) 0.02, (e) calculated true stress-strain curve upto 0.1 strain.

5.3 Conclusions

The elastic behavior of the bulk polymer samples depends largely on the molecular architecture, including the degree of crystallinity and the crystallite orientation distribution. The highest yield stress is achieved by semi-crystalline structures with chains in the crystal domains that are predominantly oriented with the tensile direction. For the bidirectional oriented semi-crystalline structure, an enlarged region of strain hardening behavior is observed due to the rotation of crystals towards the tensile straining direction.

During the deformation simulations, morphologically, the crystalline parts of the samples have similar behavior, which features the continuous rotation of the crystals with their chain orientations towards the tensile direction. Apart from the crystalline contribution, the effectiveness of the inter-crystal network also plays an important part in the mechanical performance.

The laminar to fibrillar transition during deformation, which was supported by evidence from *in-situ* X-ray diffraction pattern [12, 21], is also detected from the Hermans' orientation spectra at the molecular level. The lamellar structure is maintained up to a train level of 0.5, followed by a transition to the fibrillar structure with long periods of highly ordered fibrils in the tensile direction, surrounded by amorphous interlayers.

CHAPTER 6

TWO-POINT STATISTICS ANALYSIS OF SEMI-CRYSTALLINE STRUCTURES

During the previous bulk polymer crystallization and deformation simulations, local density and Hermans' orientation distributions are used as efficient tools in structural quantification of the semi-crystalline structure and their morphological evolutions. In this chapter, two-point statistics is introduced for a better description of the semi-crystallinity.

6.1 Characteristics of the semi-crystalline structure from biaxial oriented melt

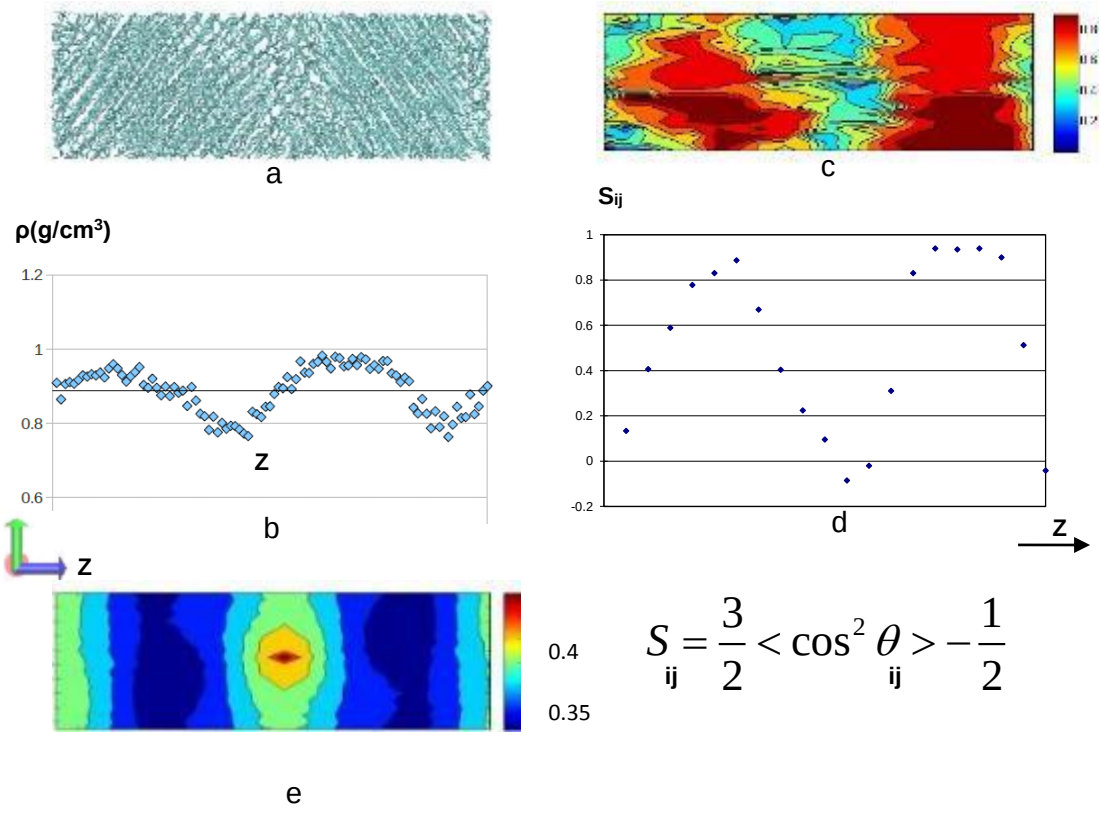

$$S_{ij} = \frac{3}{2} < \cos^2 \theta_{ij} > - \frac{1}{2}$$

Figure 6-1 (a) Snapshot of the semi-crystalline structure on the yz plane. (b) Density distribution along z axis. (c) Hermans' orientation S_{ij} distribution on the yz plane. (d) Hermans' orientation S_{ij} distribution along z axis. (e) 2D two-point autocorrelation.

In time-resolved SAXS experiments [91] on semi-crystalline polyethylene samples, autocorrelation functions of diffraction intensity were applied to analyze the lamellar polyethylene crystals, utilizing the 1D autocorrelation intensity changes with distance.

However, as a robust mathematical tool, simulations results could also be analyzed by two-point statistics. First of all, two-point autocorrelation of the semi-crystalline structure from bidirectional oriented melt (see Figure 6-1a) is calculated. The Hermans' orientation factor (see Figure 6-1c and d) is used as microstructural function. From the two-point autocorrelation mapped on the yz plane (see Figure 6-1e), the banded spectrum along z axis reflects the lamellar morphology of the sample, in which crystalline lamellae repeats at certain distance, while in the lateral y direction, no such correlations are found.

6.2 Characteristics of semi-crystalline structures during deformation

As is shown in selected two-point correlation spectra during deformation (see Figure 6-2), the banded pattern remains clear at the early stage of deformation, which indicates the maintained lamellar characteristics of the structure. In combination with the observation of the chain morphology, the deformation is attributed to the rotation of the crystalline lamellae which direct the chain vector to the uniaxial tensile direction in the early stage. In addition, the amorphous part consists of entangled networks becomes taut due to stretch.

At a moderate strain, some streaks develop along the z axis, with a blurred boundary between the bands, which could be interpreted as the break-up of the original crystalline lamellae followed by lateral correlation developed between the crystallites.

Since the crystalline chain directors are pointed to the stretching direction, shearing between the chains will lead to the lateral displacement inside the crystals, resulting in the destruction of the former crystal lamellae and generation of laterally correlated new crystallites.

At a large strain of 0.9 (Fig. 6-2c), from both of the autocorrelation of crystallites and cross-correlation between the crystalline and amorphous phases, bands are broken by multiple parallel streaks, which clearly indicates the lateral periodicity. This is a further proof of the lamellar-to-fibrillar transition.

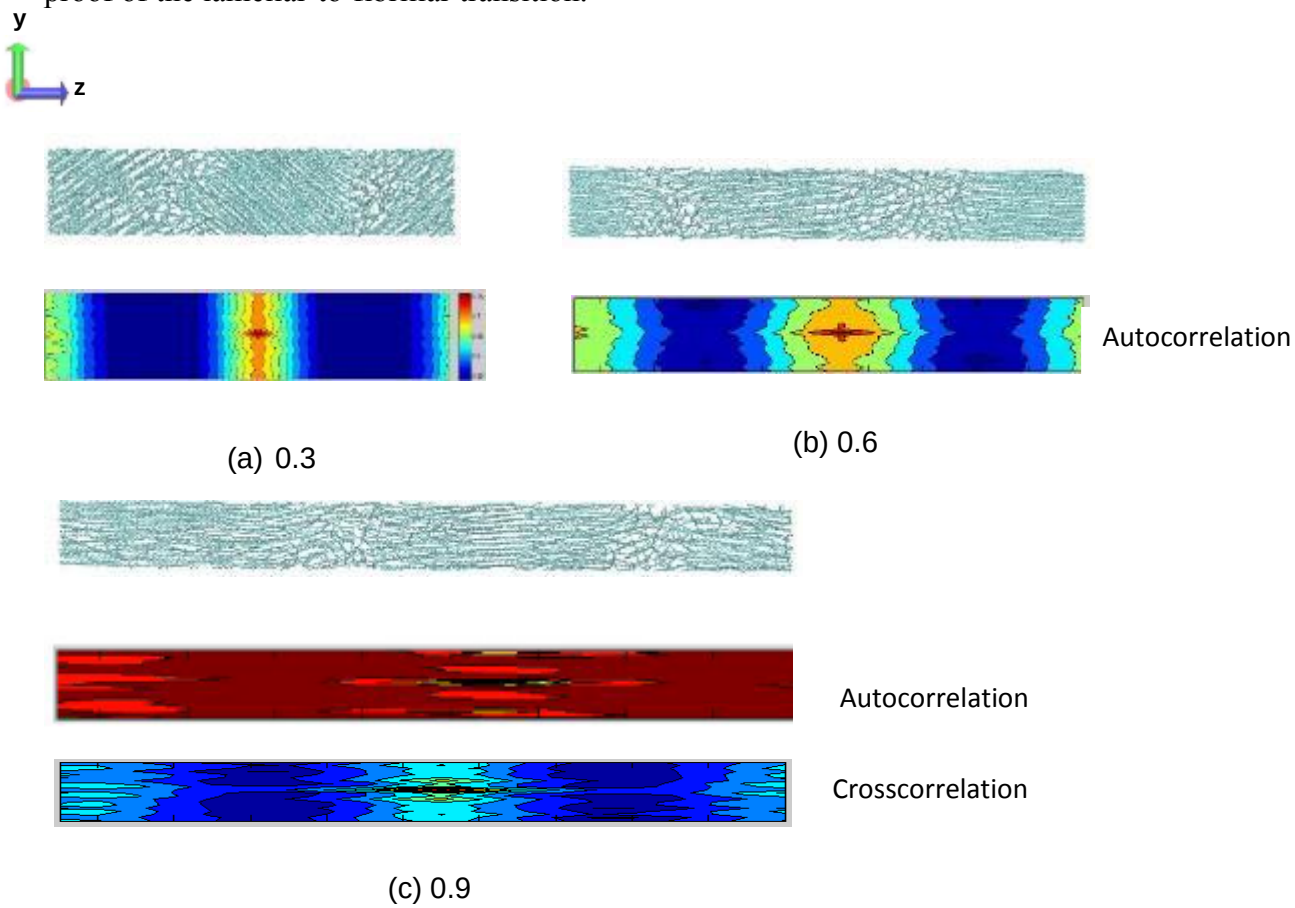

Figure 6-2 Morphological changes and selected two point statistics during uniaxial tensile deformation along z axis of bidirectional oriented semi-crystalline structure; strain: (a) 0.3; (b) 0.6; (c) 0.9.

6.3 Three-dimensional representation of two-point statistics

As is well presented above, the application of two-dimensional (2D) two-point statistics in the structural characterizations would facilitate the interpretation of morphological features of a semi-crystalline polymeric system and tracing its evolution under extension. The method of image convolution eliminates artificial effects brought by the finite size of a simulation box, enhances the resolution of the contrasts between phases and sharpens the boundary between the crystalline part and amorphous part. However, the 2D image is still an averaged representation of a three-dimensional (3D) object. Due to the 3D anisotropic nature of a semi-crystalline polymer system, some features are lost in the averaging process. To make full illustration of a semi-crystalline structure on the Angstrom resolution, both surface view and representative slice view of a semi-crystalline structure are demonstrated by the 3D two-point autocorrelation, as is shown in Figure 6-3.

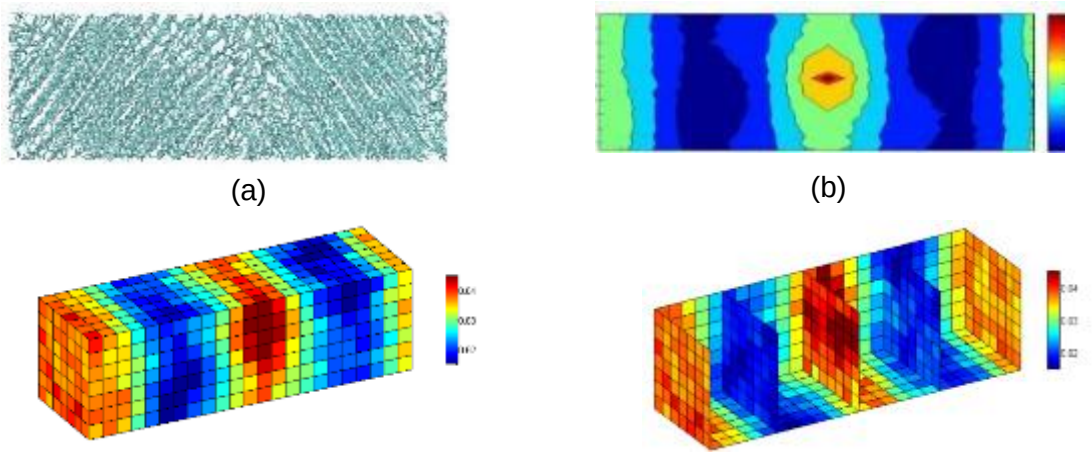

Figure 6-3 (a) Snapshot of the semi-crystalline structure on the yz plane; (b) 2D two-point autocorrelation; (c) surface view of 3D two-point autocorrelation; (d) slice view of 3D two-point autocorrelation.

In Figure 6-3 (c), the surface of a simulation box shows distinctive laminar features, with consecutive higher ordered and less ordered regions, corresponding to the crystalline and amorphous parts of a semi-crystalline structure. Slices of the structure (see Figure 6-3 d) also show great differences between the amorphous and crystalline regions. Comparatively, the fluctuation at different locations within a certain region is small.

6.4 Conclusions and outlook

2D Two point statistics method is proven to be an effective tool in structural characterization of the semi-crystalline structure and their evolution during deformation. The microstructural function is defined as the local Hermans' orientation factor. Owing to the great difference between the amorphous and crystalline regions, the structure was well represented. The 3D two-point statistics method further supports the laminar nature of a semi-crystalline polymer system.

The successful use of the two-point statistics methodology of describing order/orientation inside a polymeric system could find wider applications in other morphological changes of semi-crystalline systems during annealing/recovery and partially ordered systems such as liquid crystalline polymers.

CHAPTER 7

RECOVERY AFTER DEFORMATION

In Chapter 5, simulations on morphological evolutions during deformation of semi-crystalline structures are performed. Snapshots of the structure instantly at certain strain levels during the deformation process are analyzed. However, the strain rate during MD simulations (~ 10^7 s^{-1}) is much higher than the experimental setup, which casts clouds on the validity of the detected morphology. Questions could be raised that whether it well represents the real-world morphology or it is just a transient fact that could relax to another state in experimental time scale.

Considering the computational resource cost of simulations of deformation, it is barely possible to substantially lower the strain rate a comparable level of experiments (10^4 ~ 10^5 s^{-1}) for "ultra-fast" deformation. To partially address the time-scale difference between current MD simulations and existing experimental setup, recovery simulations of selected representative stages of the deformation process is performed in a time-scale to reach a quasi-equilibrium state. The structural evolutions during such relaxation processes are analysis and compared to validate the stability of certain structural characteristics. In addition to density and Hermans' orientation distributions, the two-point statistics tool described in Chapter 6 are also applied in the analysis of the relaxed structure, be better trace the morphologies.

7.1 Recovery after deformation simulations

Recovery relaxation is performed for 10 ns at 375 K after deformation is applied. The selected initial strain levels are 0.3, 0.6 and 0.9, respectively. Since the main goal of

the recovery process is to observe the morphological changes of the semi-crystalline structure and to verify the stability of the phase transition during deformation, the strain in the stretching direction is fixed, while the other dimensions are suddenly exposed to atmospheric pressure immediately after deformation, to allow volumetric and structural relaxations at different stages of deformation. The use of the $NL_z\sigma_x\sigma_yT$ resembles the experimental condition of the annealing/recovery process and is able to capture the configuration changes at the MD scale.

7.2 Analyses of recovery after deformation

The self-correlated Hermans' orientation S_{ij} mapped on the yz plane before and after the recovery simulations are shown in Figure 7-1, paired with the two-point statistics based on the Hermans' orientation factor.

At a strain of 0.3 (see Figure 7-1a), the lamellar structure is maintained with more distinct interfaces after relaxation, due to the effect of annealing.

At a strain of 0.6 (see Figure 7-1b), although the crystals obtains higher chain alignment, local ordering in the previous amorphous region is not completely diminished after relaxation. Microfibrils begin to initiate by connecting multiple crystals.

At a higher strain of 0.9 (see Figure 7-1c), after chain relaxation and defect migration, a fibrillar structure of long periods of fully stretched chains is stabilized, surrounded by the less ordered region. This fibrillar formation in the stretching direction is also reflected by the two-point correlations, which feature better defined longitudinal streaks after recovery (see Figure 7-1c), in comparison to the original banded spectrum in the early stage of deformation, e.g., at a strain level of 0.3 (see Figure 7-1a).

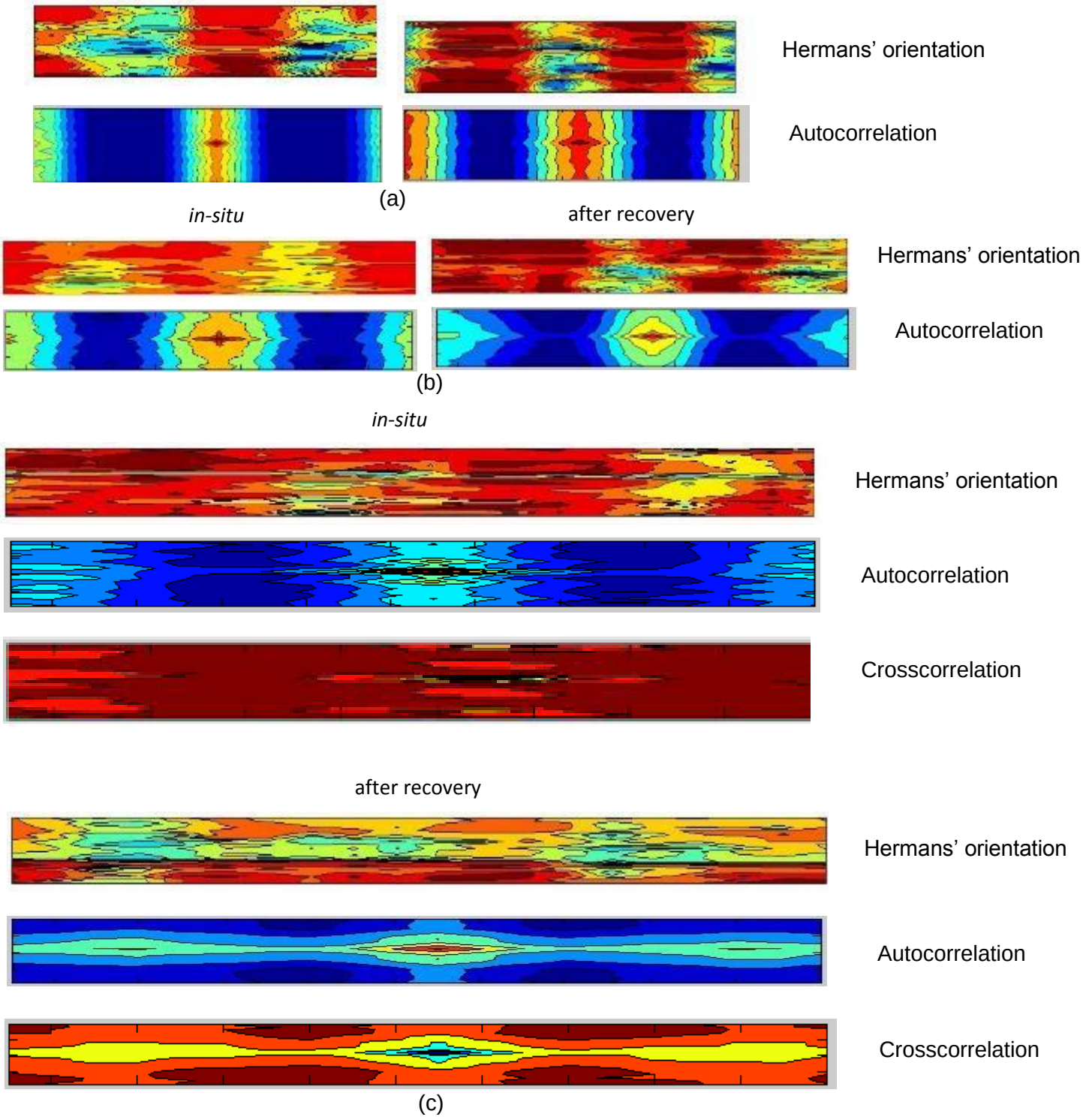

Figure 7-1 Morphological changes reflected by Hermans' orientation, and two-point statistics before and after 10 ns of NPT relaxation at 375 K; strain: (a) 0.3, (b) 0.6, (c) 0.9.

To further examine the structural character of the lamellar-to-fibrillar transition, S_{ij} is also mapped along the uniaxial deformation direction z. At a strain of 0.3 (see Figure 7-2), a typical lamellar structure is evident, with highly ordered crystals with S_{ij} approaching 0.9. The local minima between 0.4 and 0.5 are characteristic of the inter-lamellar amorphous region, with certain preferred orientation due to stretching. At a strain of 0.6, the maximum remains, while the minimum rises to around 5.5. Combined with the two-dimensional scheme, part of the inter-lamellar region becomes highly ordered, rather than a homogeneous stretching of the network. The growing trend of the local ordering is also indicated at a strain of 0.9, where a pronounced drop in the maxima reduces the local differences along z axis. It is speculated that this is due to the destruction of lamellae and formation of the fibrils along z axis, which are surrounded by less ordered regions. The recovery simulation provides further confirmation of the lamellar-to-fibrillar transition. The transition is stable with the maintained strain levels.

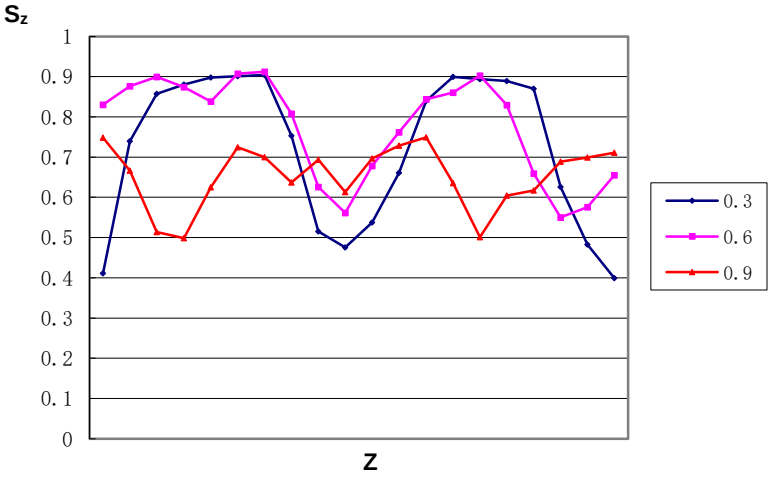

Figure 7-2 Hermans' orientation mapped along the z axis, at strain levels 0.3, 0.6 and 0.9.

7.3 Conclusions

The recovery simulations of semi-crystalline structures after their deformation show further purification of both the crystalline part and the amorphous part. The crystalline part become better organized and the amorphous part become less oriented with added randomness. The well relaxed crystalline region and amorphous region have a more distinct interface.

Hermans' orientation and two-point statistics analysis of the recovery of the as-deformed structures at both the lamellar stage and fibrillar stage confirms that the fibrillar structure introduced by large-scale deformation is stable after relaxation.

CHAPTER 8

CRYSTALLIZATION OF THIN FILMS

After the detailed investigation of the crystallization, deformation and recovery properties of bulk semi-crystalline polymers, exploration of the effects on the crystallization of polymers with free surfaces is also made. Instead of three dimensional periodic boundary conditions applied to the bulk system, in the thin film structure only the x and y dimensions obtain periodicity, while free surfaces in the z dimension are exposed to vacuum or certain substrates. The structure resembles a polymer thin film.

Biaxial extension is a widely applied technology for thermoplastic film forming, commonly known as blow filming. By varying the applied biaxial stress, not only the film thickness is changed, but also the chain orientation is affected. The anisotropic properties of biaxial stretched films are investigated with chain and crystallite orientation.

In addition to free-standing thin films, polymeric thin films with a substrate also attracted research and application interests such as functional membranes, packaging and coating materials. Typical film making technologies of polymers such as cast filming and spray coating introduce minimal or no stress to the polymeric system. Simulations here concentrate on the crystallization of such films deposited on a strongly interacting substrate with no other applied stress so that the influence of substrate on the polymer crystallization/orientation morphology could be exclusively studied.

8.1 Crystallization of free surface

8.1.1 Crystallization of a free standing thin film with moderate biaxial stress

A fully relaxed free standing film with periodicity only at the x and y dimensions

(red and green arrows) at 425 K is shown in Figure 8-1a. The $NL_z\sigma_x\sigma_yT$ ensemble is applied for both the high temperature equilibration and subsequent crystallization process with Nose-Hoover thermostat [84-86]. Employing a temperature of 375 K, the free standing thin film is crystallized under moderate biaxial stresses of 100 MPa in both x and y directions.

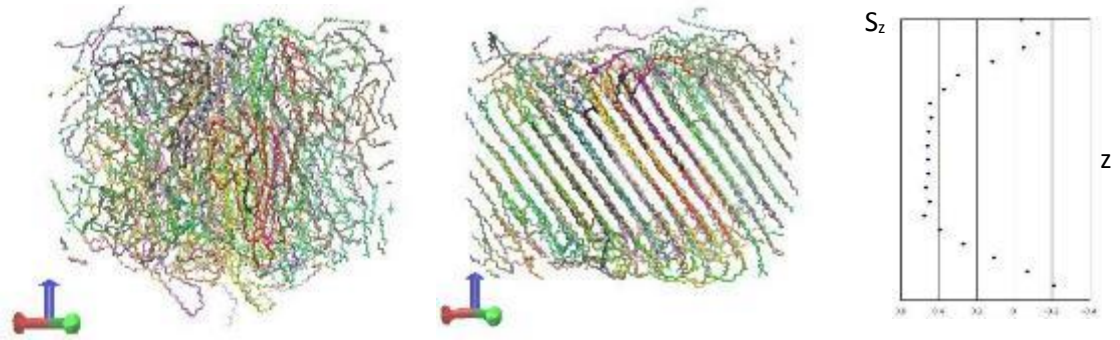

(a) (b) (c)

Figure 8-1 (a) Initial structure of a free standing thin film at 425 K. (b) Semi-crystalline structure after 20 ns crystallization of free-standing thin films at 375 K with biaxial stress of 100 MPa. (c) Hermans' orientation S_z distribution in film thickness direction z.

The final structure after 20 ns crystallization in Figure 8-1b shows clearly a semi-crystalline feature, which is also demonstrated in the Hermans' orientation distribution in Figure 8-1 c. The chains near the free surface area has higher mobility compared to the chains at the central "bulk like" regions. Due to less confinement, the free surfaces remained amorphous, while the chains in the central region are able to crystallize with uniform orientation. Consequently, the Hermans' orientation of the free surfaces is close to 0, while the one in the center is approximately 0.5. The Hermans' orientation factor of the surface region is slightly negative, which indicates a preferred side-on morphology of

loops and chain ends at the surface. However, no obvious ordered surface feature is detected.

8.1.2 Crystallization of a free standing thin film with strong biaxial stress

Inspired by the case of a free standing thin film crystallized under moderate biaxial stress, the situation with a strong biaxial stress is studied. With the same crystallization temperature at 375 K and identical initial structure of two-dimensioanl periodic boundary conditions, the structure is evolved for 20 ns with constant biaxial stress of 150 MPa (compared to 100 MPa at the previous simulation).

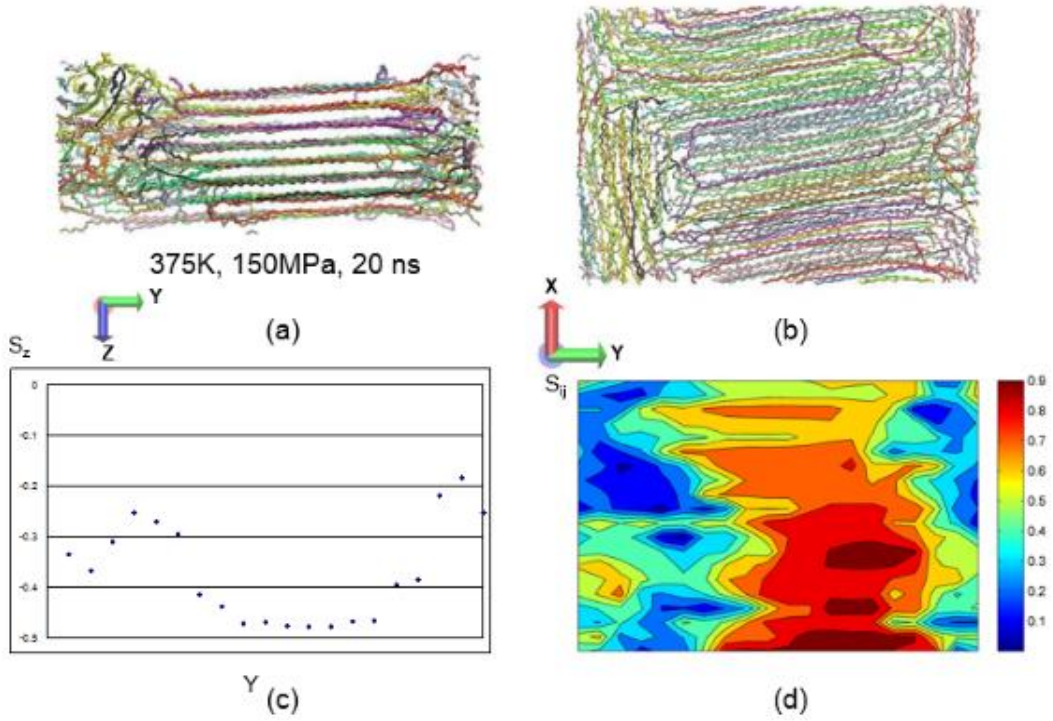

Figure 8-2 (a) Final crystallization morphology (side view) of a free standing polymer thin film under a large biaxial stress of 150 MPa. (b) Top view of the as-crystallized thin film. (c) Hermans' orientation along y axis. (d) Hermans' orientation projected on the xy plane.

The as-crystallized structure is shown in Figure 8-2 (a) side view and (b) top view. The side view of the partially crystallized thin film demonstrates a monodomain of highly oriented crystalline structure with all-trans chains aligned along the stretching direction, which is vertical to the z axis. The defects and less-ordered chains concentrate on the edge of the ordered region, no thickness-dependence of chain orientation is observed. The structure is quite similar to the structure crystallized from highly oriented melt or stress-induced crystallization, both of which are described in detail in Chapter 4.

In this case, stress is the predominant factor for the final crystallization morphology. Combing with the top view (see Figure 8-2b), crystallized chains are also exposed on the free surface. A surface texture with directional order is induced here by the strong biaxial stress.

The Hermans' orientation along the z axis (see Figure 8-2c) is fluctuated largely in the less-ordered region but with a negative value, while in the highly ordered region it is nearly -0.5. This further indicates that the chains inside the crystalline region direct to the thin film surface normal. The 2D Hermans' orientation spectrum projected on the xy plane (see Figure 8-2d) also shows a distinct crystalline domain.

8.2 Crystallization of polymer in presence of surfaces

8.2.1 Crystallization process

The crystallization behavior of polymers is strongly influenced by the substrates that they are attached to. The density and orientation effects on polymer interactions with flat surfaces are also investigated. This part of the investigation consists of two types: the

polymer crystallization behavior of thin films with a single substrate and polymer crystallization behaviors between parallel sheets.

8.2.2 Force field of polymer-surface interactions

As a study concentrating on the crystallization behavior, the substrates are chosen to be featureless purely flat surfaces. The interactions between the polymer united atoms and the substrate are simplified as a Lenard-Jones (LJ) style force field with a cut off distance of 1 nm.

$$E_{LJ} = 4\varepsilon\left[\left(\frac{\sigma}{r}\right)^{12} - \left(\frac{\sigma}{r}\right)^{6}\right], \qquad (8\text{-}1)$$

where σ = 0.401nm. A model wetting surface is selected with a significantly stronger Lenard-Jones interaction parameter $\varepsilon_{wetting}$ = 4.69 kJ/mol with the polymer.

8.2.3 Crystallization of polymer on a single substrate

For a wetting substrate, systems containing 5, 10 and 20 polymeric chains of 400 united atoms were deposited on them. The 2000, 4000 and 8000 united atoms systems are seeded on the diamond lattice before an NVT equilibration for 1 ns with fixed x and y periodic boundaries of 6 nm at 475 K. Upper and lower free surfaces were allowed to relax in the z direction towards vacuum. After equilibration, a flat substrate is brought at a distance of 0.4 nm to the melt, which is the equilibrium interaction distance of the LJ potential. The temperature of the entire system is suddenly decreased to 375 K, to simulate the process of melt deposition on a substrate. Crystallization for 30 ns is performed for the systems to study the morphological, structural and positional changes of the polymer on a

substrate. For comparison, the same structures before loading the substrate are crystallized with the identical condition.

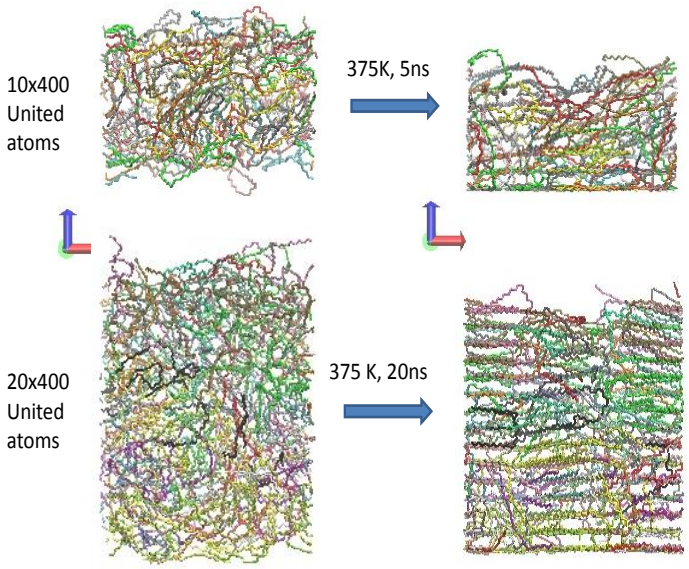

(a)

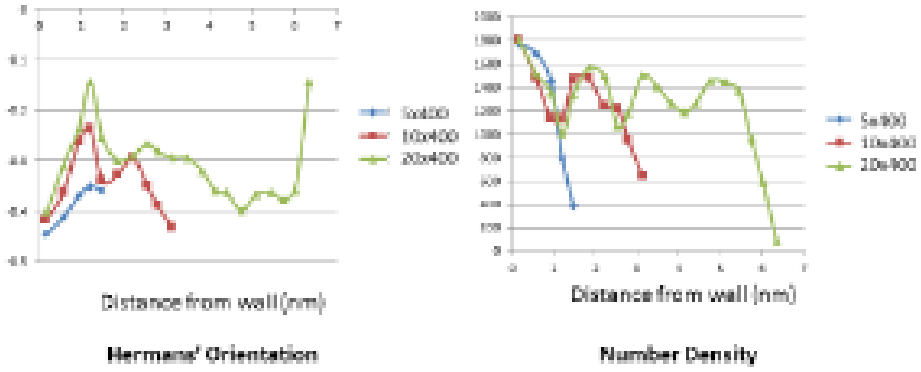

(b) **(c)**

Figure 8-3 (a) Initial and final morphologies of 10 and 20 chain thin films deposited on a substrate with strong attractions. Hermans' orientation (b) and density (c) distributions of the thin films of different thicknesses.

As is shown in Figure 8-3a, final morphologies of 10 and 20 chain thin films deposited on a substrate with strong attractions are illustrated. The Hermans' orientation (see Figure 8-3b) and density (see Figure 8-3c) distributions of the thin films of different thickness are calculated. The Hermans' orientation is taken with respect to the z axis, which is vertical to the substrate surface. The space occupied by the polymer chains are divided into thin layers along the z-axis with an average of 400 repeat unites in each periodic box. The data points for the Hermans' orientation and density are average values over each thin layer.

Owing to the strong attraction, highest densities are observed near the surface, while the chains are nearly vertical to the surface normal, with a Hermans' orientation parameter below -0.4. This indicated the flat-on morphology of polymer chains, which is previously proposed based on experimental observations [92]. On the contrary, the outer layer of each system shows least amount of material along with random Hermans' orientation between samples. This is also a typical feature for a free surface with more degrees of freedom.

Based on the above results and analyses, it was observed that a strong interacting substrate positively affects the density distribution and crystal orientation of the deposited polymer film, even beyond the LJ cut-off distance of 1 nm. This indicates the orientated chains in the near-surface area would further guide the crystallization morphology as a reference or "model layer".

Due to the strong interaction of the substrate and the polymer film (wetting surface effect), the density is significantly higher right near the surface (within LJ cut-off distance) for polymer films of any thickness investigated (see Figure 8-3c). For the thinnest film, the

density drops monotonically towards the free surface, indicating the interaction force filed as a dominating factor. For thicker films, the density at the free surfaces is still lower, owing to fewer restrictions towards vacuum. However, the density also presented periodic fluctuations with depth, which could be attributed to some structural features.

Several indications could be traced from the Herman's orientation spectra with the normal direction to the surface as reference (see Figure 8-3b). A chain vector with an orientation parameter (S) of -0.5 is parallel to the substrate. When the orientation parameter of a chain vector is 0, it has 45˚inclination to the reference and the substrate.

The wetting surface not only introduces a higher density at the near-substrate area, but also brings a flat-on morphology of the polymer chains with respect to the strongly interacting substrate. This phenomenon is recently validated by advanced characterization techniques on the nanoscale. The monotonic increase of S within approximately 1 nm to the substrate indicates that the polymer chains are predominantly influenced by the LJ potential field of the substrate, which decreases with distance to the surface beyond certain length.

However, the orientation parameter decreased again beyond the LJ cut-off distance of the surface (1 nm). This could be attributed the crystallization of polymer chains that introduces increased structural regularity. The density of this region (between 1.5 to 2.5 nm) is also higher than the neighboring regions with a higher or lower depth. For the film with a larger thickness (~6.5 nm), certain periodicity of the density and fluctuations of the Herman's orientation factor are demonstrated, which could also be originated from the consecutive crystalline-amorphous lamellar structure of the semi-crystalline polymeric film.

At the surface area (top 1 nm) of a thin film, the density is significantly lower than those of the center and near-substrate regions, while the orientation varies substantially. This region is the least restricted region with higher mobility of chains towards vacuum. The surface is uneven and random in organization.

Radii of gyration (Rg) in the initial melt and after crystallization of 30 ns for polymeric thin films consisting 10, 20 and 40 chains are demonstrated in Figure 8-4. An increasing trend of Rg with increasing thin film thickness is shown both before and after crystallization. The differences of Rgs between the 20-chain film and 40-chain film are significantly small, compared to the Rg of a thinner film consisting 10 chains. This might be originated from the film thickness. For a film thicker than the Rg of polymer chains (in this case the 20 chain system and 40 chain system), Rg has a relatively weak thickness dependence. However, for the 10 chain system with a thickness around 3 nm, Rg is 2.80 nm, which is much less than the Rg (4.87 nm) of the 20 chain system, which has a thickness above 6 nm. A Rg comparable to the thickness of a polymeric thin film deposited on a wetting substrate is presented when the thin film is below a critical thickness (around 5 nm). This scaling correlation is crucial for polymer thin film design and physical property predictions.

In addition, Rg is also calculated before and after crystallization for all three thicknesses and a rising trend of Rg is presented after crystallization. This might be originated from the all-trans conformation formed inside the crystalline region, which unfolded sections of a chain and increased Rg.

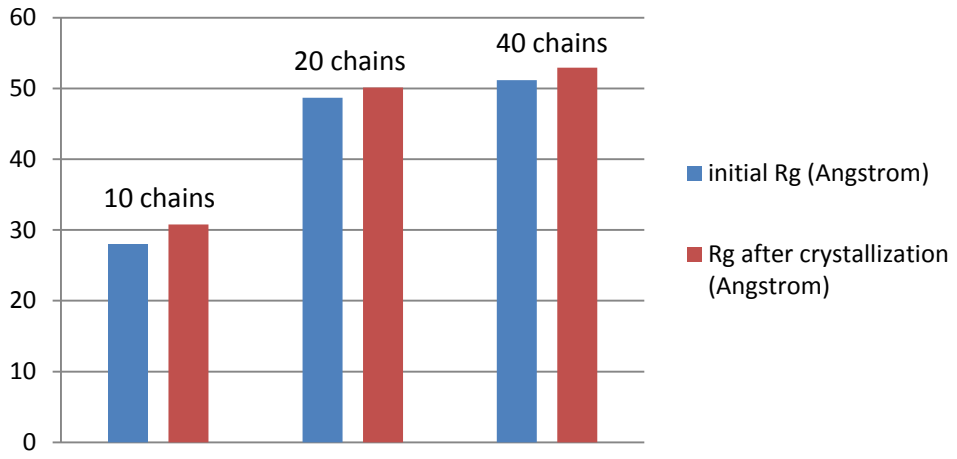

Figure 8-4 Radii of gyration and Radii of gyration before and after crystallization for 10, 20 and 40 chain thin films deposited on a substrate with strong attraction.

8.2.4 Crystallization of polymer between double sheets

After discussing the polymer chains deposited on a single substrate, the behavior between two parallel sheets is also addressed. Strongly interaction parameters were initially defined for both surfaces, to avoid the slippage of chains on the sheets.

Systems consisting of 20 polymeric chains each with 400 united atoms are prepared through the diamond lattice method. Periodic boundary conditions are imposed on the x and y directions, and the box lengths were fixed to 6 nm, while in the z direction free surfaces are generated. In the subsequent equilibrium process, a temperature of 475 K, which is well above the melting point, is imposed on the systems for 1 ns to achieve full relaxation. The x and y directions are held to 6 nm while the free surfaces are allowed to stretch to match the density at the fixed temperature. According to the sizes of the polymeric systems, parallel flat sheets are constructed within the interaction distances of the Lenard-Jones potential, to confine the system. The distances between two sheets are

8.7 nm for the 20 chains systems. Equilibrations of the polymeric melts between parallel sheets are performed for another 1 ns, followed by a quench at 375 K for 20 ns, to observe the crystallization behavior. The equilibration and crystallization of the system under confinements are performed under NPT ensemble with zero stresses in the x and y directions, to allow volume changes during quenching and isothermal crystallization processes.

As is shown in Figure 8-5, crystallization after 16 ns is observed for the 20 chain system, with the spacing between parallel sheets equals 8.7 nm. In addition to the strong flat-on features of the chain system near the surface, local ordering also occurred in the center core. The system is densified significantly in the center.

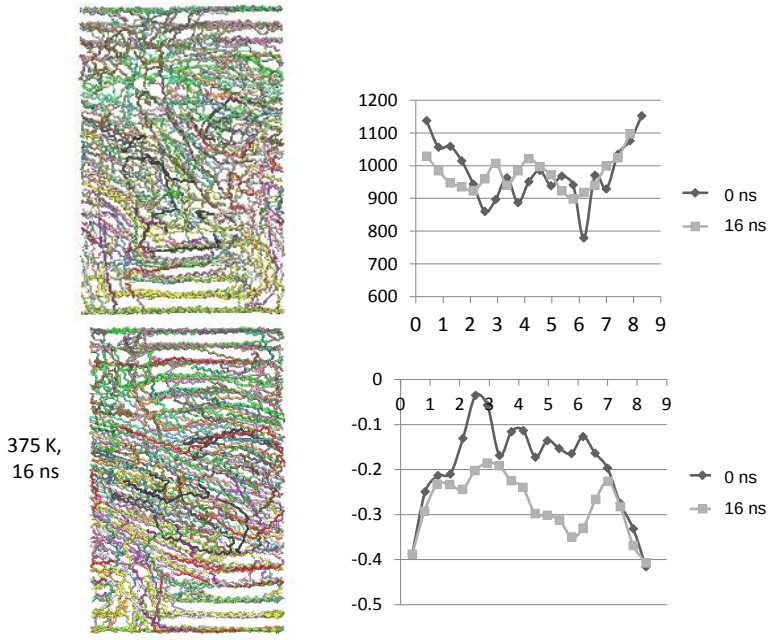

Figure 8-5 Crystallization after 16 ns for the 20 chain system.

For the case of 20 chain system, polymer chains behave differently at the near

surface regions and the center region between parallel sheets. Due to the strong wetting effect of the substrates, the densities are higher in these regions either at the initial stage or at the final solid state. In addition, a flat-on effect characterized by Herman's orientation factor close to -0.5. The central region is predominantly determined by polymer-polymer interaction. Densification combined with increased structural regularity of this region indicate that the amorphous to crystallization process.

8.2.5 Effect of polymer crystallization under shear between parallel sheets

In all the above systems, only dynamics of polymer chains are performed, while the substrates remain immobile. The horizontal relative motion of parallel sheets is of special interest, which physically imitates shearing motions during polymer processing. The crystallization behavior under external stress is also investigated here. Relative motion in the x direction of the parallel sheets with two different speeds are imposed. The relatively "slow" speed is 1 nm/ns, which is comparable to the uniaxial deformation rate imposed to the bulk system (see Chapter 5). The "fast" speed is 10 nm/ns, which corresponds to an ultrafast strain rate of 10^{-8} s^{-1}. The Nose-Hoover thermostat [84-86] is imposed to the entire system during the shear process, to simulation the isothermal crystallization condition during shearing.

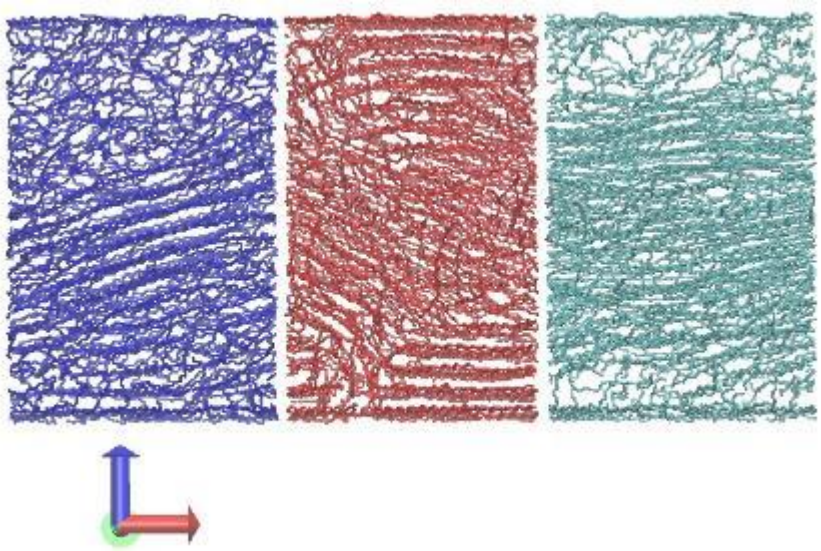

Figure 8-6 Crystallization morphology of a 20-chain system at slow shear (left), fast shear (right) and no shear (middle).

As is shown in Figure 8-6, the crystallization morphology of a 20-chain system at slow shear (left), fast shear (right) and no shear (middle) are presented. As is analyzed above, the crystallization of a system between fixed parallel sheets is characterized by flat-on morphology of the near-substrate regions and crystallization at the central region. Due to the confined size between the parallel sheets (6.5 nm), the center crystallization zone forms a single-crystal-like morphology. The density of the near-substrate region is also higher than that of the region in the center, owing to the influence of the wetting substrates.

However, as the substrate is undergoing a moderate shearing motion during the crystallization process (Figure 8-6a), the scenarios are different. The near-substrate regions, due to the shearing force, the strong orientational order is disturbed and the polymer chains are amorphous. On the other hand, at the center piece of the polymer layer the dynamics is driven by the polymer-polymer interaction and thus forming an integrated crystalline

domain. A monodomain crystalline lamella is formed, neighbored by the less ordered near-substrate regions. Another influence of the shearing force to the system is the crystal orientation. The chains inside a crystalline domain are tilted to accommodate the shearing.

For the case of fast shearing, strong motion of the parallel sheets dominates the behavior of the polymer in between. The near-substrate regions have much lower densities than the center slab, due to the fast motion of the sheets. Polymer chains are generally aligned in the parallel direction and clustered in the center piece, as an influence of the shearing. No well-developed crystalline domain is formed, but rather a highly unidirectional oriented domain. This is because of the strong shearing that disturbs the tranquil crystallization condition to reach a quasi-equilibrium state.

For the above system consisting of 20 chains per periodic simulation box, a single-crystal-like structure is shown, with a uniformed orientation of the crystalline region. However, with increased film thickness, the scenario could be changed. Given enough space, nucleation and growth of nuclei could occur at multiple locations through the film thickness. The shape, size, orientation and inter-crystallite spacing as an effect of thickness confinement are worth studying. The comparison of thicknesses effect and bulk property indicates the unique characteristics of semi-crystalline thin film structures.

In the case of a thicker film between parallel sheets, the polymer morphology with non-shear, slow shear and fast shear conditions are demonstrated in Figure 8-7. For the non-shear condition, in addition to the common characters of a thinner film such as the dense flat-on morphology of polymer chains in the near-substrate regions, different crystalline domains are developed along the thickness dimension with independent chain orientations at a quasi-equilibrium state.

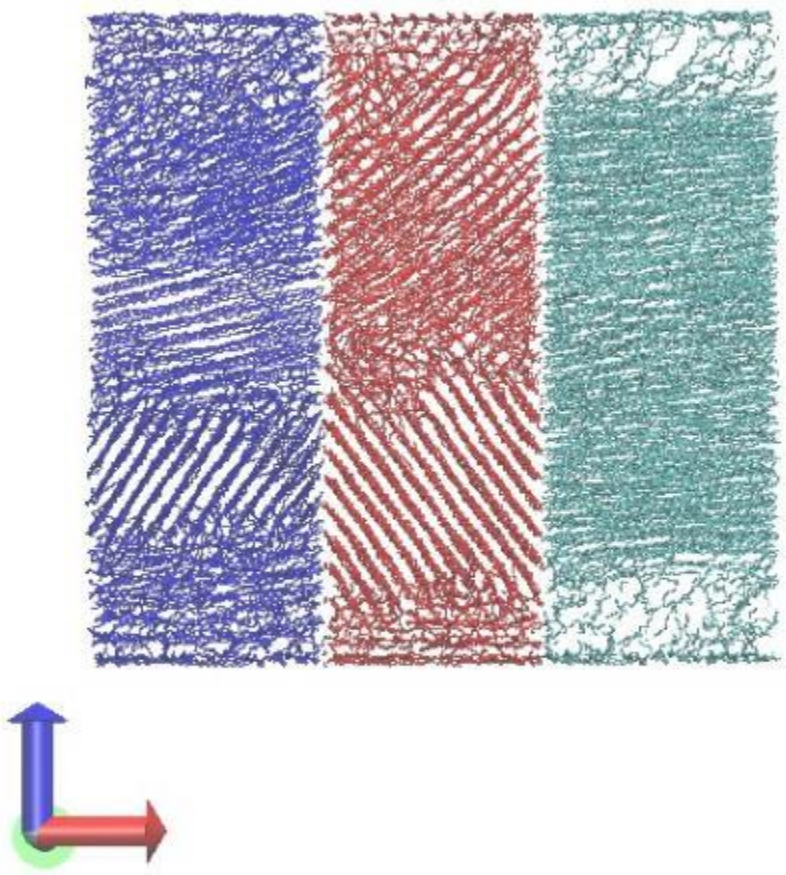

Figure 8-7 Crystallization morphology of a 40-chain system at slow shear (left), fast shear (right) and no shear (middle).

As a slow shearing force is imposed at both ends of the polymer film, the crystallization behavior towards the center region is influenced in terms of how the polymer chains are oriented. The general direction of chain orientation within a crystalline domain could be altered in a way such that the polymer chains are more aligned in the shearing direction. However, distinguishable crystalline domains still exist, i.e. along the z axis, a polydomain semi-crystalline structure with a preferred orientation towards the shearing direction is developed. For fast shearing, since the dominant force for the polymer behavior is the fast shearing between the parallel sheets, the characteristic are rather thickness

independent, featuring a sparse near-substrate area and a monodomain highly unidirectional oriented center slab.

8.3 Conclusions

Free surface plays a key role in the morphology of polymer thin film crystallization. Due to less confinement, chains near the free surface with higher mobility tends to remain amorphous with a slightly trend of flat-on morphology.

Stress could also play a dominant part in the final crystallization morphology. Similar to the role in bulk polymer crystallization, stress can induce and accelerate the crystallization process by reducing the entropy of the system. This chapter concentrates in the discussion of biaxial-stress induced polymer thin film crystallization. At a moderate stress level, the chains in the central region of the film are able to crystallize with unified orientation into a mondomain of crystalline structure. However, the crystallized chains are not aligned in the stretching direction. With strong biaxial stresses that align the chains in the stretching direction in the crystalline region, the free surface could also be crystallized due to less confinement. The featured surface has a crystalline texture consists of highly ordered flat-on chains.

For the thin film crystallization on a single wetting substrate, the near-substrate, central and free surface areas act significantly differently due to the big difference in confinement. Owing to the strong attraction, highest density and flat-on morphology of the polymer chains are displayed near the substrate. The orientated chains in the near-substrate area would even further guide the crystallization morphology as a reference. The central region of a thin film displayed bulk-like crystallization behavior in which the polymer

chain orientation are different than that of the near substrate area. At the surface area (top 1 nm) of a thin film, the density is significantly lower than those of the central and near-substrate regions, while the orientation varies substantially. This region is the least restricted region with higher mobility of chains towards vacuum. The surface is uneven and featureless.

For a thin film crystallized between parallel sheets, in addition to the near-substrate region characterized by densified flat-on chains influenced by the strong attractive force from the substrates, the center region develops into monodomain or polydomain of semi-crystalline structures, depending on the distance between the parallel sheets. Slow shearing between parallel sheet will influent the crystalline domain orientation. Fast shearing breaks the crystallization condition of the central region. The near-substrate area has lower densities, while a monodomain highly unidirectional oriented slab is formed in the center.

CHAPTER 9

ORDERING IN LIQUID CRYSTALLINE SYSTEMS

In the previous portion of the dissertation, process-structure relationships of partially-crystallizable linear polymeric systems were discussed, during which various tools were developed that could be expanded to the analysis of other partially oriented polymeric systems. As an application and validation of the data-analysis and structure-interpretation tools, structural evolution of liquid crystalline elastomers (LCEs) were also investigated with a focus on experimental approaches.

9.1 Synthesis of the mesogenic monomer and liquid crystalline polymer

9.1.1 Materials

4-nitrophenol, diisopropylcarbodiimide (DIC), dichloromethane (anhydrous), 1,2-dichloroethane, 11-bromo-1-undecene, hydride terminated poly(dimethylsiloxane) (PDMS, M_n=580 g.mol^{-1}), 2,4,6,8-tetrmethyl cyclotetrasiloxane, platinum(0)-1,3-divinyl-1,1,3,3-tetramethyldisiloxane (complex, solution in xylene, 2-3%), potassium hydroxide, potassium carbonate, sodium hydroxide, ethanol, methanol, acetonitrile. All the reagents and solvents were commercially available (Sigma-Aldrich) and were used as received.

Dimethylaminopyridinium-toluenesulfonate (DTPS) was synthesized by combining of p-toluene sulfonic acid (TSA) and dimethylaminopyridine (DMAP) which were also adopted from Sigma-Aldrich, and the former have been dehydrated with refluxed toluene before combination reaction.

9.1.2 Synthesis of the mesogenic monomers

4,4'-bis(undec-10-enyloxy)-azobenzene ($C_{11}Ar_2AB$) was synthesized based on the method of previous literature[93-95]. The synthetic route of the other two major mesogenic monomers is depicted in Figure 9-1 **[96].**

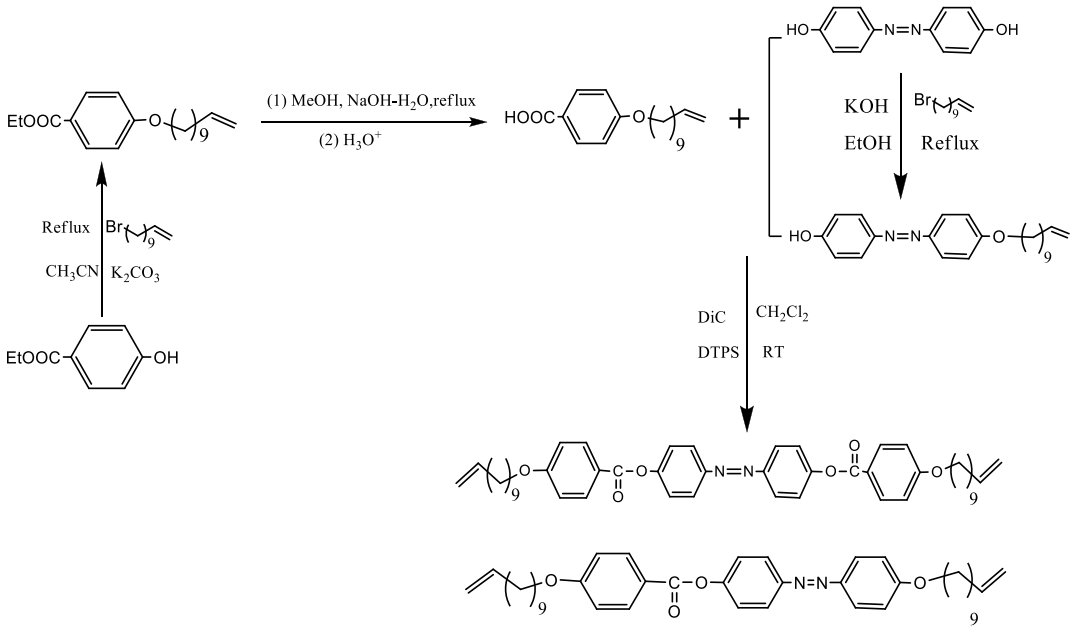

Figure 9-1 Synthetic route of three and four phenyl rings azobenzene monomers ($C_{11}Ar_3AB$ and $C_{11}Ar_4AB$). [96]

9.1.3 Synthesis of main-chain liquid crystalline elastomers

The hydrosilylation method was adapted to synthesize main-chain liquid crystalline elastomers containing azobenzene mesogens based on previous work [43, 97, 98]. The double bonds of the mesogenic monomers and the Si-H group of the siloxane spacer react to form a linear polymer main chain in the presence of the platinum catalyst. The synthetic route is shown in Figure 9-2 [99]. Two types of siloxane chain extenders were selected, with eight Si (m=7) and three Si (m=2), respectively.

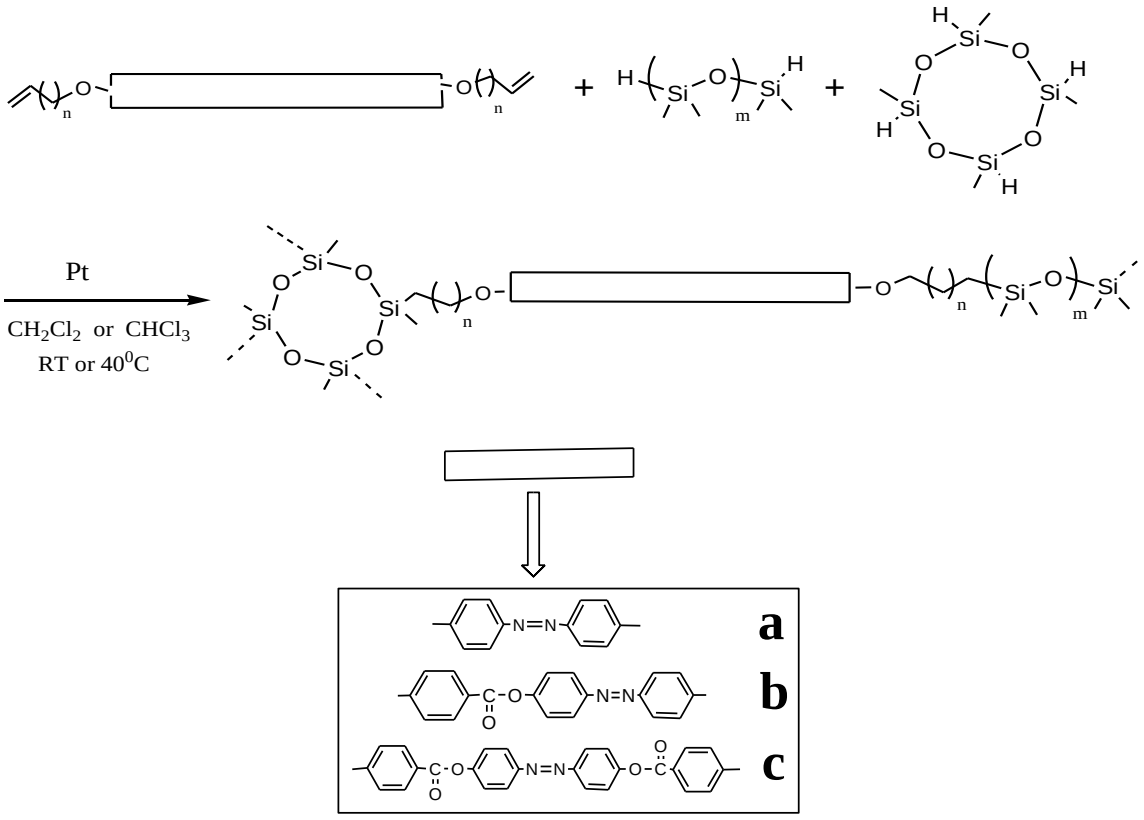

Figure 9-2 Synthesis of LCEs containing different azobenzene moieties (a) $C_{11}Ar_2Si_8XL_{10}$; (b) $C_{11}Ar_3Si_8XL_{10}$ and (c) $C_{11}Ar_4Si_8XL_{10}$. [99]

9.2 Preparation of monodomain liquid crystalline elastomer samples and recovery property with respect to thermal history

To test the stability of strain retention of samples stretched at different temperatures, the temporal dependence of the strain in the stretching dimension immediately after deformation were recorded. To ensure a homogeneous and accurate temperature control over the stretching process, the stretching process were performed at 70 °C and 25 °C in a water bath. The initial strains applied to both samples were 150 %. The film length in the stretching direction were measured by a micrometer at different time intervals. Results are illustrated in Figure 9-3.

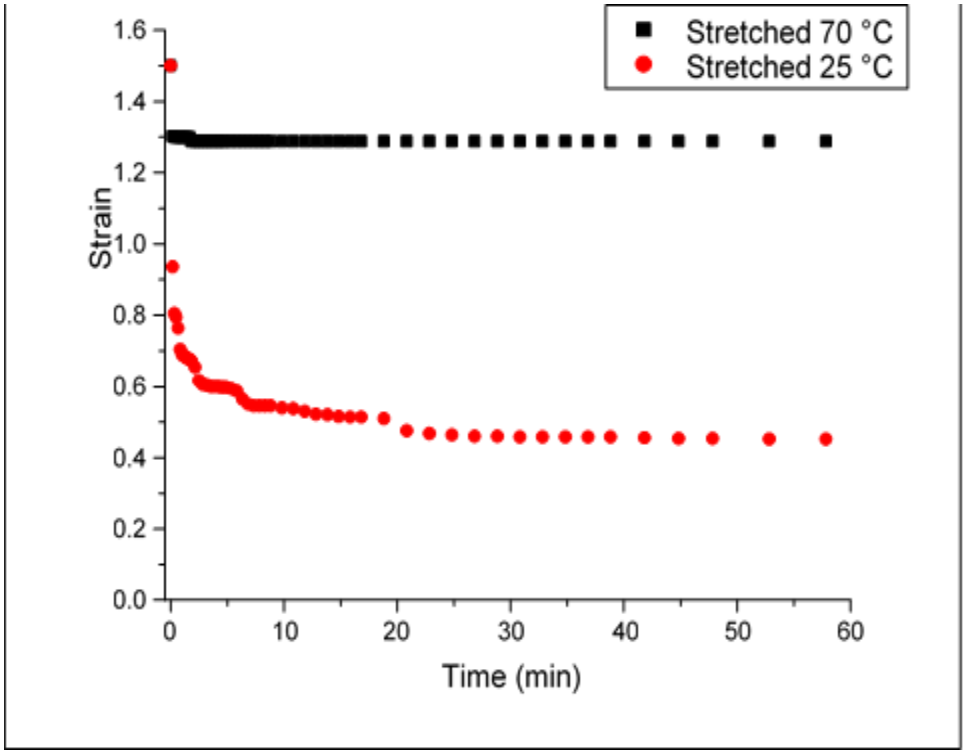

Figure 9-3 Strain retention of $C_{11}Ar_2Si_8XL_{10}$ stretched at 70 °C and 25 °C, respectively.

In Figure 9-3, great differences in the room-temperature strain-retention behavior between the samples stretched at 70 °C and at 25 °C were demonstrated during the first hour of room-temperature stress-free relaxation. The sample stretched at room temperature contracted to a substantial extend during the first 10 minutes and the remained sample length was about only 140 % of the length of the initial film in the stretching direction. The liquid crystalline order was not well "locked in" due to the relaxation.

Similar concerns were raised by previous researchers and a popular solution to the problem was to perform a second crosslinking process after the highly oriented sample to fix the as-stretched structure.[42, 75] The performance was satisfactory but the process involved an additional chemical crosslinking step after polymerization and thus it was rather time-consuming with restricted conditions.

To accelerate and simplify the process for preparing highly oriented monodomain sample and to avoid the second chemical crosslinking process, the protocol of "hot stretching" was proposed. As can be seen from Figure 9-4 b of the black cubes, the sample stretched at 70 °C shrank only slightly within several seconds after exposing to room temperature, before retained good dimensional stability. A sample of at least 230 % of the initial dimension in the stretching direction was prepared.

Inspired by the above dimensional stability experiments, the following preparation protocols of sample preparation were executed. The two-phenyl-ring azobenzene monodomain LCE ($C_{11}Ar_2Si_8XL_{10}$) strip samples were prepared by stretching the initially polydomain samples at 120 °C，which was above the isotropic transition temperatures (as can be proved by the DSC data to be presented later in the chapter), and were annealed under load at 60 °C for 3 min, then the load was removed and they were allowed to cooled down to room temperature. The three- and four-phenyl-ring azobenzene monodomain LCE ($C_{11}Ar_3Si_8XL_{10}$ and $C_{11}Ar_4Si_8XL_{10}$) strip films were prepared by stretching the polydomain samples at 120 °C，which were under the isotropic transition temperatures and above the smectic to nematic transition temperatures (see discussions on the DSC curves later in the chapter). They were annealed under load at 60℃ for 3min, before load removal and cooling down to room temperature.

For $C_{11}Ar_2Si_8XL_{10}$, the stretching temperature is already over its clearing temperature ($T_{Sc\text{-}Iso}$= 74 °C). As is shown in Figure 9-4 (a), the molecular chains are oriented in the stretching direction from an isotropic state. However, for $C_{11}Ar_3Si_8XL_{10}$ and $C_{11}Ar_4Si_8XL_{10}$, stretching temperature is below the clearing temperatures. The samples undergo polydomain-to-monodomain transitions at their smectic phase (see Figure 9-4b).

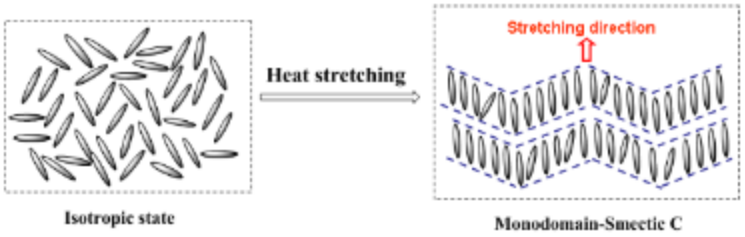

(a) $C_{11}Ar_2Si_8XL_{10}$

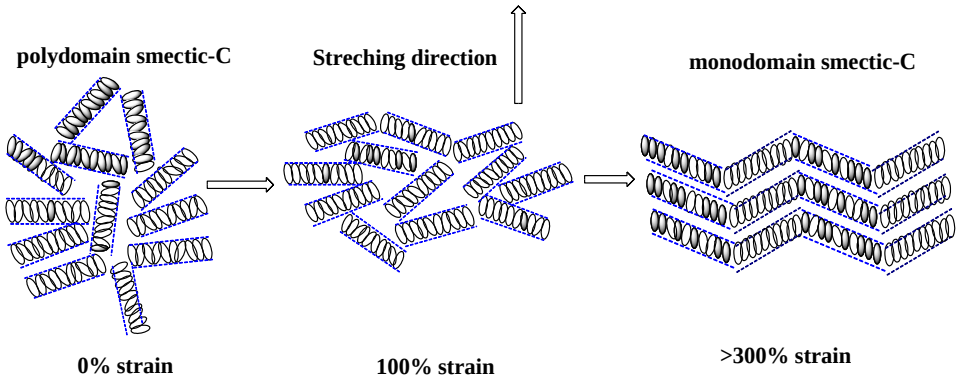

(b) $C_{11}Ar_3Si_8XL_{10}$ and $C_{11}Ar_4Si_8XL_{10}$

Figure 9-4 (a) Schematic representation for monodomain formation of $C_{11}Ar_2Si_8XL_{10}$ from isotropic state (b) Schematic representation for monodomain formation of $C_{11}Ar_3Si_8XL_{10}$ and $C_{11}Ar_4Si_8XL_{10}$ from polydomain.

After checking the room temperature dimensional stability over time of the LCE samples, thermal stability of samples with different thermal history was evaluated. The results were shown in Figure 9-5. The identical polymer films after two weeks of relaxation after sample preparation procedures discussed in Figure 9-3 were used in the experiment. Lx0 and Ly0 refers to the length and width of both films before stretching, which were cut from as-casted films without a preferred macroscopic orientation. The length (Lx) and the width (Ly) of both dimensions were measured directly after taking out of a water bath with a heating rate of 1 °C/min.

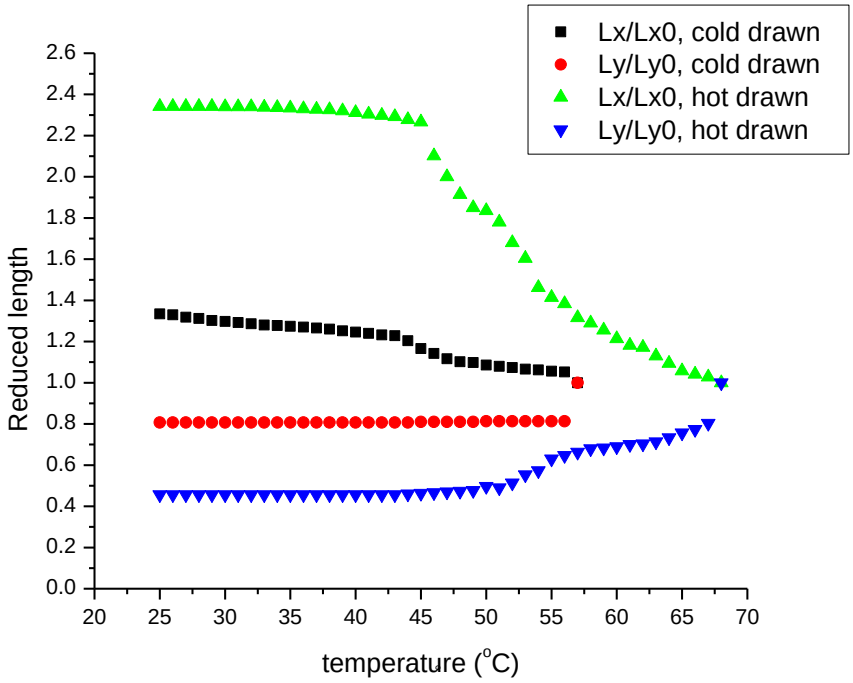

Figure 9-5 Thermal stability of $C_{11}Ar_2Si_8XL_{10}$ films prepare at 70 °C and 25 °C, respectively.

The results in Figure 9-5 show significant differences of the polymer thin films prepared at different temperatures. The film stretched at room temperature changed back to the original unoriented size at a temperature around 57 °C, while the film stretched at 70 °C recovered back completely at 68 °C, which is close to the transition temperature to the isotropic state. More specifically for the cold drawn sample, the x dimension shrank steadily from 25 °C until a sharp drop beginning at around 43 °C and finished at 57 °C. No width change was captured until the jump back at 57 °C. For the hot drawn sample, the sharp turn into a fast drop period in the x dimension occurred at approximately 45 °C, while the width began to increase at around 50 °C. A jump close to 68 °C was also displayed. The experiment demonstrated better thermal stability of the hot drawn sample.

9.3 Characterizations of the reactive azobenzene-containing main-chain LCEs and LCPs

The DSC measurement was performed on a specimen of about 7~15mg at a heating and cooling rate of 10°C/min under a nitrogen flow of 50 mL/min. The instrument was calibrated by using indium as a standard. The collected data was analyzed by the TA Universal Analysis software.

The glass transition temperatures of the azobenzene-containing LCEs are reported from the maximum tanδ (loss modulus/storage modulus) by a stress-controlled DMA (Netzsch DMA 242E) with a heating rate of 3 °C/min in a nitrogen atmosphere. The phase transition temperature and corresponding latent heat of LC monomers, polymers, and elastomers was determined by a TA Q200 differential scanning calorimeter.

The molecular weights and polydispersity indexes (PDI) of linear polymeric products of the azobenzene-containing dialkenes and poly(dimethylsiloxane) via hydrosilylation were listed in Table 9-1. The M_n of all three products were over 20,000 with a relatively narrow distribution, indicating good reactivity of the three monomers. Following the synthetic route in Figure 9-2, elastomeric thin films could be peeled off from PTFE dishes after solvent evaporation.

Table 9-1 Molecular weight and PDI of azobenzene-containing LCPs.

Polymer	Mn (g/mol)	Mw (g/mol)	PDI (Mw/Mn)
$C_{11}Ar_2Si_8XL_0$(LCP)	24917	56955	2.286
$C_{11}Ar_3Si_8XL_0$(LCP)	22597	39434	1.745
$C_{11}Ar_4Si_8XL_0$(LCP)	26318	44015	1.672

The azobenzene-containing monomers displayed different liquid crystalline phase transitions, which were characterized by the DSC first cooling (see Figure 9-3 a) and second heating curves (see Figure 9-3 b). In Figure 9-3 (b) of $C_{11}Ar_2AB$, only the crystallization peak (Tc_r=96.0 °C) and nematic to isotropic transition peak (T_{NI}=107.5 °C) were presented. $C_{11}Ar_3AB$ showed three transition peaks, corresponding to the crystallization temperature (Tc_r=74.8 °C), the smectic to nematic transition temperature (T_{Sc-N}=143.2 °C) and the nematic to isotropic transition temperature (T_{NI}=183 °C). For $C_{11}Ar_4AB$, in addition to the three above transition temperatures Tc_r（123.5 °C）, T_{Sc}（180.9 °C and T_{NI}（270.5 °C）, two crystal-to-crystal transition temperatures between different crystalline phases were also demonstrated.

DSC first cooling and second heating curves of the linear liquid crystalline polymers (LCPs) were shown in Figure 9-6. All three LCPs demonstrated both the smectic to nematic transition peak T_{Sc-Iso} and the nematic to isotropic transition peak. The curves also indicated a trend of increasing liquid crystalline to isotropic transition temperatures with the increasing length of the mesogen. No significant enthalpy differences were shown. The transition points and enthalpy are listed in Table 9-2.

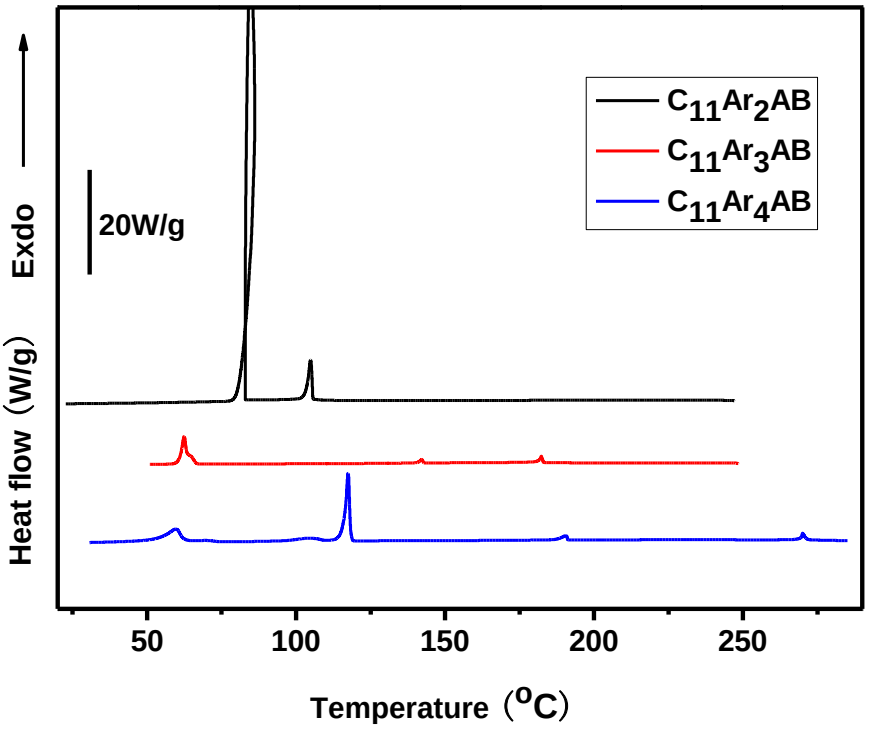

(a)

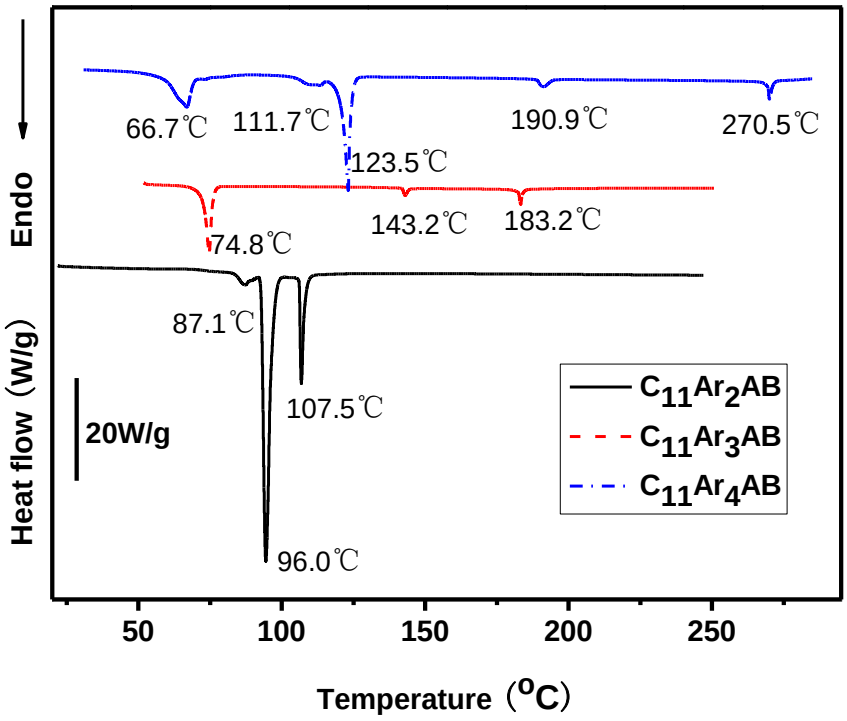

(b)

Figure 9-6 DSC profile of (a) 1st cooling; (b) 2nd heating at 10 °C/min of monomers.

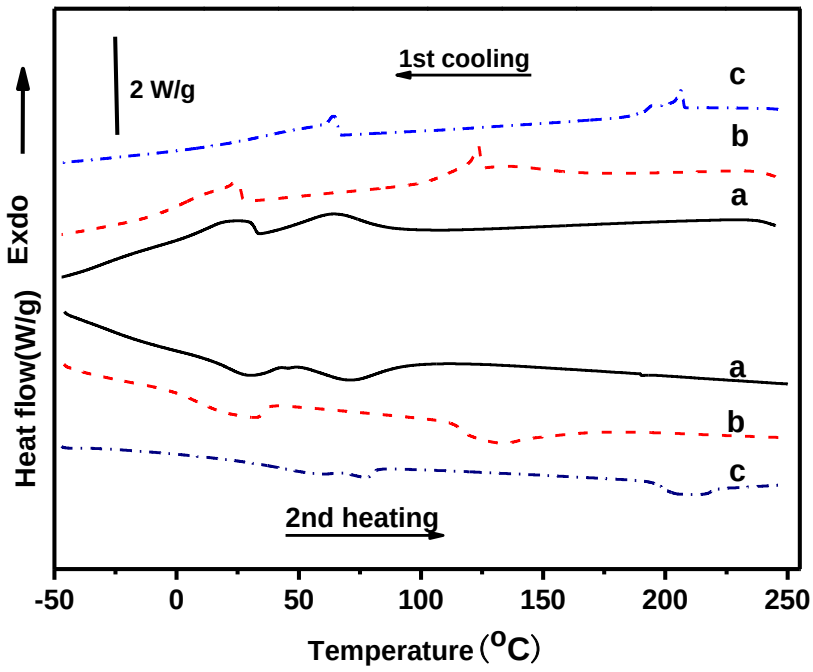

Figure 9-7 DSC profile (1st cooling and 2nd heating, 10 °C/min) of LCPs containing azobenzene mesogens. (a) $C_{11}Ar_2Si_8XL_0$, (b) $C_{11}Ar_3Si_8XL_0$ (c) $C_{11}Ar_4Si_8XL_0$.

Table 9-2 Thermal transition of azobenzene-containing LCPs and LCEs.

polymer	T_{Sm-N} (°C)	ΔH_{Sm-N} (J/g)	T_{N-Iso} (°C)	ΔH_{N-I} (J/g)	polymer
$C_{11}Ar_{2\text{-}LCP}$	27.0	4.52	74.0	6.52	$C_{11}Ar_2XL_{10}$
$C_{11}Ar_{3\text{-}LCP}$	27.0	5.62	140.0	4.35	$C_{11}Ar_3XL_{10}$
$C_{11}Ar_{4\text{-}LCP}$	61.0	3.85	222.0	5.05	$C_{11}Ar_4XL_{10}$

9.4 Morphological evolution of the polydomain to monodomain transition of the azobenzene-containing main-chain LCEs

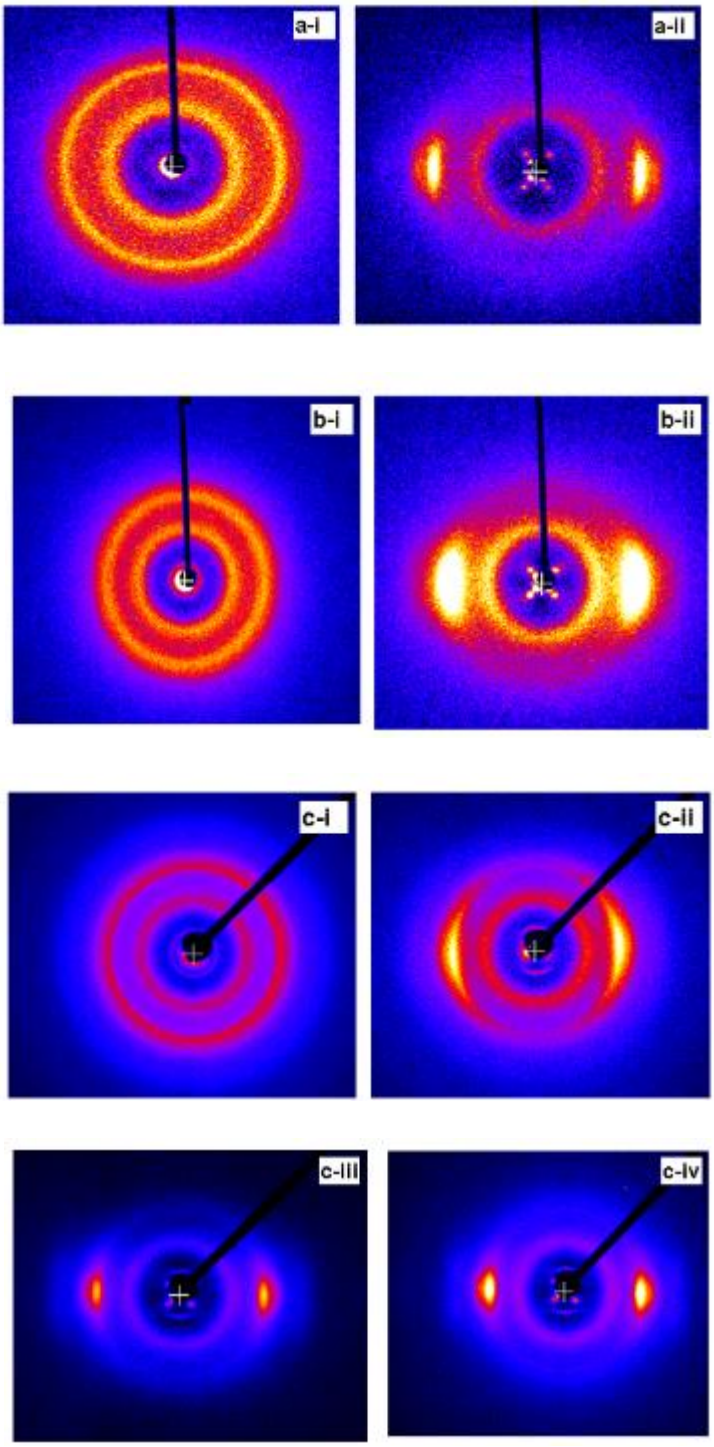

Figure 9-8 2D WAXS pictures of (a) $C_{11}Ar_2Si_8XL_{10}$, (b) $C_{11}Ar_3Si_8XL_{10}$ and (c) $C_{11}Ar_4Si_8XL_{10}$ at different draw ratios. Strain levels of a-i, a-ii is 0%, 250%; b-i, b-ii is 0, 250%; c-i, c-ii, c-iii, c-iv is 0 %, 100 %, 200 % and 340 % respectively.

Both wide angle X-ray diffraction (WAXD) and small angle X-ray scattering (SAXS) measurements of elastomer specimens were performed at room temperature with a Rigaku Micromax-002 (Cu, λ=1.5418Å) diffractometer and a Rigaku R-axis IV++ 2-D detection system. The order parameter was calculated by an azimuthal scan applied to the smectic inter-mesogen reflexes. Data were analysis by the Jade software package.

As is shown in Figure 9-8, X-ray diffraction patterns of the as-cast and strained LCE thin films were obtained to identify their morphological characteristics. For the LCEs with two and three benzene rings, only patterns at two extreme cases were shown, i.e. as-cast films and uniaxially highly-stretched films (over 300 % strain). For the LCE thin film with four benzene rings, the XRD patterns of the as-cast film, and uniaxilly stretched films at pre-strain levels of 100 %, 200 %, and 340 %, respectively. Characteristic lengths, tilting angles and order parameters of highly stretched thin films derived from XRD patterns were summarized in Table 9-3.

Table 9-3 2D WAXS characterization data of the monodomain MCLCE films.

Sample	2θ (°)			d (nm)			φ (°)	S
	$2\theta^{m}$	$2\theta^{s}$	$2\theta^{Sc*}$	d^{c}	d^{s}	d^{l*}		
$C_{11}Ar_2Si_8XL_{10}$	20.18	12.28	2.03	0.44	0.72	4.35	44.92	0.90
$C_{11}Ar_3Si_8XL_{10}$	19.82	12.21	2.07	0.45	0.73	4.27	35.40	0.88
$C_{11}Ar_4Si_8XL_{10}$	18.98	12.45	1.82	0.47	0.71	4.86	48.04	0.87

$2\theta^{m}$, $2\theta^{s}$ and $2\theta^{Sc*}$ refer to the X-ray reflection angles of the mesogen layers, backbones of siloxane chains, smectic-C layers, respectively, d^{m}, d^{S}, d^{Sc*}, and d^{Sc**} denote the d-spacing values of the azobenzene based mesogens, siloxane chains and the smectic-C layers.

The as-cast films show typical polydomain liquid crystalline material

characteristics in the 2D-XRD patterns, featuring diffraction rings at both small angle and wide angle regions without an obvious azimuthal maximum. For the uniaxially highly-stretched thin films, azimuthal repeat peaks were shown at both small angle and outer wide angle regions, with the exception of less-featured diffraction halos at 2θ between 12˚ and 13˚. Specifically, the small angle diffraction showed an off-axis four-spot pattern, which is characteristic to the liquid crystalline smectic-C layers, with correlation lengths ranging from 4-5 nm, depending on sizes of the mesogen group. At the wide angle regions with a characteristic length around 0.45 nm, two strong equatorial peaks were demonstrated, which were attributed to the correlations between the hydrocarbon chains and mesogen groups. The diffraction halo at mid-wide angle region corresponded to the amorphous layers aggregated from the siloxane chain-extender and crosslinkers. For the LCE with the longest mesogenic group ($C_{11}Ar_4Si_8XL_{10}$), XRD diffraction experiments of thin films at intermediate strain levels were also carried out, to observe the transition between the unoriented polydomain morphology to the highly oriented monodomain morphology. At moderate strain (200%), arcs appeared in the small angle region, indicating the development of anisotropic long-range correlations between the smectic layers inside the LCE. The long arcs at the wide-angle region around the equatorial position corresponded to the lateral correlations of the rigid mesogen groups and flexible hydrocarbon chains. As the strain increased to 340%, the characteristic four-spot diffraction pattern was demonstrated, indicating a well aligned monodomain smectic-C LC phase, with calculated order parameters approaching 0.9. The polydomain-to-monodomain transition of azo-benzene smectic-C LCEs were also reported previously for side-chain LCE [68] and main-chain LCE copolymers [100].

9.5 Photoresponsive behaviors of the azobenzene-containing main-chain LCEs

The mechanical properties and photo-generated stresses of the azobenzene-containing LCE films (20×2.0×0.05~0.06mm) were irradiated under Model UVGL-25 (Ultra-violet product Ltd., 115V×0.16A) and measured by a strain-controlled dynamic mechanical analyzer (DMA, TA Instruments RSA III) in tension.

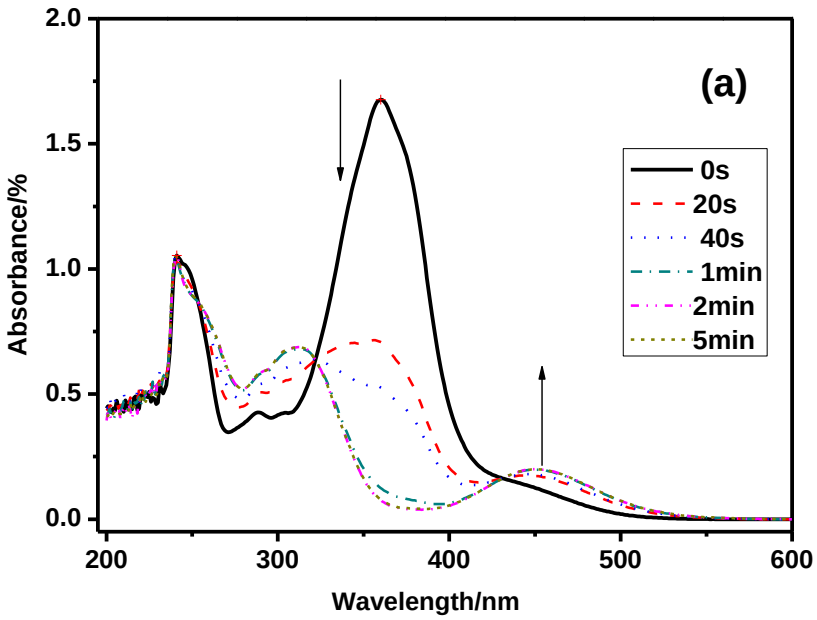

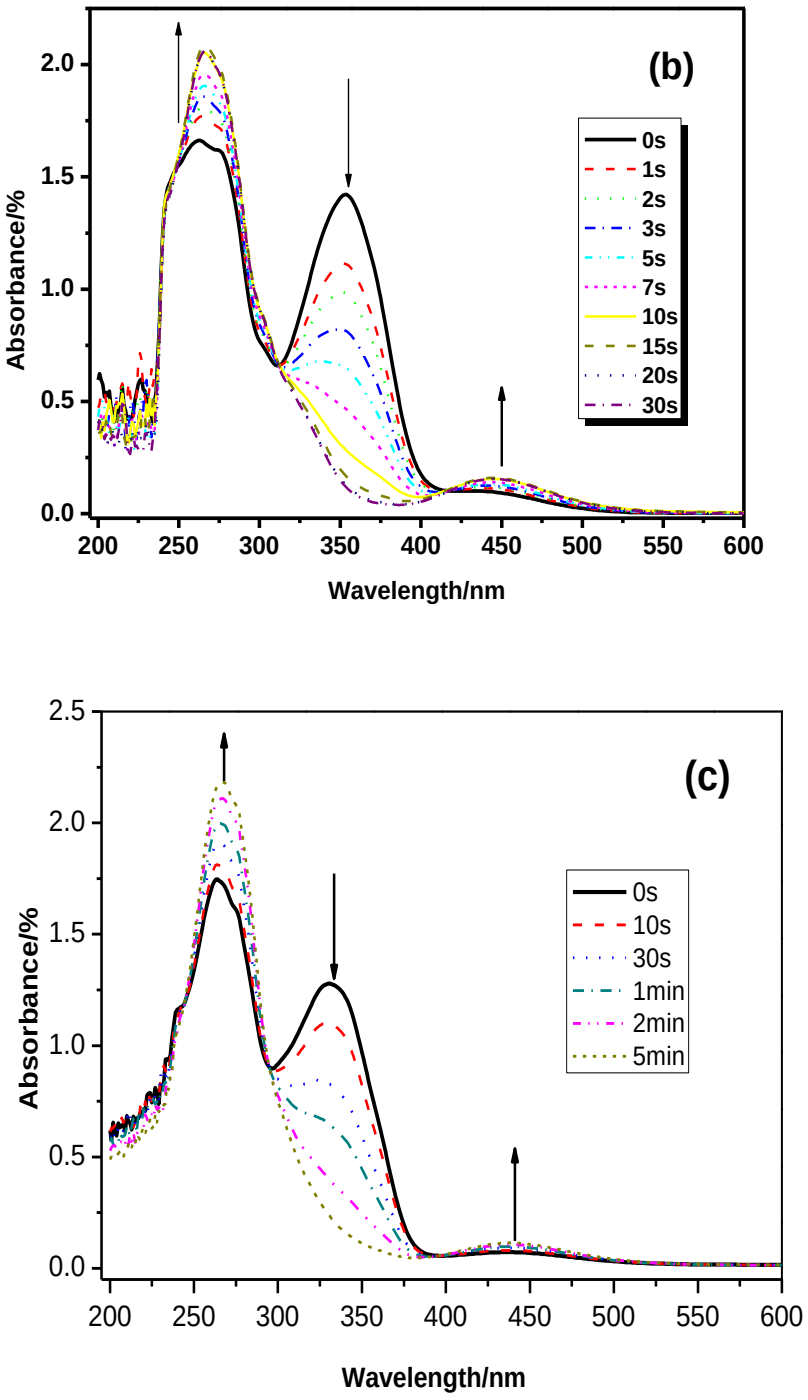

Figure 9-9 UV-vis spectral change in dependence of time for the solution of monomers (a) $C_{11}Ar_2AB$, (b) $C_{11}Ar_3AB$ and (c) $C_{11}Ar_4AB$ in chloroform solution at room temperature unpon irradiation with 365nm UV light.

The UV-vis spectra of azobezene-containing compounds at different irradiation time are shown in Figure 9-9. As the *trans* to *cis* isomerization of the azobenzene group initiated by UV exposure, the absorption of the K-band of π-π* transfer (at 360 nm, 354 nm, 331 nm, respectively) decreased with increasing irradiation time, while the weaker peaks at 453 nm, 451 nm and 441 nm which corresponded to the R-band of n-π* transfer increased with time.

For $C_{11}Ar_3AB$ and $C_{11}Ar_4AB$, the R-band absorption of the carbonyl group at 266 nm and 264 nm increased with time. This indicated that the energy absorbed from UV irradiation could be dissipated by both the n-π* transfer of the azobenzene group and the n-π* transfer of the carbonyl group. Also illustrated from the UV-vis spectra of $C_{11}Ar_2AB$, $C_{11}Ar_3AB$, $C_{11}Ar_4AB$ are 1 min, 20 s and 2 min, respectively. The equilibration time of the *trans-cis* isomerization of the symmetric structures was longer than that of the asymmetric one.

The photo-induced stress-strain behavior of azobenzene-containing compounds were characterized by the stress change of monodomain LCE films upon UV exposure at fixed gauge length.

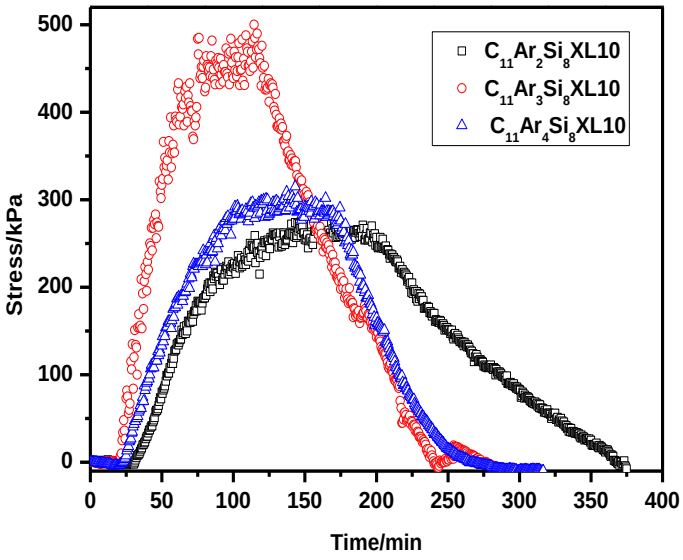

(a)

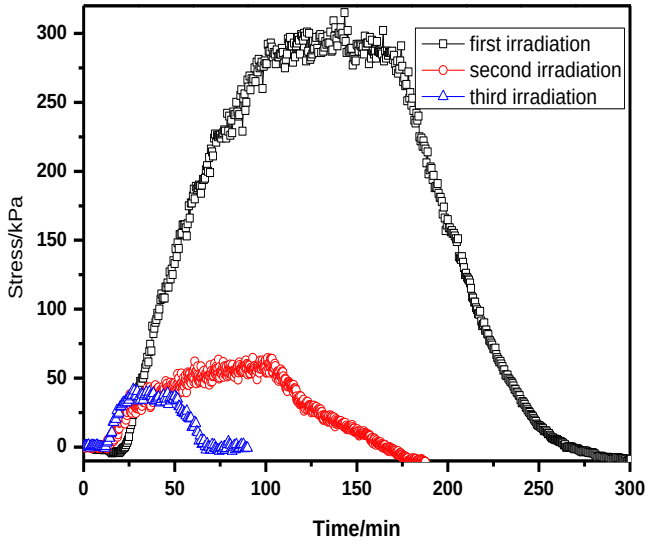

(b)

Figure 9-10 (a). Temporal response of $C_{11}Ar_2Si_8XL_{10}$ (□), $C_{11}Ar_3Si_8XL_{10}$ (○), and $C_{11}Ar_4Si_8XL_{10}$ (Δ) in a stress upon 1st exposure to 365 nm UV light; (b). Temporal response of $C_{11}Ar_4Si_8XL_{10}$ in a stress upon 1st (□, after stretching), 2nd (○, after 5 days), 3rd (Δ, after 45 days) exposure to UV 365 nm light.

As is shown in Figure 9-10 (a), after stabilization of the clamped thin films at zero initial stress condition, irradiation by a weak UV lamp was initiated. As is illustrated in the Figure 9-11, the well-aligned all-*trans* azobenzene-containing mesogens began to go through *trans* to *cis* isomerization, thus generated a contractive force (see Figure 9-12b). The relatively fast conversion rate from *trans* to *cis* state dropped constantly as the consumption of the *trans* isomer near the surface region of the thin film under exposure, until an equilibrium state of the amount of *trans* and *cis* isomers upon irradiation, featuring a plateau at a positive stress level. After the UV lamp was turned out, the azobenzene isomers at the *cis* state steadily transformed to the energetically more favorable *trans* state. The stress between fixed clamps dropped *continuously*, indicating the extensive force corresponding to the *cis* to *trans* isomerization. The stress level reached zero after an isomerization between the UV-activated state and the ground state inside monodomain LCE films.

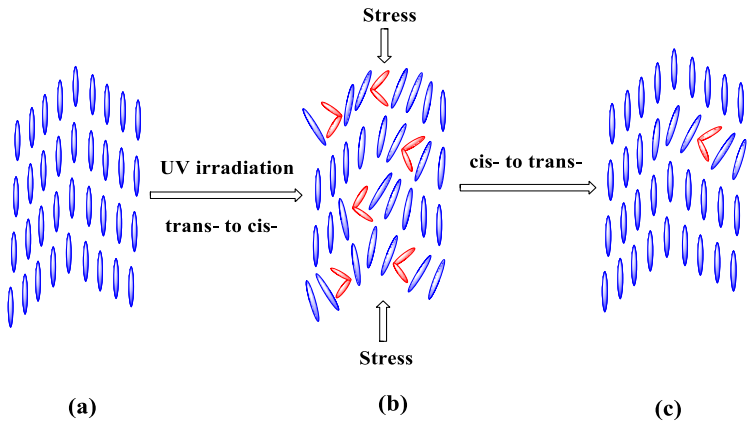

Figure 9-11 Order change of local smectic-C part of LCE containing azobenzene mesogens under UV irradiation.

Specifically, the LCE containing the azobenzene-only mesogen ($C_{11}Ar_2Si_8XL_{10}$)

has the slowest response, presumably due to the rigidity of the azobenzene groups. In comparison, the LCE with a longer mesogen of two symmetric phenyl rings attached to the 4, 4' locations of the azobenzene groups through flexible ester groups responded faster to external irradiation. Impressively, the photo responsiveness of the LCE with an asymmetric mesogen ($C_{11}Ar_3Si_8XL_{10}$) was faster and achieved a much higher stress level, approaching 500 kPa. To the best knowledge of the authors, this is the highest stress level ever reported for the azobenzene-containing LCE thin-film systems. It is speculated that the asymmetric nature of the mesogen structure of $C_{11}Ar_3Si_8XL_{10}$ brought more degrees of freedom during the *trans-cis* isomerization inside the system. Although it is difficult to characterize directly the kinetics of photo activation of different LCEs at the solid state, the faster *trans* to *cis* isomerization of the asymmetric small molecule in solution supported the effect inside the elastomer.

In addition to the immediate response to UV irradiation of as-cast films, response of a sample ($C_{11}Ar_4Si_8XL_{10}$) under second and third exposure was also examined. In Figure 9-12 (b), the second irradiation after five days of the initial irradiation with identical conditions yielded much weaker yet appreciable responses. The third irradiation experiment after relatively long-term storage in dark (45 days) presented similar responses to the second test.

9.6 Design of reversible photo-actuator based on the photo responsive LCE

Owing to the restrictions of the smectic-C layer at room temperature, the rate of response is rather slow. Three hours is expected to reach a stress maxima after UV-irradiation, while a complete cycle of loading and unloading costs approximately 10 hours.

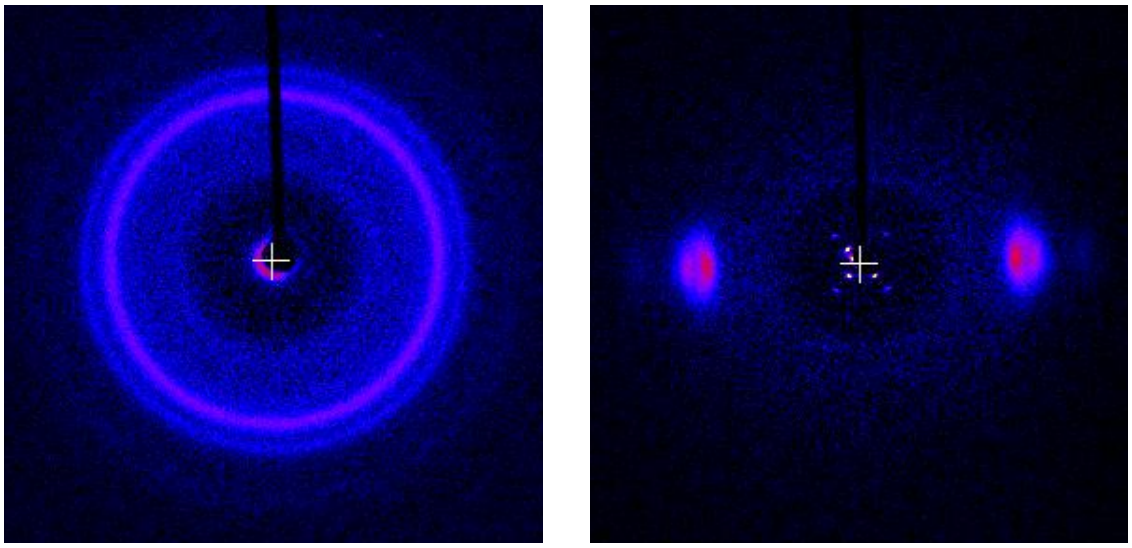

(a) **(b)**

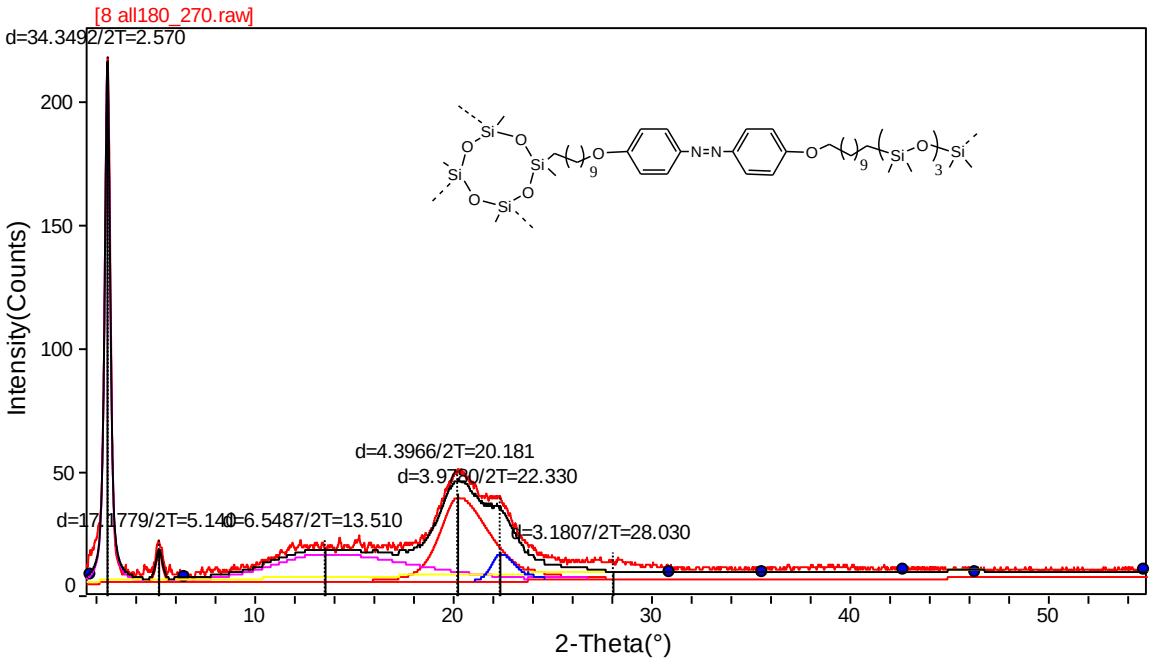

(c)

Figure 9-12 (a) 2DXRD pattern of $C_{11}Ar_2Si_3XL_{10}$ at 0 strain; (b) 2DXRD pattern of $C_{11}Ar_2Si_3XL_{10}$ at 300 % strain; (c) peak decomposition based on XRD data.

Although doing experiments at elevated temperatures [68, 72] will speed up the relaxation, the maximum stress is expected to decrease with reduced rigidity of the backbone [71], while the requirement of an additional heat source might limit some potential applications of the material.

Table 9-4 Peak decomposition and assignment of 2DXRD data of $C_{11}Ar_2Si_3XL_{10}$.

2θ (°)	d(Å)	Structure
2.57	34.3	1st order long spacing
5.14	17.2	2nd order long spacing
13.51	6.5	Trisiloxane
20.18	4.4	C-C
22.33	4.0	π-stacking

To achieve the fully reversible actuation by a single monochromic light source at room temperature in a timely manner, an improved actuation scheme was designed, to reduce the actuation cycle from more than 600 min to 25 min.

The material used is similar to the previously characterized LCE with two phenyl rings in the mesogen. The only difference is the shorter chain extender (Si_3) used in the main chain chemistry (see inset of Figure 9-12 c). The glass transition temperature is expected higher than the Si_8 version. The structure is highly ordered with an order parameter of 0.85 based on the XRD pattern of highly stretched sample (Figure 9-12 b). One-dimensional peak decomposition of the two-dimensional pattern is shown in Figure 9-12 (c). Characteristic smectic-C pattern were demonstrated, with off-axis four-spot patterns for the primary and secondary diffraction. A detailed peak assignment is shown in Table 9-4. The outer equatorial arch was assigned to π-stacking of benzene rings from different mesogenic units inside a crystalline domain, which were not well-separated in the

diffraction pattern that were previously discussed.

After an initial equilibration for 20 min to confirm that no residual stresses remained, the LCE film were exposed to UV light, which in response generated a stress of approximately 170 kPa after 5 min. Since at this stress level the trans-cis isomerization is far from the quasi-equilibrium state, the response is rather fast. This design solved the intrinsic problem for potential actuation applications brought by the long relaxation time of main-chain LCEs. The relaxation time of photo-initiated trans-cis isomerization in a similar main-chain LCE is reported to be approximately one hour at room temperature [72, 73].

After the UV light is off, 20 min relaxation was performed, which relatively quickly relaxed to a stress level below 50 kPa. The above mentioned 5-min-on and 20-min-off cycles were performed several times, to achieve fast and reproducible actuation of the LCE film (see Figure 9-13). The last six cycles shown in Figure 9-13 illustrated a reliable photo-tune actuator between stress levels of 50 kPa and 220 kPa.

The resultant stress response is much higher than the previous reports of any azobenzene containing LCE [68, 72], and is comparable to tough glassy films with very high Tg [46, 65]. The reason for the significantly larger response is attributed to the linear main-chain conformation of the LCE monodomain film. This work is one of the few attempts to synthesize the photo active azobenzene group as mesogen in the main chain of LCE, while in the previous reports by Finkelmann et al. [68, 72] and Ikeda et al.[44, 62], the azobenzene moieties were either on side-chains as pendant groups or as crosslinkers between polymer chains.

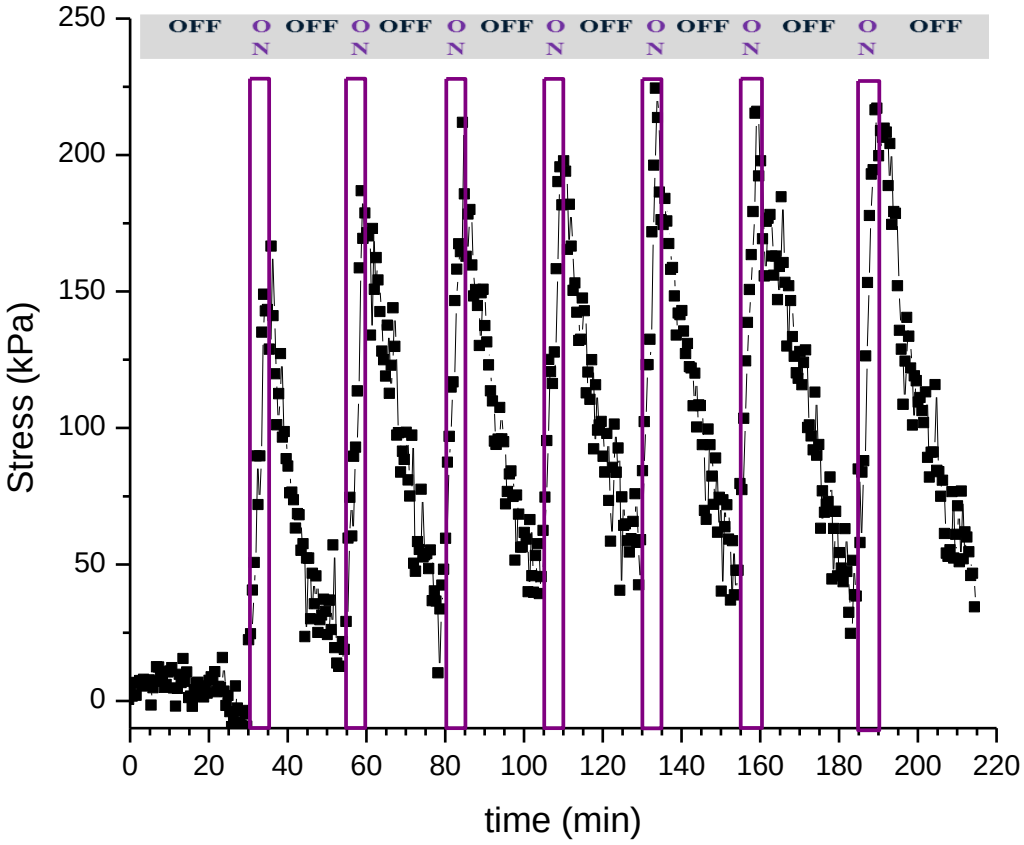

Figure 9-13 Cyclic loading-unloading test of a photo-actuator.

Due to the linear main-chain topology, in which the trans-azobenzene groups are well aligned in the chain orientational direction, the photo-response is a representation of collective motion of the backbone, rather than the local side-chains and crosslinking points. In addition, the molar ratio of the photo-active azobenzene group is much higher than that in the side-chain or crosslinked samples. The two aspects mentioned above give rise to the significant response of the linear main-chain LCE film.

The design of the actuation experiment is aimed at an efficient and reproducible photo-actuator. Although the temperature-tuned actuators relying on the shape memory

effect has been widely documented [52, 101-104], only several reports discussed about photo-directed actuators showing periodic loading and unloading curves. Tsoi and Ikeda et al. [105] were able to develop photo-induced nanoparticles repeatedly tuned their shapes by UV (365 nm) and blue laser light (430 nm). Harada [49] and White [46, 65] et al. successfully changed the bending angle of azobenzene containing polymeric films by alternating UV and visible light irradiation. However, the above experiments were based on the measurements of the extreme values of a form factor (height or angle).

To our knowledge, no previous record was shown to clearly demonstrate the time-resolved stress response of a single-wavelength directed actuator. Both the response time and accuracy of stress control were improved by taking advantage of the initial nearly linear region of the loading and unloading curves, respectively.

9.7 Simulations on azobenzene-containing polymers

All-atoms molecular models of the azobenzene-containing polymer $C_{11}Ar_2Si_8$ was built with the Cerius2 software package. A repeat unit (see Figure 9-14a) was constructed before a linear polymer chain was grown with 20 repeat units (see Figure 9-14b). Three identical chains were brought in a system with periodic boundary conditions (see Figure 9-14c) to simulate bulk polymer properties.

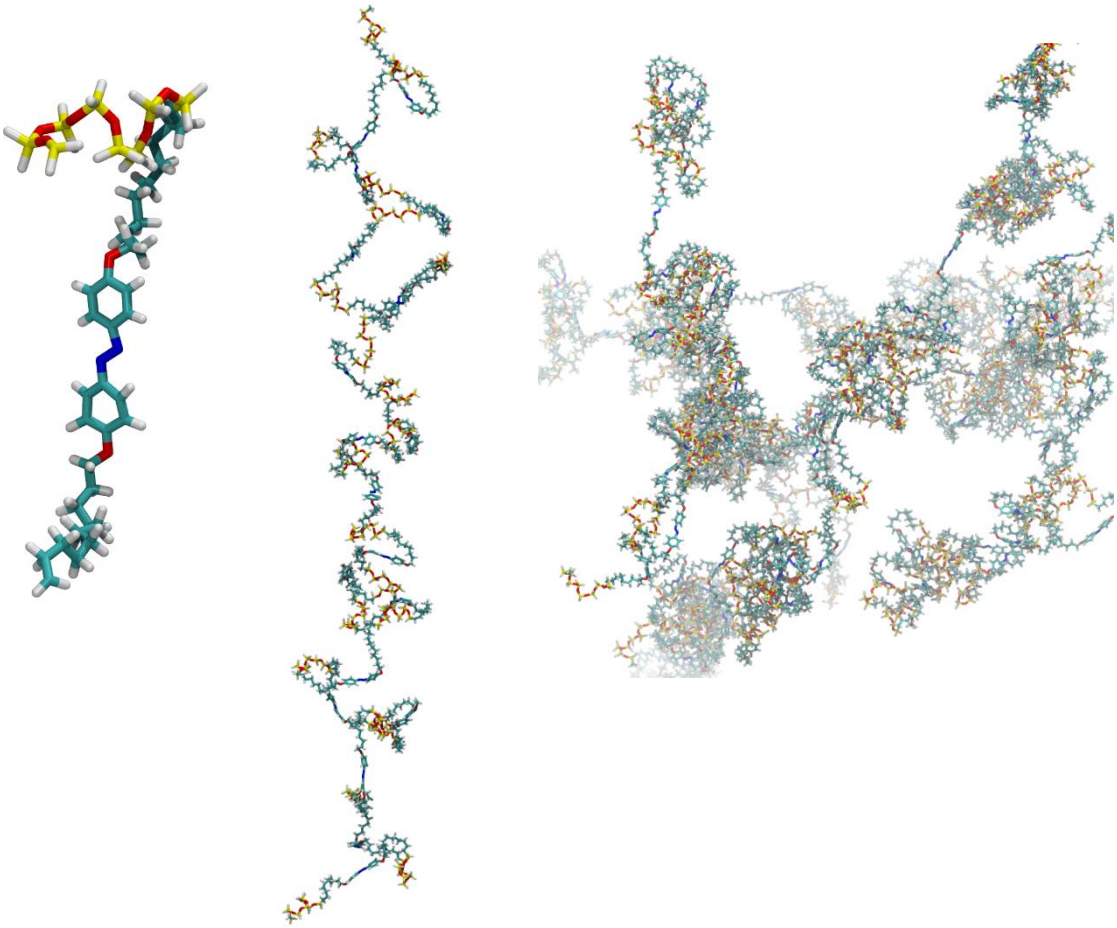

(a) one repeat unit (b) a single polymer chain (c) three polymer chains

Figure 9-14 All-atoms molecular model of azobenzene-containing structures. (a) One repeat unit containing one azobenzene group, two aliphatic segments and one siloxane chain; (b) a single polymer chain ($C_{11}Ar_2Si_8$) consisting of 20 repeat units; (c) a polymer system with three $C_{11}Ar_2Si_8$ chains.

Molecular dynamics simulations of the polymeric system were performed to investigate phase behavior of the azobenzene-containing polymers and to assist the understanding of the phase-transition mechanism. The simulation was performed with the Materials Studio software using the MM2 force field.

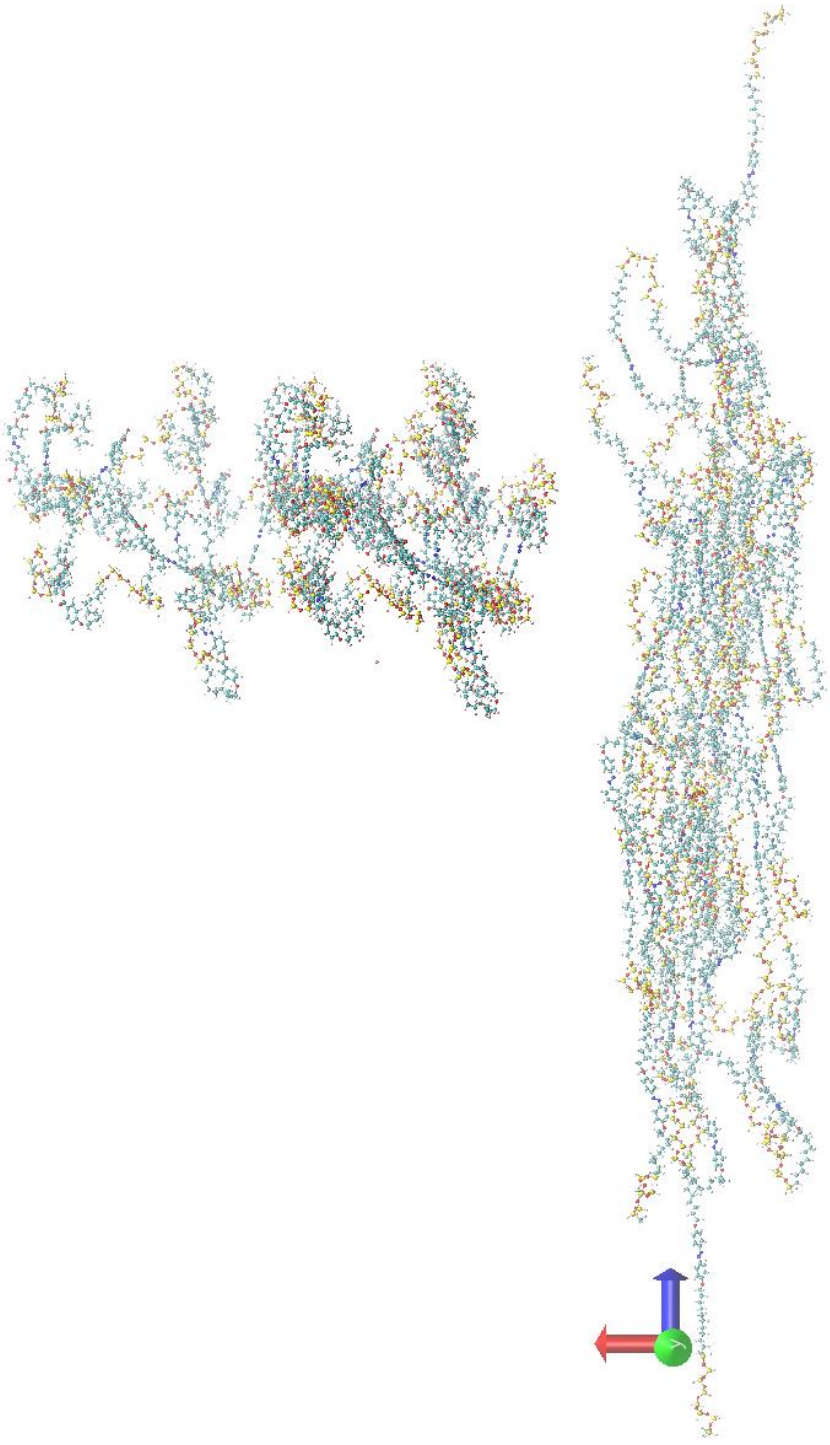

(a) initial structure **(b) deformed structure**

Figure 9-15 Morphology of azobenzene-containing polymer (a) before and (b) after deformation.

The simulation procedure was adopted from the deformation simulations in Chapter 4 and Chapter 5. An initial structure with a low density (see Figure 9-15a) was equilibrated at a high temperature (500 K) for 1 ns to remove internal stresses and reach a proper density. The system was then annealed at 400 K for 1 ns and stretched unidirectionally in a large strain to reach a highly anisotropic state (see Figure 9-15b).

The preliminary results showed a partially ordered polymeric structure at a high strain level at 350 K. The aliphatic segments and azobenzene groups are highly oriented in the stretching direction, while the siloxane groups are more disordered. These findings are consistent with the X-ray diffraction pattern in Figure 9-8a. These results also demonstrated that MD simulation procedures could be used to describe the azobenzene-containing LC systems investigated in this chapter and future research could expand the computational process to validate more experimental results in the dissertation.

9.8 Conclusions

Via poly-hydrosilylation, a series of liquid crystal elastomers were synthesized with azobenzene contaning mesogens. The mesogens with two or four benzene rings are symmetric structures while the three benzene ring mesogen is asymmetric. The two ring mesogen has only liquid crystalline phase while the other two has an additional liquid crystal phase. The transition temperatures for both the mesogenic monomer and corresponding polymer are higher with increased length of mesogen. According to the X-ray diffraction data, the LCEs are all smectic-C at room temperature. At an elevated temperature, the LCE films can be stretched to the monodomain phase either from the isotropic state or the polydomain state, depending on the LC-isotropic transitions of the

samples. A higher stretching ratio leads to an increasingly ordered system, until the monodomain is reached. All the highly ordered monodomain samples with azobenzene components display stress response to external UV irradiation at 365 nm, due to the *trans*-to-*cis* isomerization mechanism. Compared to symmetric structures, the asymmetric LCE with three benzene rings in the mesogenic group illustrates more prominent and faster response to the same condition of irradiation. A fully reversible actuation by a single monochromic light source at room temperature in a timely manner was achieved. All-atom molecular dynamics simulations of the experimental structure indicates increased order in the aliphatic segments and mesogenic groups, which is consistent with 2D X-ray diffraction data.

CHAPTER 10

CONCLUSIONS, SIGNIFICANCE AND RECOMMENDATIONS FOR FUTURE WORK

10.1 Conclusions

The simulations on single chain molecular dynamics showed that above a critical chain length and under suitable thermodynamics conditions, a single polymer chain could fold into a monodomain crystalline structure with a highly ordered overall structure. A relatively long chain takes significantly longer time period to relax and reorganize into a crystallite.

Multiple polymer chains with periodic boundary condition can form semi-crystalline structures under different processing conditions. By tuning the initial structure and the isothermal crystallization environment, samples from pre-oriented melt, under constant stress or constant volume conditions can obtain lamellar structures with similar crystallinity, crystal orientation, lamellae thicknesses and density distribution.

During the deformation simulations, the crystalline parts of samples prepared from different processing conditions act similarly, while the inter-crystal network plays a key role in the deformation morphology and the consequent defect initiation. At large deformation, the laminar-to-fibrillar transition is observed at the molecular level. The lamellar structure remained to a strain level of 0.5, followed by a transition to the fibrillar structure with long periods of highly ordered fibrils in the tensile direction, surrounded by amorphous interlayers. The elastic behavior of the bulk polymer samples depends largely on the molecular morphology, including the degree of crystallinity and the crystallite

orientation distribution. The highest yield stress is achieved by semi-crystalline structures with chains in the crystal domains that are predominantly oriented in the tensile direction. For the bidirectional oriented semi-crystalline structure, an enlarged region of strain hardening behavior is observed due to the rotation of crystals towards the tensile direction.

The recovery simulations of semi-crystalline structures after their deformation show further purification of both the crystalline part and the amorphous part. The crystalline part become better organized and the amorphous part become less oriented with added randomness. The well relaxed crystalline region and amorphous region have a more distinct interface.

Two-dimensional two-point statistics method is proven to be an effective tool in structural characterization of the semi-crystalline structure and their evolution during deformation. The microstructural function is defined by the local Hermans' orientation factor. Owing to the great difference between the amorphous and crystalline regions, the structure was well represented. The three-dimensional two-point statistics method further supports the laminar nature of a semi-crystalline polymer system. Hermans' orientation and two-point statistics analyses of the recovery of the as-deformed structures at both the lamellar stage and fibrillar stage confirm that the fibrillar structure introduced by large deformation is stable after relaxation.

The free surface plays a key role in the morphology of polymer thin film crystallization. Due to less confinement, chains near the free surface with higher mobility tends to remain amorphous with a slightly trend of flat-on morphology. Stress could also play a dominant part in the final crystallization morphology. Similar to the role in bulk

polymer crystallization, stress can induce and accelerate the crystallization process by reducing the entropy of the system. This chapter concentrates in the discussion of biaxial-stress induced polymer thin film crystallization. At a moderate stress level, the chains in the central region of the film are able to crystallize with unified orientation into a mondomain of crystalline structure. However, the crystallized chains are not aligned in the stretching direction. With strong biaxial stresses that align the chains in the stretching direction in the crystalline region, the free surface could also be crystallized due to less confinement. The featured surface has a crystalline texture consists of highly ordered flat-on chains.

For thin film crystallization on a single wetting substrate, the near-substrate, central and free surface areas act significantly differently due to the big difference in confinement. Owing to the strong attraction, highest density and flat-on morphology of the polymer chains are displayed near the substrate. The orientated chains in the near-substrate area would even further guide the crystallization morphology as a reference. The central region of a thin film displayed bulk-like crystallization behavior in which the polymer chain orientation are different than that of the near substrate area. At the surface area (top 1 nm) of a thin film, the density is significantly lower than those of the central and near-substrate regions, while the orientation varies substantially. This region is the least restricted region with higher mobility of chains towards vacuum. The surface is uneven and featureless.

For a thin film crystallized between parallel sheets, in addition to the near-substrate region characterized by densified flat-on chains influenced by the strong attractive force from the substrates, the center region develops into monodomain or polydomain of semi-

crystalline structures, depending on the distance between the parallel sheets. Slow shearing between parallel sheet will influent the crystalline domain orientation. Fast shearing breaks the crystallization condition of the central region. The near-substrate area has lower densities, while a monodomain highly unidirectional oriented slab is formed in the center.

Symmetric and asymmetric azobenzene containing main-chain liquid crystalline polymers and elastomers were studied. The two ring mesogen has only one liquid crystalline phase while the three- and four-ring has an additional liquid crystal phase. The transition temperatures for both the mesogen monomer and corresponding polymer are higher with increased length of mesogen.

According to the X-ray diffraction data, the LCEs are all smectic-C at room temperature. At an elevated temperature, the LCE films can be stretched to the monodomain phase either from the isotropic state or the polydomain state, depending on the LC-isotropic transitions of the samples. A higher stretching ratio leads to an increasingly ordered system, until the monodomain is reached. This is illustrated by the 2D XRD pattern and validated by molecular dynamics simulations results.

All the highly ordered monodomain samples with azobenzene components display stress response to external UV irradiation at 365 nm, due to the *trans*-to-*cis* isomerization mechanism. Compared to the symmetric structures, the asymmetric LCE with three benzene rings in the mesogenic group illustrates higher and faster response to the same condition of irradiation. A fully reversible actuation by a single monochromic light source at room temperature in a timely manner was achieved.

10.2 Significance of research

In this dissertation, molecular dynamics simulations combined with a variety of experimental techniques were employed to investigate the crystallization, liquid crystalline transition and deformation mechanisms governing mechanical and phase behavior observed in semi-crystalline and liquid crystalline polymeric materials. The findings from this research elucidated the evolution and influence of atomistic- and nano-scale molecular architecture and structural ordering affecting the bulk and surface behaviors at multiple length and time scales.

Several data-analyses tools were developed in this research, including local density mapping, 1D and 2D Hermans' orientation distributions, and 2D and 3D two-point statistics. This was the first time such parameters and tools are integrated in the analysis of the molecular-level dynamics during the entire process of crystallization, deformation and recovery of a partially-ordered polymeric system.

The two-point spatial correlation function $f(h, h'|\boldsymbol{r})$ has been shown to capture a number of traditional metrics used to quantify structure [81, 82]. Two-point statistics can provide rich information about multi-phase materials such as composites [106-110], polycrystals [83, 111] and porous materials[112, 113]. In this dissertation the application of two-point statistics was successfully expanded to a semi-crystalline polymeric system with Hermans' orientation spectrum. The use of two-point statistics in this regard is completely new.

The experimental part of this dissertation exploring the photo-responsiveness by liquid crystalline elastomers with the main-chain conformation complemented and validated simulation results and the effectiveness of data-analysis tools. Since very limited

useful result was available in the literature related to the behavior of photo-sensitive polymer systems, azobenzene containing polymers were prepared starting from the systems of unique azobenzene-containing monomers. The novel main-chain liquid crystalline elastomers developed and characterized in the research filled in a category which was less studied compared to the side-chain counterparts, but of particular fundamental interest owing to the correlation between molecular-scale liquid crystal ordering and the macroscopic orientation of the system. This accounts to substantial contribution in this area that will serve to validate additional MD studies.

Meanwhile, the successful design of the highly efficient photo-actuator tuned by a weak single light source also made break-through in the design of similar devices. Both the response time and accuracy of stress control were improved by taking advantage of the initial nearly linear region of the loading and unloading curves, respectively.

A major focus of the studies presented in this research was on the development and applications of various simulations/data analysis protocols to better describe the above-mentioned partially ordered systems, thus give insights into the fundamentals of the morphological evolution mechanism. More specifically, semi-crystalline and liquid crystalline polymers were primarily studied with a focus on the mechanical property predictions and description of order during the structural evolution. However, the tools developed here can be applied to other partially ordered material systems to further guide the studies on material structure-property relationships and provide robust guidance for computational materials design.

10.3 Recommendations for future work

During the first portion of this research (Chapters 2-7), simulations on the entire process of crystallization, deformation and recovery of a linear polyethylene-like polymeric system were carried out and analyzed extentively. The tools developed here, e.g., local density distribution, Hermans' orientation mapping, and two-point statistics could be expanded to the atomistic/molecular scale study of other partially ordered polymeric systems such as liquid crystalline polymers, synthetic fibers and biopolymers in various forms, and even anisotropic inorganic systems such as ferroelectric and magnetic materials and drawn metals.

The Hermans' orientation parameter defined in the dissertation is based on the chain vectors of neighboring repeat units, which is designed to represent local orders within a polymeric system without losing the trace of the long-chain nature of polymers. The microstructural function of two-point statistics is based on the Hermans' orientation parameter defined here. However, in the case of more complex polymeric structures such as liquid crystalline polymers and biopolymers, local vectors could be calculated within one repeat unit or as part of it, such as the mesogenic group of a main-chain liquid crystalline polymer or certain functional groups, with considerations from both local ordering and the general chain orientation. For inorganic systems, vectors could be selected from either lattice parameters from a local crystal domain or along the grain boundary. Microstructural functions could be thus defined to perform two-point statistics.

The simulations performed in this research involved a substantial amount of description in the structural evolution of large deformations of partially ordered systems. However, the simulations did not include bond breakage, i.e., the molecular weight was

assumed constant during the deformation process. However, covalent bonds in a polymer chain could also break during high strain rate large deformation, especially at elevated temperatures such as in some of the simulations conditions described in the thesis. It would be closer to the experiments to include bond-breaking criteria (e.g., certain force or distance cut-offs). This could also enhance the accuracy of mechanical property calculations in Chapter 5.

During the latter portion of the thesis, experimental works on novel main-chain liquid crystalline polymers were introduced (Chapter 9); these materials exhibit highly correlated local mesogenic order and macroscopic liquid crystalline domains. The hot-stretching method developed here to prepare monodomain samples bridges the multi-scale orientation scheme from the atomistic/molecular scale spanning to the macroscopic continuum scale.

The approach and the unique polymer architecture not only show good shape-memory and large actuation effects, but are also of particular interest for theoretical and simulations-based studies. Specifically, vectors as part of the mesogen in the main-chain can well-represent the local order of its neighboring region, e.g., a vector could be defined by the two N atoms of an azo group or by two benzene rings attached to it. By averaging the Hermans' orientation of such vectors in a characteristic length scale (e.g., comparable to the resolution of XRD experimental set-up), the order parameters of nano-scale liquid crystalline domains could be calculated and compared with calculations from experimental data. Furthermore, the microstructural functions based on the local ordering state calculations could be utilized in two-point statistics analysis of the bulk system. Since a substantial density difference exists between the highly ordered (dense) liquid crystalline

region and the random siloxane region, using local density as the microstructural function for a comparison between the two could produce well-ordered patterns.

On the other hand, simulations and quantifications of the photo-responsiveness of the azobenzene-containing functional liquid crystalline polymers will also make a significant impact on the fundamental understanding of such a behavior. Molecular dynamics simulations can reach different quasi-equilibrium states that correspond to different stages of *trans-cis* isomerization. At the *trans*-state, the vectors are mostly aligned towards the general liquid crystal orientation, while at the cis-state, vectors are substantially off-axis; thus, the calculated order parameter of a domain is expected to drop. Based on such statistics, *trans-cis* isomerization could be directly linked to the order parameter evolution with time of UV-irradiation, which is also available from the XRD results presented in Chapter 9. From such simulations, stress could also be calculated by the method applied in Chapter 5 with respect to the *trans-cis* ratio inside a liquid crystalline polymeric system. Fundamental relationship between the molecular level isomerization mechanism and the macroscopic stress response could be established and insights into more efficient photo-actuation materials could be developed using the computationally-assisted molecular architecture design.

REFERENCES

1. Yoon, D.Y. and P.J. Flory, *SMALL-ANGLE NEUTRON-SCATTERING BY SEMICRYSTALLINE POLYETHYLENE.* Polymer, 1977. **18**(5): p. 509-513.

2. Summerfield, G.C., J.S. King, and R. Ullman, *SMALL-ANGLE NEUTRON-SCATTERING FROM SOLUTION-CRYSTALLIZED AND MELT-CRYSTALLIZED POLYETHYLENE.* Journal of Applied Crystallography, 1978. **11**(OCT): p. 548-551.

3. Schelten, J., D.G.H. Ballard, G.D. Wignall, G. Longman, and W. Schmatz, *SMALL-ANGLE NEUTRON-SCATTERING STUDIES OF MOLTEN AND CRYSTALLINE POLYETHYLENE.* Polymer, 1976. **17**(9): p. 751-757.

4. Lustiger, A., B. Lotz, and T.S. Duff, *THE MORPHOLOGY OF THE SPHERULITIC SURFACE IN POLYETHYLENE.* Journal of Polymer Science Part B-Polymer Physics, 1989. **27**(3): p. 561-579.

5. Dicorleto, J.A. and D.C. Bassett, *ON CIRCULAR CRYSTALS OF POLYETHYLENE.* Polymer, 1990. **31**(10): p. 1971-1977.

6. Haward, R.N., *STRAIN-HARDENING OF THERMOPLASTICS.* Macromolecules, 1993. **26**(22): p. 5860-5869.

7. Bartczak, Z., R.E. Cohen, and A.S. Argon, *Evolution of the Crystalline Texture of High-Density Polyethylene during Uniaxial Compression.* Macromolecules, 1992. **25**(18): p. 4692-4704.

8. Bartczak, Z., A.S. Argon, and R.E. Cohen, *Texture Evolution in Large-Strain Simple Shear Deformation of High-Density Polyethylene.* Polymer, 1994. **35**(16): p. 3427-3441.

9. Meinel, G. and A. Peterlin, *PLASTIC DEFORMATION OF POLYETHYLENE .3. MECHANICAL PROPERTIES AND MORPHOLOGY OF DRAWN LOW DENSITY POLYETHYLENE.* European Polymer Journal, 1971. **7**(6): p. 657.

10. Meinel, G. and A. Peterlin, *PLASTIC DEFORMATION OF POLYETHYLENE .2. CHANGE OF MECHANICAL PROPERTIES DURING DRAWING.* Journal of Polymer Science Part a-2-Polymer Physics, 1971. **9**(1): p. 67.

11. Peterlin, A. and G. Meinel, *SMALL-ANGLE X-RAY DIFFRACTION STUDIES OF PLASTICALLY DEFORMED POLYETHYLENE .3. SMALL DRAW RATIOS.* Makromolekulare Chemie, 1971. **142**(MAR): p. 227.

12. Jiang, Z.Y., Y.J. Tang, J. Rieger, H.F. Enderle, D. Lilge, S.V. Roth, R. Gehrke, W. Heckmann, and Y.F. Men, *Two Lamellar to Fibrillar Transitions in the Tensile Deformation of High-Density Polyethylene.* Macromolecules, 2010. **43**(10): p. 4727-4732.

13. Al-Hussein, M. and G. Strobl, *Strain-controlled tensile deformation behavior of isotactic poly(1-butene) and its ethylene copolymers.* Macromolecules, 2002. **35**(22): p. 8515-8520.

14. Hiss, R., S. Hobeika, C. Lynn, and G. Strobl, *Network stretching, slip processes, and fragmentation of crystallites during uniaxial drawing of polyethylene and related copolymers. A comparative study.* Macromolecules, 1999. **32**(13): p. 4390-4403.

15. Hobeika, S., Y. Men, and G. Strobl, *Temperature and strain rate independence of critical strains in polyethylene and poly(ethylene-co-vinyl acetate).* Macromolecules, 2000. **33**(5): p. 1827-1833.

16. Men, Y. and G. Strobl, *Critical strains in poly(epsilon-caprolactone) and blends with poly(vinyl methyl ether) and poly(styrene-co-acrylonitrile).* Macromolecules, 2003. **36**(6): p. 1889-1898.

17. Hong, K. and G. Strobl, *Network stretching during tensile drawing of polyethylene: A study using X-ray scattering and microscopy.* Macromolecules, 2006. **39**(1): p. 268-273.

18. Samon, J.M., J.M. Schultz, B.S. Hsiao, S. Seifert, N. Stribeck, I. Gurke, G. Collins, and C. Saw, *Structure development during the melt spinning of polyethylene and poly(vinylidene fluoride) fibers by in situ synchrotron small- and wide-angle X-ray scattering techniques.* Macromolecules, 1999. **32**(24): p. 8121-8132.

19. Samon, J.M., J.M. Schultz, B.S. Hsiao, J. Wu, and S. Khot, *Structure development during melt spinning and subsequent annealing of polybutene-1 fibers.* Journal of Polymer Science Part B-Polymer Physics, 2000. **38**(14): p. 1872-1882.

20. Cai, J.L., B.S. Hsiao, and R.A. Gross, *Real-Time Structure Changes during Uniaxial Stretching of Poly (omega-pentadecalactone) by in Situ Synchrotron WAXD/SAXS Techniques.* Macromolecules, 2011. **44**(10): p. 3874-3883.

21. Tang, Y.J., Z.Y. Jiang, Y.F. Men, L.J. An, H.F. Enderle, D. Lilge, S.V. Roth, R. Gehrke, and J. Rieger, *Uniaxial deformation of overstretched polyethylene: In-situ synchrotron small angle X-ray scattering study.* Polymer, 2007. **48**(17): p. 5125-5132.

22. Stribeck, N., *Extraction of domain structure information from small-angle scattering patterns of bulk materials.* Journal of Applied Crystallography, 2001. **34**: p. 496-503.

23. Stribeck, N., R. Bayer, P. Bosecke, and A.A. Camarillo, *Visualisation of the structure transfer between an oriented polymer melt and the semi-crystalline state.* Polymer, 2005. **46**(8): p. 2579-2583.

24. Schneider, K., *Investigation of Structural Changes in Semi-Crystalline Polymers During Deformation by Synchrotron X-Ray Scattering.* Journal of Polymer Science Part B-Polymer Physics, 2010. **48**(14): p. 1574-1586.

25. Xu, G.Q. and W.L. Mattice, *Study on structure formation of short polyethylene chains via dynamic Monte Carlo simulation.* Computational and Theoretical Polymer Science, 2001. **11**(6): p. 405-413.

26. Rapold, R.F. and W.L. Mattice, *NEW HIGH-COORDINATION LATTICE MODEL FOR ROTATIONAL ISOMERIC STATE POLYMER-CHAINS.* Journal of the Chemical Society-Faraday Transactions, 1995. **91**(16): p. 2435-2441.

27. Boyd, R.H., R.H. Gee, J. Han, and Y. Jin, *Conformational Dynamics in Bulk Polyethylene - a Molecular-Dynamics Simulation Study.* Journal of Chemical Physics, 1994. **101**(1): p. 788-797.

28. Waheed, N., M.S. Lavine, and G.C. Rutledge, *Molecular simulation of crystal growth in n-eicosane.* Journal of Chemical Physics, 2002. **116**(5): p. 2301-2309.

29. Yi, P. and G.C. Rutledge, *Molecular simulation of crystal nucleation in n-octane melts.* Journal of Chemical Physics, 2009. **131**(13).

30. Ko, M.J., N. Waheed, M.S. Lavine, and G.C. Rutledge, *Characterization of polyethylene crystallization from an oriented melt by molecular dynamics simulation.* Journal of Chemical Physics, 2004. **121**(6): p. 2823-2832.

31. Yamamoto, polymer, 2013.

32. Capaldi, F.M., M.C. Boyce, and G.C. Rutledge, *Enhanced mobility accompanies the active deformation of a glassy amorphous polymer.* Physical Review Letters, 2002. **89**(17).

33. Capaldi, F.M., M.C. Boyce, and G.C. Rutledge, *Molecular response of a glassy polymer to active deformation.* Polymer, 2004. **45**(4): p. 1391-1399.

34. Hossain, D., M.A. Tschopp, D.K. Ward, J.L. Bouvard, P. Wang, and M.F. Horstemeyer, *Molecular dynamics simulations of deformation mechanisms of amorphous polyethylene.* Polymer, 2010. **51**(25): p. 6071-6083.

35. Gautam, S., S. Balijepalli, and G.C. Rutledge, *Molecular simulations df the interlamellar phase in polymers: Effect of chain tilt.* Macromolecules, 2000. **33**(24): p. 9136-9145.

36. Hutter, M., P.J. in 't Veld, and G.C. Rutledge, *Polyethylene {201} crystal surface: interface stresses and thermodynamics.* Polymer, 2006. **47**(15): p. 5494-5504.

37. Lee, S. and G.C. Rutledge, *Plastic Deformation of Semicrystalline Polyethylene by Molecular Simulation.* Macromolecules, 2011. **44**(8): p. 3096-3108.

38. Hudzinskyy, D., A.V. Lyulin, A.R.C. Baljon, N.K. Balabaev, and M.A.J. Michels, *Effects of Strong Confinement on the Glass-Transition Temperature in Simulated Atactic Polystyrene Films.* Macromolecules, 2011. **44**(7): p. 2299-2310.

39. Finkelmann, H., E. Nishikawa, G.G. Pereira, and M. Warner, *A new opto-mechanical effect in solids.* Phys Rev Lett, 2001. **87**(1): p. 015501.

40. Wim, H.d.J., *Liquid Crystal Elastomers: Materials and Applications*. 2012.

41. De Gennes, P.G., *Phenomenology of short-range-order effects in the isotropic phase of nematic materials.* Physics Letters A, 1969. **30**(8): p. 454-455.

42. Küpfer, J. and H. Finkelmann, *Nematic liquid single crystal elastomers.* Die Makromolekulare Chemie, Rapid Communications, 1991. **12**(12): p. 717-726.

43. Donnio, B., H. Wermter, and H. Finkelmann, *A Simple and Versatile Synthetic Route for the Preparation of Main-Chain, Liquid-Crystalline Elastomers.* Macromolecules, 2000. **33**(21): p. 7724-7729.

44. Yu, Y., M. Nakano, and T. Ikeda, *Photomechanics: directed bending of a polymer film by light.* Nature, 2003. **425**(6954): p. 145.

45. Tylkowski, B., M. Pregowska, E. Jamowska, R. Garcia-Valls, and M. Giamberini, *Preparation of a new lightly cross-linked liquid crystalline polyamide by interfacial polymerization. Application to the obtainment of microcapsules with photo-triggered release.* European Polymer Journal, 2009. **45**(5): p. 1420-1432.

46. Lee, K.M., N.V. Tabiryan, T.J. Bunning, and T.J. White, *Photomechanical mechanism and structure-property considerations in the generation of photomechanical work in glassy, azobenzene liquid crystal polymer networks.* Journal of Materials Chemistry, 2012. **22**(2): p. 691-698.

47. Saminathan, M. and C.K.S. Pillai, *Synthesis of novel liquid crystalline polymers with cross-linked network structures.* Polymer, 2000. **41**(8): p. 3103-3108.

48. Lee, K.M., H. Koerner, R.A. Vaia, T.J. Bunning, and T.J. White, *Light-activated shape memory of glassy, azobenzene liquid crystalline polymer networks.* Soft Matter, 2011. **7**(9): p. 4318-4324.

49. Takashima, Y., S. Hatanaka, M. Otsubo, M. Nakahata, T. Kakuta, A. Hashidzume, H. Yamaguchi, and A. Harada, *Expansion–contraction of photoresponsive artificial muscle regulated by host–guest interactions.* Nat Commun, 2012. **3**: p. 1270.

50. Palffy-Muhoray, P., *Liquid crystals: Printed actuators in a flap.* Nat Mater, 2009. **8**(8): p. 614-615.

51. Camacho-Lopez, M., H. Finkelmann, P. Palffy-Muhoray, and M. Shelley, *Fast liquid-crystal elastomer swims into the dark.* Nat Mater, 2004. **3**(5): p. 307-310.

52. Pei, Z., Y. Yang, Q. Chen, E.M. Terentjev, Y. Wei, and Y. Ji, *Mouldable liquid-crystalline elastomer actuators with exchangeable covalent bonds.* Nat Mater, 2014. **13**(1): p. 36-41.

53. Woltman, S.J., G.D. Jay, and G.P. Crawford, *Liquid-crystal materials find a new order in biomedical applications.* Nat Mater, 2007. **6**(12): p. 929-938.

54. Yamada, M., M. Kondo, R. Miyasato, Y. Naka, J.-i. Mamiya, M. Kinoshita, A. Shishido, Y. Yu, C.J. Barrett, and T. Ikeda, *Photomobile polymer materials-various three-dimensional movements.* Journal of Materials Chemistry, 2009. **19**(1): p. 60-62.

55. Yamada, M., M. Kondo, J.-i. Mamiya, Y. Yu, M. Kinoshita, C.J. Barrett, and T. Ikeda, *Photomobile Polymer Materials: Towards Light-Driven Plastic Motors.* Angewandte Chemie International Edition, 2008. **47**(27): p. 4986-4988.

56. Dawson, N.J., M.G. Kuzyk, J. Neal, P. Luchette, and P. Palffy-Muhoray, *Cascading of liquid crystal elastomer photomechanical optical devices.* Optics Communications, 2011. **284**(4): p. 991-993.

57. Li, Z., Y. Zhang, L. Zhu, T. Shen, and H. Zhang, *Efficient synthesis of photoresponsive azobenzene-containing side-chain liquid crystalline polymers with high molecular weights by click chemistry.* Polymer Chemistry, 2010. **1**(9): p. 1501-1511.

58. Graham-Rowe, D., *A new twist to tuning lasers.* Nat Photon, 2009. **3**(4): p. 183-184.

59. Yanlei, Y., M. Nakano, and T. Ikeda, *Photoinduced bending and unbending behavior of liquid-crystalline gels and elastomers.* Pure and Applied Chemistry, 2004. **76**(7-8): p. 1467-1477.

60. Serak, S., N. Tabiryan, R. Vergara, T.J. White, R.A. Vaia, and T.J. Bunning, *Liquid crystalline polymer cantilever oscillators fueled by light.* Soft Matter, 2010. **6**(4): p. 779-783.

61. Hayata, Y., S. Nagano, Y. Takeoka, and T. Seki, *Photoinduced Volume Transition in Liquid Crystalline Polymer Gels Swollen by a Nematic Solvent.* ACS Macro Letters, 2012. **1**(11): p. 1357-1361.

62. Ikeda, T., M. Nakano, Y. Yu, O. Tsutsumi, and A. Kanazawa, *Anisotropic Bending and Unbending Behavior of Azobenzene Liquid-Crystalline Gels by Light Exposure.* Advanced Materials, 2003. **15**(3): p. 201-205.

63. Lee, K.M., H. Koerner, R.A. Vaia, T.J. Bunning, and T.J. White, *Relationship between the Photomechanical Response and the Thermomechanical Properties of Azobenzene Liquid Crystalline Polymer Networks.* Macromolecules, 2010. **43**(19): p. 8185-8190.

64. Wie, J.J., D.H. Wang, K.M. Lee, L.-S. Tan, and T.J. White, *Molecular Engineering of Azobenzene-Functionalized Polyimides To Enhance Both Photomechanical Work and Motion.* Chemistry of Materials, 2014. **26**(18): p. 5223-5230.

65. Wang, D.H., J.J. Wie, K.M. Lee, T.J. White, and L.-S. Tan, *Impact of Backbone Rigidity on the Photomechanical Response of Glassy, Azobenzene-Functionalized Polyimides.* Macromolecules, 2014. **47**(2): p. 659-667.

66. Wang, D.H., K.M. Lee, Z. Yu, H. Koerner, R.A. Vaia, T.J. White, and L.-S. Tan, *Photomechanical Response of Glassy Azobenzene Polyimide Networks.* Macromolecules, 2011. **44**(10): p. 3840-3846.

67. Lee, K.M. and T.J. White, *Photochemical Mechanism and Photothermal Considerations in the Mechanical Response of Monodomain, Azobenzene-Functionalized Liquid Crystal Polymer Networks.* Macromolecules, 2012. **45**(17): p. 7163-7170.

68. Sánchez-Ferrer, A., A. Merekalov, and H. Finkelmann, *Opto-Mechanical Effect in Photoactive Nematic Side-Chain Liquid-Crystalline Elastomers.* Macromolecular Rapid Communications, 2011. **32**(8): p. 671-678.

69. Sánchez-Ferrer, A., T. Fischl, M. Stubenrauch, H. Wurmus, M. Hoffmann, and H. Finkelmann, *Photo-Crosslinked Side-Chain Liquid-Crystalline Elastomers for Microsystems.* Macromolecular Chemistry and Physics, 2009. **210**(20): p. 1671-1677.

70. Garcia-Amoros, J., H. Finkelmann, and D. Velasco, *Influence of the photo-active azo cross-linker spacer on the opto-mechanics of polysiloxane elastomer actuators.* Journal of Materials Chemistry, 2011. **21**(4): p. 1094-1101.

71. Sánchez-Ferrer, A. and H. Finkelmann, *Thermal and mechanical properties of new Main-Chain Liquid-Crystalline Elastomers.* Solid State Sciences, 2010. **12**(11): p. 1849-1852.

72. Sanchez-Ferrer, A. and H. Finkelmann, *Opto-mechanical effect in photoactive nematic main-chain liquid-crystalline elastomers.* Soft Matter, 2013. **9**(18): p. 4621-4627.

73. Sánchez-Ferrer, A. and H. Finkelmann, *Uniaxial and Shear Deformations in Smectic-C Main-Chain Liquid-Crystalline Elastomers.* Macromolecules, 2008. **41**(3): p. 970-980.

74. Jiang, X., X. Chen, X. Yue, J. Zhang, S. Guan, H. Zhang, W. Zhang, and Q. Chen, *Synthesis and characterization of photoactive poly(arylene ether sulfone)s containing azobenzene moieties in their main chains.* Reactive and Functional Polymers, 2010. **70**(9): p. 616-621.

75. Bualek, S. and R. Zentel, *Crosslinkable liquid-crystalline combined main-chain/side-group polymers with low glass transition temperatures.* Die Makromolekulare Chemie, 1988. **189**(4): p. 791-796.

76. Shepherd, J.E., *Multiscale Modeling of the Deformation of Semi-Crystalline Polymers*, in *Mechanical Engineering*. 2006, Georgia Institute of Technology: USA.

77. Plimpton, S., *FAST PARALLEL ALGORITHMS FOR SHORT-RANGE MOLECULAR-DYNAMICS.* Journal of Computational Physics, 1995. **117**(1): p. 1-19.

78. Paul, W., D.Y. Yoon, and G.D. Smith, *An Optimized United Atom Model for Simulations of Polymethylene Melts.* Journal of Chemical Physics, 1995. **103**(4): p. 1702-1709.

79. Hermans, P.H. and P. Platzek, *The stability-elongation-diagram of isotropic cellulose filaments in light of the theoretical relationship between source anisotropy, orientation and stability II Filaments of various production manners.* Kolloid-Zeitschrift, 1939. **89**(3): p. 349-354.

80. Hermans, P.H., J.J. Hermans, D. Vermaas, and A. Weidinger, *Deformation Mechanism of Cellulose Gels .4. General Relationship between Orientation of the Crystalline and That of the Amorphous Portion.* Journal of Polymer Science, 1948. **3**(1): p. 1-9.

81. Fullwood, D.T., S.R. Niezgoda, B.L. Adams, and S.R. Kalidindi, *Microstructure sensitive design for performance optimization.* Progress in Materials Science, 2010. **55**(6): p. 477-562.

82. Niezgoda, S.R., Y.C. Yabansu, and S.R. Kalidindi, *Understanding and Visualizing Microstructure and Microstructure Variance as a Stochastic Process.* Acta Materialia, 2011. **59**: p. 6387-6400.

83. Adams, B.L., X. Gao, and S.R. Kalidindi, *Finite approximations to the second-order properties closure in single phase polycrystals.* Acta Materialia, 2005. **53**(13): p. 3563-3577.

84. Nosé, S., *A unified formulation of the constant temperature molecular dynamics methods.* The Journal of Chemical Physics, 1984. **81**(1): p. 511-519.

85. Nosé, S., *A molecular dynamics method for simulations in the canonical ensemble.* Molecular Physics, 1984. **52**(2): p. 255-268.

86. Hoover, W.G., *Canonical dynamics: Equilibrium phase-space distributions.* Physical Review A, 1985. **31**(3): p. 1695-1697.

87. Dong, X., D.L. McDowell, S.R. Kalidindi, and K.I. Jacob, *Dependence of mechanical properties on crystal orientation of semi-crystalline polyethylene structures.* Polymer, 2014. **55**(16): p. 4248-4257.

88. Peacock, A.J., *Handbook of polyethylene: structures, properties and applications*. 2000.

89. Dong, X., D. McDowell, and K. Jacob, *Effect of network structure from different processing conditions on the mechanical property of semi-crystalline polymers.* MRS Online Proceedings Library, 2014. **1619**

90. Pawlak, A., *Cavitation during tensile deformation of high-density polyethylene.* Polymer, 2007. **48**(5): p. 1397-1409.

91. Slusarczyk, C., *Time-resolved SAXS investigations of morphological changes in a blend of linear and branched polyethylenes during crystallization and subsequent melting.* Journal of Alloys and Compounds, 2004. **382**(1-2): p. 68-74.

92. Liu, T., S. Yan, M. Bonnet, I. Lieberwirth, K.D. Rogausch, and J. Petermann, *DSC and TEM investigations on multiple melting phenomena in isotactic polystyrene.* Journal of Materials Science, 2000. **35**(20): p. 5047-5055.

93. Ghosh, S., D. Usharani, A. Paul, S. De, E.D. Jemmis, and S. Bhattacharya, *Design, Synthesis, and DNA Binding Properties of Photoisomerizable Azobenzene−Distamycin*

Conjugates: An Experimental and Computational Study. Bioconjugate Chemistry, 2008. **19**(12): p. 2332-2345.

94. Tokuhisa, H., M. Yokoyama, and K. Kimura, *Synthesis of crowned azobenzene derivatives and their photoresponsive ion-conducting behavior.* Chemistry of Materials, 1993. **5**(7): p. 989-993.

95. Ramesh Babu, R., S. Kumaresan, N. Vijayan, M. Gunasekaran, R. Gopalakrishnan, P. Kannan, and P. Ramasamy, *Growth of 4,4′-dihydroxyazobenzene (DHAB) and its characterization.* Journal of Crystal Growth, 2003. **256**(3–4): p. 387-392.

96. Zhang, Z., *Synthetic scheme of the monomers C11Ar3AB and C11Ar4AB were adopted from private communication with Dr. Zaixing Zhang in "Photoresponsive main-chain liquid crystalline elastomers containing symmetric and asymmetric azobenzene mesogens via hydrosilylation polymerization", unpublished manuscript.*

97. Ren, W., P.J. McMullan, and A.C. Griffin, *Stress–strain behavior in main chain liquid crystalline elastomers: effect of crosslinking density and transverse rod incorporation on "Poisson's ratio".* physica status solidi (b), 2009. **246**(9): p. 2124-2130.

98. Ren, W., P.J. McMullan, H. Guo, S. Kumar, and A.C. Griffin, *A Liquid Crystalline Elastomer with a p-Pentaphenyl Transverse Rod Laterally Attached to the Main Chain.* Macromolecular Chemistry and Physics, 2008. **209**(3): p. 272-278.

99. Zaixing Zhang, X.D., Anselm Griffin and Karl Jacob, *Synthetic scheme of LCEs containing different azobenzene moieties (a) C11Ar2Si8XL10, (b) C11Ar3Si8XL10 and (c) C11Ar4Si8XL10 were adopted from private communication with Dr. Zaixing Zhang in "Photoresponsive main-chain liquid crystalline elastomers containing symmetric and*

asymmetric azobenzene mesogens via hydrosilylation polymerization", unpublished manuscript.

100. Sánchez-Ferrer, A. and H. Finkelmann, *Polydomain–Monodomain Orientational Process in Smectic-C Main-Chain Liquid-Crystalline Elastomers.* Macromolecular Rapid Communications, 2011. **32**(3): p. 309-315.

101. Kim, S.T. and H. Finkelmann, *Cholesteric Liquid Single-Crystal Elastomers (LSCE) Obtained by the Anisotropic Deswelling Method.* Macromolecular Rapid Communications, 2001. **22**(6): p. 429-433.

102. Burke, K.A. and P.T. Mather, *Soft shape memory in main-chain liquid crystalline elastomers.* Journal of Materials Chemistry, 2010. **20**(17): p. 3449-3457.

103. Ren, W. and A.C. Griffin, *Mechanism of strain retention and shape memory in main chain liquid crystalline networks.* physica status solidi (b), 2012. **249**(7): p. 1379-1385.

104. Ahn, S.-k., P. Deshmukh, M. Gopinadhan, C.O. Osuji, and R.M. Kasi, *Side-Chain Liquid Crystalline Polymer Networks: Exploiting Nanoscale Smectic Polymorphism To Design Shape-Memory Polymers.* ACS Nano, 2011. **5**(4): p. 3085-3095.

105. Tsoi, S., J. Zhou, C. Spillmann, J. Naciri, T. Ikeda, and B. Ratna, *Liquid-Crystalline Nano-optomechanical Actuator.* Macromolecular Chemistry and Physics, 2013. **214**(6): p. 734-741.

106. Jiao, Y., F.H. Stillinger, and S. Torquato, *Modeling heterogeneous materials via two-point correlation functions. II. Algorithmic details and applications.* Physical Review E, 2008. **77**(3).

107. Jiao, Y., F.H. Stillinger, and S. Torquato, *Modeling heterogeneous materials via two-point correlation functions: Basic principles.* Physical Review E, 2007. **76**(3).

108. Fullwood, D.T., S.R. Niezgoda, and S.R. Kalidindi, *Microstructure reconstructions from 2-point statistics using phase-recovery algorithms.* Acta Materialia, 2008. **56**(5): p. 942-948.

109. Niezgoda, S.R., D.M. Turner, D.T. Fullwood, and S.R. Kalidindi, *Optimized structure based representative volume element sets reflecting the ensemble-averaged 2-point statistics.* Acta Materialia, 2010. **58**(13): p. 4432-4445.

110. Kalidindi, S.R., S.R. Niezgoda, and A.A. Salem, *Microstructure informatics using higher-order statistics and efficient data-mining protocols.* JOM, 2011. **63**(4): p. 34-41.

111. Qidwai, S.M., D.M. Turner, S.R. Niezgoda, A.C. Lewis, A.B. Geltmacher, D.J. Rowenhorst, and S.R. Kalidindi, *Estimating response of polycrystalline materials using sets of weighted statistical volume elements (WSVEs).* Acta Materialia, 2012. **60**: p. 5284–5299.

112. Gommes, C.J., Y. Jiao, and S. Torquato, *Microstructural degeneracy associated with a two-point correlation function and its information content.* Physical Review E, 2012. **85**(5).

113. Gommes, C.J., H. Friedrich, P.E. de Jongh, and K.P. de Jong, *2-Point correlation function of nanostructured materials via the grey-tone correlation function of electron tomograms: A three-dimensional structural analysis of ordered mesoporous silica.* Acta Materialia, 2010. **58**(3): p. 770-780.